# Search for Signals of Decaying Dark Matter and Spectral Features in the Flux of Electron and Positron Cosmic-Rays Measured with CALET on the ISS

暗黒物質崩壊によるシグナル探査と ISS 搭載 CALET による宇宙線電子・陽電子フラックスのスペクトル構造

February, 2019

**Saptashwa BHATTACHARYYA**

バタチャリヤ　サパタシャワ

# Search for Signals of Decaying Dark Matter and Spectral Features in the Flux of Electron and Positron Cosmic-Rays Measured with CALET on the ISS

# 暗黒物質崩壊によるシグナル探査とISS搭載CALETによる宇宙線電子・陽電子フラックスのスペクトル構造

February, 2019


Waseda University

Graduate School of Advanced Science and Engineering
Department of Pure and Applied Physics
Research on Observational Astrophysics

**Saptashwa BHATTACHARYYA**

バタチャリヤ　サパタシャワ

# Abbreviations

AIC *Akaike Information Criterion*

CR *Cosmic Ray*

DM *Dark Matter*

DSA *Diffusive Shock Acceleration*

FSR *Final State Radiation*

ICS *Inverse Compton Scattering*

ISM *Interstellar Medium*

ISRF *Interstellar Radiation Field*

LIS *Local Interstellar Spectrum*

LKP *Lightest Kaluza-Klein Particle*

MACHO *Massive Compact Halo Objects*

MHD *Magneto-Hydrodynamic*

PWN *Pulsar Wind Nebula*

SNR *Supernova Remnants*

WIMP *Weakly Interacting Massive Particle*

# Contents

**List of Figures** 6

**Abstract** 10

**Introduction** 11

**1 Cosmic Ray Sources, Propagation and Observation** 14

1.1 Sources and Acceleration of Primary Cosmic Rays . . . . . 14

1.2 Interstellar Medium and Galactic Magnetic Field . . . . . 20

1.3 Models for Cosmic Ray Propagation . . . . . 21

1.3.1 Leaky Box Model . . . . . 21

1.3.2 Diffusion Model . . . . . 23

1.4 Solar Modulation . . . . . 27

1.5 Cosmic Ray Observation . . . . . 28

1.6 CALET on International Space Station . . . . . 31

1.6.1 CALET Detector Components . . . . . 31

1.6.2 Science Goals of CALET Detector . . . . . 35

**2 Dark Matter: Evidences and Detection Methods** **39**

2.1 Gravitational Effects of Dark Matter . . . . . 39

2.2 Dark Matter Candidates . . . . . 43

2.3 Dark Matter Detection Methods . . . . . 45

2.3.1 Collider Search and Direct Detection of Dark Matter . . . . 45

2.3.2 Indirect Dark Matter Detection . . . . . 47

**3 Calculation of Cosmic Ray Propagation** **53**

3.1 Analytical Method to Solve Transport Equation . . . . . 53

3.2 GALPROP: Numerical Calculation of Cosmic Ray Propagation . . 57

3.2.1 Numerical Solution of Diffusion Equation . . . . . 57

3.2.2 Crank-Nicolson Method for Solving Cosmic Ray Diffusion . . 59

3.2.3 Cosmic Ray Propagation using GALPROP . . . . . 59

3.3 Energy Loss of Cosmic Ray Electrons in GALPROP . . . . . 63

3.4 Calculation of Dark Matter Signatures with GALPROP . . . . . 68

3.5 Choice of Propagation Parameters for Dark Matter Propagation . . . . . 69

3.6 Self-Consistent Simulation of Background and Dark Matter Signals . . . . . 73

**4 Discerning Signals of Fermionic Dark Matter Decay from Single Pulsar with CALET** **79**

4.1 Observance of Rise in Cosmic Ray Positron Fraction . . . . . 79

4.2 Dark Matter or Pulsar as Extra Source of Cosmic-Ray Positrons . . . . . 80

4.3 3-body Decay of Dark Matter and Fermionic Dark Matter Model . . . . . 85

4.4 Parametrization of Observed Cosmic Ray Electron and Positron Flux . . . . . 87

4.5 Positron Excess with 3-Body Dark Matter Decay and Single Pulsar 90

4.6 Diffuse $\gamma$-ray Constraint on Dark Matter Decay Model . . . . . 92

4.6.1 Primary and Secondary $\gamma$-ray Production from Dark Matter Decay . . . . . 92

4.6.2 Dark Matter Decay Models with Low $\gamma$-ray Flux . . . . . 94

4.7 Discerning Dark Matter Decay Spectra from Single Pulsar Spectra using CALET . . . . . 96

**5 Interpretation of the $e^- + e^+$ Spectrum Measured by CALET on the ISS 103**

5.1 Current Status of $e^- + e^+$ Measurement . . . . . 103

5.2 CALET $e^- + e^+$ Flux Measurement and Result . . . . . 104

5.3 Parametrization of the Observed $e^+$ and $e^-$ Spectrum . . . . . 107

5.3.1 Single Power-law Parametrization . . . . . 107

5.3.2 Smoothly Broken Power-law Parametrization . . . . . 108

5.4 Explaining CALET Measurement with Dark Matter Decay or Single Pulsar . . . . . 111

5.4.1 Explaining CALET Measurement with Dark Matter Decay . 111

5.4.2 Diffuse $\gamma$-ray Constraint and Allowed Dark Matter Model . . 120

5.4.3 Explaining CALET Measurement with Single Pulsar . . . . 121

5.5 Discerning Dark Matter and Pulsar Model with 5-year CALET Measurement . . . . . 129

5.5.1 Simulated CALET Data assuming Dark Matter Decay as Extra Source . . . . . 129

5.5.2 Simulated CALET Data assuming Single Pulsar as Extra Source . . . . . 132

**6 Conclusion and Discussions** **141**

**Appendices** **143**

**A Energy Distribution of the DM Decay Products** **144**

**B Comparison of Parametrization and GALPROP Calculation** **150**

**C An Update Based on CALET Extended Results** **153**

**Acknowledgment** **158**

# List of Figures


1.1 Schematic diagram of CR acceleration by Fermi mechanism . . . . . 16

1.2 Particle dynamics in the vicinity of astrophysical shock . . . . . 19

1.3 Anti-correlation between solar activity and galactic CR flux . . . . . 29

1.4 Spectrum of major components of CRs over a wide energy range . . . . . 32

1.5 CALET installed on the Japanese Experiment Module-Exposed Facility on the ISS . . . . . 33

1.6 Schematic side view of CALET calorimeter and shower development of TeV electron inside it . . . . 34

1.7 Expected $e^+ + e^-$ spectrum measured with CALET assuming 5 years of observation for the nearby SNR source . . . . . 38

2.1 Galaxy rotation curve and Dark Matter . . . . . 40

2.2 Gravitational lensing and Bullet cluster . . . . . 41

2.3 CMB anisotropies as measured by WMAP . . . . . 42

2.4 Measurement of cosmological parameters from different observations . . . . . 42

2.5 'Freeze-out' mechanism and WIMP . . . . . 46

2.6 Schematic diagram of different DM detection techniques . . . . . 47

2.7 Direct-detection constraint on WIMP mass . . . . . 48

2.8 Differential energy spectrum per annihilation as a function of DM mass . . . . . 50

2.9 Annihilation cross-section bound from observing dwarf spheroidal galaxies with VERITAS . . . . . 50

2.10 Upper limits of DM annihilation cross-section from IceCube neutrino observation . . . . . 51

2.11 DM density as a function of distance from galactic center . . . . . 52

3.1 Schematic diagram of the 2D cylindrical diffusion of CRs in the galaxy . . . . . 55

3.2 Schematic diagram of spatial grid system with 3-D coordinate system in GALPROP . . . . . 61

3.3 Average energy of a particle inside coarse and fine energy bin . . . . . 64

3.4 Energy binning dependence of electron spectrum in GALPROP . . . . . 65

3.5 Effect of energy binning on proton and electron spectrum calculated using GALPROP . . . . . 66

3.6 Effect of modification in GALPROP to mitigate energy binning issue . . . . . 67

3.7 Effect of CR propagation parameters in GALPROP on CR $e^-$ spectrum . . . . . 71

3.8 Spiral arm structure of Milky-way galaxy . . . . . 72

3.9 Proton spectrum and B/C ratio calculation with GALPROP and comparison with AMS-02 measurements . . . . . 73

3.10 Effect of spiral arm thickness on CR $e^-$ spectrum calculated using GALPROP . . . . . 74

3.11 Effect of spiral arm thickness on CR proton and $e^+$ spectrum calculated using GALPROP . . . . . 74

3.12 Effect of time-step parameters in GALPROP on DM annihilation spectrum . . . . . 75

3.13 Self-consistent propagation of CR $e^-$ and DM annihilation spectrum using GALPROP . . . . . 78

4.1 Observance of rise in CR positron fraction with PAMELA, Fermi-LAT and AMS-02 . . . . . 81

4.2 Examples of DM annihilation and milky-way pulsars explaining CR positron excess . . . . . 84

4.3 Fermionic DM model and particle contents of this model . . . . . 87

4.4 Decay of 2 TeV fermionic DM and explanation of AMS-02 measurements . . . . . 91

4.5 Single pulsar explanation of AMS-02 measurements . . . . . 91

4.6 Example of $\gamma$-ray flux associated with DM Decay . . . . . 93

4.7 Decay of 1.5 TeV and 1 TeV fermionic DM as an explanation of CR positron excess . . . . . 95

4.8 Single pulsar fit to simulated CALET data with 2 TeV fermionic DM as extra source . . . . . 99

4.9 Single pulsar fit to simulated CALET data with 1.5 TeV and 1 TeV fermionic DM as extra source . 100

4.10 $\chi^2$ distribution of single pulsar and 2 TeV fermionic DM from fit to simulated CALET data + AMS-02 data . . . . . 101

4.11 $\chi^2$ distribution of single pulsar and 1.5 TeV and 1 TeV fermionic DM from fit to simulated CALET data + AMS-02 data . . . . . 102

5.1 Comparison of $e^+ + e^-$ flux measured by various space-based and ground-based CR detectors . . . 104

5.2 Featureless nature of precise AMS-02 $e^+ + e^-$ spectrum . . . 105

5.3 $e^+ + e^-$ Flux measured by CALET after 1.5 years of observation on ISS . . . 107

5.4 Single power-law fit to CALET data over the complete measured energy range . . . 109

5.5 Single power-law with single pulsar as extra source fit to CALET data over the total measured energy range . . . 110

5.6 Dependece of smoothness term in broken power law of electron . . . 112

5.7 Dependence of minimum $\chi^2$ from fit to CALET + AMS-02 on DM mass . . . 116

5.8 Best-fit of background + 1.1 TeV decaying DM to CALET + AMS-02 for a background cut-off 10 TeV 117

5.9 Best-fit of background + 0.8 TeV decaying DM to CALET + AMS-02 for a background cut-off 10 TeV 118

5.10 Best-fit of background + 0.8 TeV decaying DM to CALET + AMS-02 for a background cut-off 2 TeV 119

5.11 Primary and secondary $\gamma$-ray flux accompanied by DM decay to $ee\nu$ and $\mu\mu\nu$ channel for all the studied models . . . 122

5.12 Dependence of minimum $\chi^2$ from fit to CALET + AMS-02 on single pulsar cut-off energy . . . 125

5.13 Best-fit of background + single pulsar source to CALET + AMS-02 . . . 126

5.14 Comparison of single pulsar parametrization with GALPROP calculation assuming Monogem pulsar 127

5.15 Comparison of single pulsar parametrization with analytical calculation assuming Monogem pulsar . 128

5.16 Fit of single pulsar source to 5 years CALET simulated data assuming DM Model A as extra source 133

5.17 Fit of single pulsar source to 5 years CALET simulated data assuming DM Model B as extra source 134

5.18 Fit of single pulsar source to 5 years CALET simulated data assuming DM Model C as extra source 135

5.19 Distribution of branching ratios of outgoing leptons for DM models obtained from the fitting to CALET simulated data assuming DM as extra source . . . 136

5.20 $\chi^2$ distribution for the fit of single pulsar model to the simulated CALET data with DM Model A as extra source . . . 137

5.21 $\chi^2$ distribution for the fit of single pulsar model to the simulated CALET data with DM Model B as extra source . . . 137

5.22 $\chi^2$ distribution for the fit of single pulsar model to the simulated CALET data with DM Model C as extra source . . . 137

5.23 Fit of 800 GeV DM to 5 years CALET simulated data assuming the pulsar model as extra source . . 139

5.24 Distribution of branching ratios of outgoing leptons for 800 GeV DM, obtained from the fitting to CALET simulated data assuming pulsar as extra source . . . . . 140

5.25 $\chi^2$ distribution for the fit of 800 GeV DM to the simulated CALET data with pulsar model as extra source . . . . . 140

A.1 Feynman diagram of decay of fermionic DM approximated as 4-point interaction . . . . . 144

B.1 Verification of background parametrization by comparing with GALPROP calculation . . . . . 152

C.1 CALET Extended Measurement of $e^+ + e^-$ Flux . . . . . 154

C.2 Best fit of Background + 1.1 TeV DM to CALET (2018) + AMS-02 . . . . . 156

C.3 Best fit of Background + Single pulsar to CALET (2018) + AMS-02 . . . . . 157

# Abstract

The ISS-based CALorimetric Electron Telescope (CALET) detector measures Cosmic Ray (CR) electron + positron spectrum and it is currently in operation from October 2015. Due to an energy resolution of 2% over 10 GeV to several TeV, CALET can detect fine structures in the CR electron + positron spectrum which can originate from astrophysical sources or exotic sources such as annihilation and decay of Dark Matter (DM). To examine the possibility of detecting such signals with CALET, in this thesis, at first CR propagation in our galaxy is discussed. It's shown that with 5 years of CALET simulated data, spectral signatures of TeV scale DM decaying to 3 leptons can be distinguished from a generic single, nearby, young pulsar. Also, using 2 years of precise measurement of electron + positron spectrum with CALET flight data, the spectral features in the spectrum is investigated. Using a broken power-law for the CR electron and a contribution of electron-positron pairs from single pulsar source or DM decay in the spectrum is studied. From the combined comparison with CALET electron+positron flux and AMS-02 positron flux over the energy range from 10 GeV to 3 TeV, allowed range of DM masses and pulsar cut-off energies are calculated. It is shown that 3-body leptonic decay of 800 GeV DM can be one of the last possibilities of DM-only explanation of positron excess without violating astrophysical constraints. Finally, I have discussed the possibility of discerning the signatures produced by decay of such a DM from a generic single pulsar model using CALET data.

# Introduction

Cosmic Rays (CR) are energetic charged particles that hit the earth's atmosphere from all directions. First signature of CRs were measured by Victor Hess on 1912 by measuring the ionization level in the atmosphere which tends to decrease up to $\approx$ 1000m with height and then increases considerably. Robert Millikan confirmed this measurement on 1925 and he gave the name CRs to this radiation. At GeV energy range the CR flux mostly consists of ionized particles, mostly protons and heliums. It also contains various stable nuclei, electrons and not very common components are antimatter particles such as positrons and anti-protons. The intensity of the CRs of energy 1 GeV/nucleon or higher is $1\,\mathrm{cm}^{-2}\,\mathrm{sr}^{-1}\,\mathrm{s}^{-1}$. The CR energy spectrum for the constituents can be represented by a single power law spectrum with spectral index $\sim$ 2.7–2.8 starting from 1 GeV to $10^{15}$ eV [1]. Above this energy ("knee") the slope becomes steep up to $10^{18}$ eV, known as the "ankle" region, and from there a hardening is detected, which probably signifies the presence of extra-galactic component in the CR spectrum. Primary component of CRs when interacts with the Interstellar Medium (ISM) due to spallation produces secondary particles (lighter). Considering the CR propagation secondary particles always refer to these particles and should not be confused with the particles produced in the atmosphere due to interaction.

It's generally believed that primary CRs with energy in the range 1 GeV to the 'knee' region originate in the Supernova Remnants (SNRs), however it is not confirmed yet at different energy region whether isolated supernovae or supernovae in super-bubbles dominates (for a detailed review see here [2]). Diffusive Shock Acceleration (DSA) mechanism at the expanding supernova shells are widely accepted as the responsible process for CR acceleration. The DSA process is first order Fermi

acceleration process in presence of strong shock waves and naturally explains the power law spectrum with index $\approx 2$ [3, 4]. These accelerated CRs then propagate in the ISM and interacts with the galactic magnetic field. The charge particle interaction with the ISM and the random motion can be described by diffusion equation [5]. The charge particles may also interact with the traveling oscillations of ion density in the magnetized plasma which can stochastically reaccelerate the CR particles and this process is known as diffusive reacceleration. Once the CR particles reach the solar system it interacts with solar wind and the effect is known as solar modulation.

CR particles finally when arrive in the proximity of the earth, they can be detected by various space or balloon borne particle detector (Ex. Fermi-LAT, PAMELA, AMS-02, CALET, CREAM, TRACER, etc.) [6–11]. The balloon experiments have several limitations due to statistical and systematic uncertainty coming from less flight-time and residual atmospheric overburden (Ex. In CREAM experiment at altitude 38–40 km, atmospheric overburden is 3.9gm/cm$^2$) compared to the space-based experiments (Ex. AMS-02 and CALET in International Space Station orbit earth at an altitude of $\sim$ 400 Km). CALET (CALorimetric Electron Telescope) is a calorimetric detector deployed in ISS on August 2015, and collecting data from October 2015. The primary science goal of CALET is the precise measurement of CR $e^- + e^-$ flux with a fine energy resolution (better than 2% above 100 GeV) from 1 GeV to 20 TeV, extending the highest energy observed by AMS-02 ($\sim$ 1 TeV). CALET also measures CR nuclei up to several 100 TeV and gamma-rays up to 10 TeV energy range. Previous calorimeter type experiments, such as Fermi-LAT is not optimized for electron observation and the thick calorimeter of CALET ensure precise $e^- + e^+$ spectrum measurement well into TeV region. Measuring TeV region of the $e^- + e^+$ spectrum directly with CALET and due to its high proton rejection ratio ($1 : 10^5$) and fine energy resolution, will address many long standing questions in the CR physics such as the origin of the CRs, propagation and acceleration mechanism in the galaxy and existence of nearby CR sources such as pulsars and Supernova Remnants (SNRs). Even though CALET cannot distinguish between electron and positron, but because of the aforementioned properties it can detect distinctive features in the $e^+ + e^-$ spectrum which may arise from the DM decay or annihilation. Using the precise measurement from CALET the spectral

features of $e^+ + e^-$ spectrum is studied in detail in this thesis work. The thesis is organized as follows:

In Chapter 1 the general understanding of CR acceleration mechanism and propagation in the milky way galaxy is described. As a part of the DM detection study with CALET, indirect DM detection techniques and relevance to CR physics is discussed in chapter 2. In Chapter 3, different methods for solving CR propagation equation is described. GALPROP numerical calculation tool is used extensively for the propagation of charged particles in galaxy. It is shown that the GALPROP calculation depends on the energy bin size and a modification in the GALPROP source code was implemented to partly mitigate this problem. In Chapter 4, it is shown that with 5 years of CALET simulated data, a fermionic DM decay as extra source of positrons can clearly be distinguished from a generic single pulsar source spectrum. For this study, AMS-02 measurement of $e^+ + e^-$ and $e^+$ flux measurements are used to determine the best fit models for DM decay scenario, which was used to simulate CALET data. However in Chapter 5, using 1.5 years of precise $e^+ + e^-$ flux measurement by CALET up to 3 TeV and AMS-02 $e^+$ flux up to 500 GeV are considered for a combined interpretation with DM decay or pulsar as extra source. Assuming a smoothly broken power-law and either pulsar or DM decay as extra source of electron-positron pairs, allowed range of DM masses and pulsar cut-off energies are determined. We have shown that depending upon the mass of DM and branching ratio of the outgoing particles from the DM decay, it is possible to explain combined CALET all electron and AMS-02 positron flux measurement, bypassing the $\gamma$-ray constraints coming from Fermi-LAT measurement. Based on the best-fit to 1.5 years of CALET flight data + AMS-02 positron flux, CALET 5 years data is simulated. Assuming the full exposure of CALET and 5 years of data-taking, possibility of discerning DM decay signal from a generic pulsar case was discussed. Finally in the conclusion of the thesis a review of the results, implications and the future plans using CALET's precise measurement are described in Chapter 6.

# Chapter 1

# Cosmic Ray Sources, Propagation and Observation

## 1.1 Sources and Acceleration of Primary Cosmic Rays

CRs are charged particles and during the propagation they get deflected randomly in the interstellar magnetic field, making it extremely difficult to track back their origin. However, supernova remnants (SNR) are commonly accepted to be the origin of galactic CRs for energies up to $10^{15}$ eV [12]. Supernova explosions with few percent of efficiency can accelerate the galactic cosmic rays and this can be shown with a simple calculation. The interstellar CR energy density ($\rho_E$) is $\sim 1\text{eV/cm}^3$ [13] and for simplicity we can assume this density is maintained throughout the galactic disk. So the power necessary to supply all the galactic cosmic rays is $P = \frac{V\rho_E}{\tau_T}$, where $V$ is the volume of the galactic disc, and $\tau_T$ is the residence time of the CRs in the galactic disc where the CR sources are distributed. To calculate the volume of the galactic disc, we assume it's radius 20 kpc and height 200 pc [1], so $V_D = \pi(20)^2\,200 \approx 7 \times 10^{66}\text{cm}^3$. The estimated time spent by CRs in the volume $V_D$ is $\sim 4 \times 10^6$ years [14]. So, the total power needed to supply all the galactic

[1] 1 pc $\approx 3 \times 10^{18}$ cm

CRs is

$$P = \frac{7 \times 10^{66} \times 1.6 \times 10^{-19} \text{Joules}}{4 \times 10^{6} \text{ years}}$$
$$P = 2.8 \times 10^{41} \text{Joules year}^{-1}. \tag{1.1}$$

Now if a type II Supernova of mass around 10 $M_{\odot}$ explodes and eject material with velocity of the order $10^8$ cm/s, then 2-3 events like this in every century and a transfer of only 1% of their kinetic energy should be sufficient to explain the observed CR energy density in the galaxy [15]. Also, it was shown in this work [16], that spherical shock from SN explosions can accelerate the particles to high energies, and the scattering off the Alfven waves confine the particles near the shock region and results in first order Fermi acceleration. Fermi acceleration is described later in short, as this mechanism can explain the power law behavior of the observed CRs.

The original theory proposed by Fermi explains the particle confinement in the galactic magnetic field and subsequent acceleration in the irregularities of the magnetic field known as *magnetic mirrors* [17]. Considering a relativistic particle of energy $E_0 = p_0 c$ encounters such a massive magnetic cloud of infinite mass and velocity $v_m$, the particle energy in the coordinate system of the cloud will be given by

$$E_0^* = \gamma_m \left(E_0 + \beta_m p_0\right) \ , \tag{1.2}$$

where $\beta_m = v_m/c$ and $\gamma_m = \frac{1}{\sqrt{1-\beta_m^2}}$. For simplicity, it's assumed that the particle scatters many time in the magnetic cloud and eventually comes out of the cloud in a direction collinear and opposite to the initial direction. For point particles and infinitely massive magnetic mirror, the collision can be assumed to be elastic and the particle energy when it comes out of the cloud is

$$E_1 = \gamma_m \left(E_0^* + \beta_m p_0^*\right) = E_0 \times \gamma_m^2 \left(1 + \beta_m\right)^2 \ . \tag{1.3}$$

So the relative gain in energy of the particle

$$\frac{\Delta E}{E_0} = \frac{E_1 - E_0}{E_0} = \gamma_m^2 (1 + \beta_m^2) - 1 \equiv \eta \ , \tag{1.4}$$

is proportional to the square of the velocity of the magnetic cloud. In this case the assumption was particle comes out at a direction opposite to the initial entry

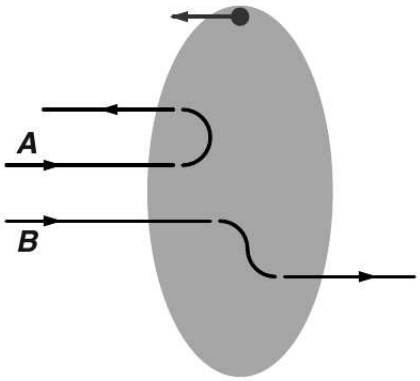


Figure 1.1: Schematic diagram of particle acceleration in magnetic cloud (grey region) due to scattering, as proposed by Fermi. Particle scattering and exit direction opposite to the entrance as shown with A, is energy gaining process. If the exit direction is along the entrance direction (shown with B), no energy is gained by the particle. If the particles enter the cloud at a direction parallel to the cloud velocity (shown with left arrow on top), particle loses energy. Image reference [18].

direction. However, it is shown here [4] the gain in energy depends strongly on the relative angle of entrance and exit. So a particle will not gain any energy if it exits in the same direction it enters. This is shown via the schematic diagram 1.1 where particle gains energy if it follows the path A and remains the same if it follows the path B. If the particle velocity direction coincides with the cloud velocity direction, then the particle loses energy. A test particle after $i$ encounters will have an average energy

$$E_i = E_0(1+\eta)^i \ . \tag{1.5}$$

If the probability of a particle remaining in the acceleration region is given by $P$, then after $i$ encounters, particles in the accelerating region is given by

$$N = N_0 P^i \ , \tag{1.6}$$

where $N_0$ is the number of particle before entering in the accelerating region. Eliminating $i$ from the above two equations give

$$\frac{\ln\,(E_i/E_0)}{\ln\,(1+\eta)} = \frac{\ln\,(N/N_0)}{\ln P} \ . \tag{1.7}$$

The number of particles that are accelerated to energies higher or equal to $E$ is $N$. In a more compact form it can be written as

$$N(E)dE = \text{constant}\, E^{\frac{\ln P}{\ln(1+\eta)}-1}\, dE\,, \tag{1.8}$$

which implies a power-law energy distribution for the particles and it depends on the square of the velocity of the magnetic clouds $v_m^2$. Due to this dependence this process is often called as second-order Fermi acceleration process. This stochastic acceleration proposed by Fermi can explain the power law behavior of CR spectrum. However, apart from the fact that this mechanism cannot predict the value of the exponent of the energy spectrum, there are other problems with this model of acceleration. The energy gain per unit time depends on the frequency of the collision ($\nu_{\rm enc}$) in the magnetic clouds, so $\frac{dE}{dt} = \nu_{\rm enc}\Delta E = \frac{c}{\lambda_{\rm enc}}\eta E = \frac{\eta E}{T_{\rm enc}}$, where $\lambda_{\rm enc}$ and $T_{\rm enc}$ are the mean free path between magnetic clouds and characteristic time per encounter, respectively. This suggests that reaching higher energy requires longer time, making the acceleration process very slow. As the energy gain per encounter is proportional to $\beta_m^2$, which is of the order $10^{-7}$, and the mean free path for the scattering of CRs in the interstellar medium is of the order of 0.1 pc, making few collisions per year, resulting in a very slow gain of energy. This suggests that, places with small scale turbulence and velocity of the magnetic turbulence much greater than the interstellar medium, will act as a better accelerator. Expanding shells of SNRs satisfy these requirements.

The well known Diffusive Shock Acceleration (DSA) theory with a first order in velocity of the magnetic clouds can explain the power-law behavior with an energy index $\approx 2$. One of the biggest problem of second-order acceleration of mechanism was chances of particles losing energy when they enter the cloud along the direction of cloud velocity. The scenario however changes if we consider a model involving a strong shock propagating through the ISM. In this model, the strong shocks are formed because the expansion velocity of the remnants are much higher than the velocity of sound in ISM. The shock runs ahead of the expanding SNR and the shock velocity depends on the expansion velocity of the SNR and the ratio of specific heats of the shocked and unshocked media. The high energy particles barely notice the shock since the average gyro radius of these particles are much higher than the shock thickness. Because of collisionless scattering on either side of the shock the particles crossing the shock get scattered in the corresponding media

and the velocity distribution is isotropized. The high energy particles crossing the shock-wave undergoes head on collision irrespective of their direction of crossing. This can be understood from the schematic figure 1.2 where it's shown that as seen from the laboratory reference frame we consider a shock wave propagating to the right with velocity $U$, greater than velocity of sound in the medium. Considering from the shock frame the upstream gas flows at the shock with a velocity $V_1 = U$. When the gas leaves the shock from the reference frame of shock it has velocity $V_2$. This velocity can be determined from the continuity equation resulting from the conservation of mass at the shock boundary $\rho_1 V_1 = \rho_2 V_2$. Considering a strong shock the ratio of densities can be written in terms of specific heat ($C_v$) of the gas as $\frac{C_v+1}{C_v-1}$. For a fully ionized media, the gas molecules are considered as mono-atomic and we get $V_2 = \frac{1}{4} V_1$. Now we consider the whole scenario from the reference frame of gas ahead of the shock. Even though the shock advances with the velocity $U$, the gas behind advances with a velocity of $3U/4$. Similarly, for gas particles diffusing from behind the shock to the upstream region will also experience the gas ahead advances with a velocity $3U/4$. In other words particles from both side of the shock experience the same procedure of energy gain through collision. The gain in energy of the particles in presence of shock depends on the first order of the velocity of the magnetic clouds and this process is often referred as first-order Fermi acceleration process. By studying the behavior of individual particles in the presence of strong shock waves, it can be shown that the power-law behavior of energy spectra with unique spectral index is common in presence of strong shock waves [3,16]. Referring back to eq. 1.8, it can be shown that in DSA, $\frac{\ln P}{\ln (1+\eta)} = -1$, so the differential energy spectrum of the high energy particles can be written as

$$N(E)\, dE = \text{constant}\, E^{-2} dE\,. \tag{1.9}$$

It is shown in this work [19], following DSA, there's an upper limit of energy that can be obtained from this process. The acceleration mechanism continues throughout the life of supernova for $10^5$–$10^6$ years, until it dissolves in the ISM. However most of the acceleration of the particles occur during the earlier phases within $10^3$ years. Assuming ISM density of 1 nucleon per cubic centimeter, the upper limit of the energy that can be achieved through this process is around $3 \times 10^4$ GeV. Apart from the standard models of acceleration of CRs, non-linear diffusive acceleration model is also important, which is however not used in the thesis work.

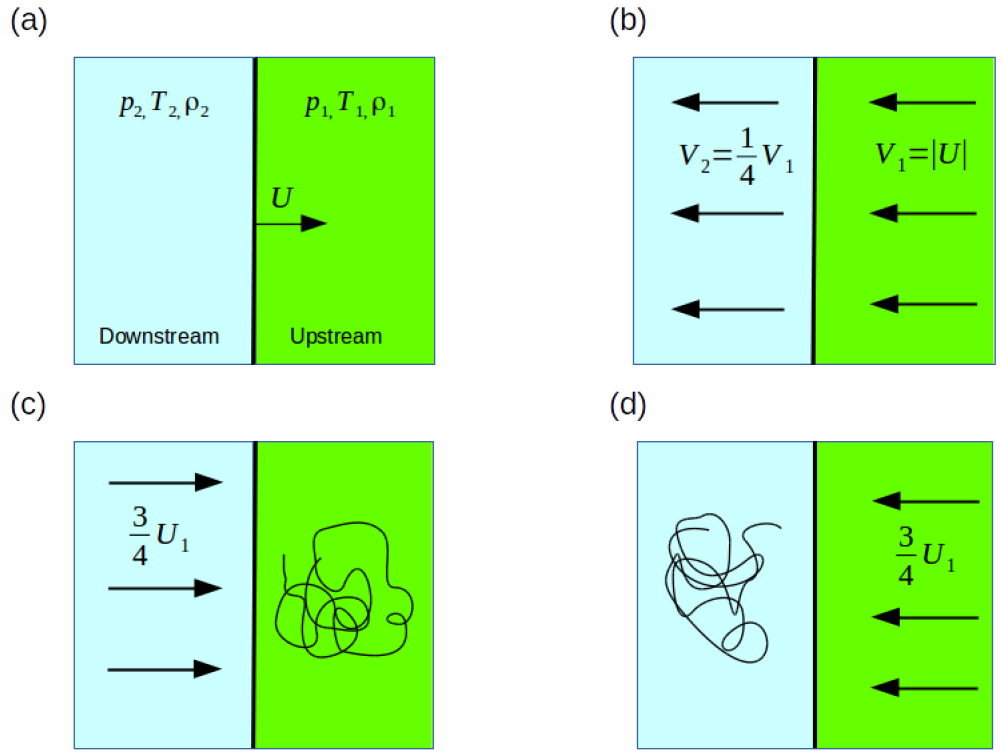


Figure 1.2: Schematic diagram of particle dynamics around a strong astrophysical shock wave (thick black line) where the upstream and downstream region are shown with green and cyan colors. (a) Velocity of shock ($U$) as seen from the lab frame. (b) Velocities of upstream and downstream media as seen from the shock wave frame. (c) Flow of gas from the medium behind the shock as seen from the upstream frame. (d) Flow of gas from the medium ahead of the shock as seen from the downstream frame. Velocity of individual particles are highly isotropic in both upstream and downstream region. Image is recreated using reference from Longair book [4].

## 1.2 Interstellar Medium and Galactic Magnetic Field

Interstellar Medium (ISM) is mainly made up of gas and it mostly consists of Hydrogen (Helium and other heavier nuclei are responsible for only 10 % of the gas) [20]. The atomic Hydrogen (HI) is detected by the 21 cm radio emission line and the molecular hydrogen ($H_2$) distribution is traced by observing the 2.3 mm CO line [21]. During the propagation of CRs, interaction with interstellar gas produces lighter secondaries due to fragmentation, antiparticles. The interstellar gas distribution plays an important role in the diffuse $\gamma$-ray production as the hadronic part of the CR interacts with ISM and produce pions ($\pi$), which decays to photons. Also the CR electrons and positrons interact with the ISM and produce $\gamma$-rays through Bremsstrahlung and inverse Compton scattering (IC). The ISM has important role in CR astrophysics since not only it causes the secondary production and diffuse $\gamma$-ray, the magnetic field present in the ionized gas is responsible for CR diffusion, which is described later.

ISM also consists of interstellar dust, which mostly contain the heavy elements present in the ISM. The heavy elements account for 1% of mass in the ISM. When the Supernova and dying stars eject heavy elements, interstellar dust form in the regions where the temperature are below $10^3$ K, the sublimation temperature. Dust grains either absorb or scatter light that pass through them, and from observation we can deduce the composition of the dust grains [4].

The ISM gas is mostly concentrated at the galactic plane and they move in circular orbits about the galactic center. The average rotational velocity of the gas is fairly constant with increasing distance from the galactic center. This is in contradiction with the Keplerian dynamics and can possibly provide evidence for DM in the galaxy [22].

The galactic magnetic field is one important component of ISM and there are several experimental techniques to determine it. By observing galaxies with discs perpendicular to the line of sight and measuring the optical, radio and infrared emission, basic information of galactic magnetic field is obtained [23]. The galactic

magnetic field values are measured using Faraday rotation, where the polarization plane of linearly polarized radio emission passes through plasma containing free electrons and embedded magnetic field. Due to this, the linearly polarized waves get rotated and positive (counterclockwise) rotation occurs when the magnetic field is directed towards the observer and vice versa. Faraday rotation is defined as $\psi = \lambda^2 \int n_e B_\parallel dl$, where $n_e$ is the number of thermal electrons along the line of sight, $B_\parallel$ is the magnetic field along the line of sight, $dl$ is the path length in parsec, and $\lambda$ is the wavelength of the observed emission [4]. The galactic magnetic field can be divided into two parts, known as random and regular field, and it is generally accepted that Milky Way has a large scale organized field. The regular field is measured by Faraday rotation method as described before and it is defined as

$$B(R, Z) = B_0 \exp\left(-\frac{r - r_\odot}{r_h}\right) \exp\left(-\frac{z}{z_h}\right) , \tag{1.10}$$

where $B_0$ is the local magnetic field strength and $r$, $z$ are the galactic radius and height. The values of the parameters are determined from the measured synchrotron radiation and extragalactic rotation measurements [24,25]. It is later shown in detail about the uncertainties related with the halo parameters such as radius and halo height and the consequences on CR propagation.

## 1.3 Models for Cosmic Ray Propagation

### 1.3.1 Leaky Box Model

CR confinement in ISM and propagation can be described by a simple model known as Leaky Box (LB) model [26], where the CR particles are confined in the galaxy and then slowly escape to intergalactic space with certain probability. The main assumptions in this model are

- The CR sources are distributed uniformly in the galactic volume.
- Variation of CR densities in the ISM is neglected and instead an uniform density is assumed.

- CRs are preaccelerated at the source with identical spectra and no acceleration occurs during propagation (ex. reacceleration).
- Escape of CRs from the confinement volume depend upon the energies of the CR particles.
- Within the confinement volume the CR particles get reflected at the boundaries and the loss of particles is parametrized with the escape time ($\tau_{\rm esc}(E)$) from the volume and this is shorter at higher energy. Higher the energy of the particle, shorter is the time spent in the volume.

The number density of the CR particles ($n_i$), where $i$ denotes species, in the LB model is described as

$$\frac{dn_i}{dt} = -\frac{n_i}{\tau_{\rm esc}} + Q \ , \tag{1.11}$$

here $Q$ denotes the source term. Here we assume no collision and other energy changing processes are involved. Solution of eq. 1.11, for a delta-function source ($Q(E) = n_{i0}\delta(t)$) is $n_i(t) = n_{0i}e^{-t/\tau_{\rm esc}}$. The escape time of the CRs are related to the escape length ($\lambda_{\rm esc}$) as, $\lambda_{\rm esc} = \rho\beta c\tau_{\rm esc}$. Here, $\rho$ is the mean density of the interstellar gas and $\beta c$ is the particle velocity. The escape length for different nuclei species is obtained from their relative abundances and the constraint comes from the secondary to primary ratio measurement. The energy dependence of primary to secondary ratio is coming from the energy dependence of $\lambda_{\rm esc}$, which is given by $\lambda_{esc} = 34.1\beta\left(\frac{1}{R}\right)^{\delta}$ g cm$^{-2}$ and $\delta = 0.6$ for $R > 4.4$ GV, and $\lambda_{\rm esc} = 14.0\beta R$g cm$^{-2}$ for $R < 4.4$ GV. Here $R$ and $\beta$ are the rigidity and ratio of particle velocity to velocity of light in the ISM [27]. Now, adding a particle loss term due to collision in the ISM in eq. 1.11,

$$\frac{dn_i}{dt} = -\frac{n_i}{\tau_{\rm esc}} - \frac{\beta c\rho}{\lambda_i}n_i + Q \ , \tag{1.12}$$

During the steady state the left hand side of the eq. 1.12 vanishes and we are left with

$$\frac{n_i}{\tau_{\rm esc}} + n_i\frac{\lambda_{\rm esc}}{\tau_{\rm esc}} = Q \tag{1.13}$$

For a primary nucleus the solution of eq.1.13 has the form

$$n_i = \frac{Q\tau_{\rm esc}}{1 + \lambda_{\rm esc}/\lambda_i} \tag{1.14}$$

For nuclei with $\lambda_i >> \lambda_{\rm esc}$ (e.g. Proton), $n_i = Q\tau_{\rm esc} = QE^{-\delta}$. So the observed spectrum of protons are steeper than the injected spectrum by an amount $\delta$. Iron nuclei which have interaction length less than the escape length ($\lambda_i << \lambda_{\rm esc}$), the low energy iron nuclei interact and get destroyed before they could escape, therefore the iron spectrum reflects the source spectrum $n_i \propto Q$. With increasing energy $\lambda_{\rm esc}$ decreases and energies at which $\lambda_i \sim \lambda_{\rm esc}$, the iron spectrum is indeed steeper as observed in experiments [28, 29].

Even though most of the CR nuclei data and some general CR physics can be explained by LB model [27–31], it fails to explain the ratio of unstable to stable isotope ratio such as $^{10}$Be/$^{9}$Be. Since the half-live of the radioactive Be isotope is close to the escape time ($\tau_{\frac{1}{2}} \sim \tau_{\rm esc}$), the abundance of $^{10}$Be can be used to deduce the density of the gas in ISM [32]. The ratio suggest that the gas density is around $0.3\,{\rm g\ cm^{-3}}$, which is much less than the density in the disk (one hydrogen atom per cubic centimeter). This suggest that CRs not only spend time in the disk but they diffuse to the galactic halo where the gas density is much less. Also the abundance of secondary nuclei such as Boron (B), which is the result of interaction of primary Carbon (C) with the ISM suggests that the column density of gas is much more than the observed average column density along the line of sight. This leads to the conclusion that CR particles do not travel in straight lines but confined in the galaxy for a much larger time than the expected.

### 1.3.2 Diffusion Model

LB is one simple but effective model to describe the CR propagation in galaxy. However, the actual propagation of CRs can be understood using the diffusion model where the interaction of the CRs with ISM magnetic field (described before) can provide a mechanism for the confinement in the galaxy. The important differences between the LB model and diffusion model are

- In the steady state CR distribution is uniform in LB model in contrast to diffusion model where, there exists a density gradient.
- The LB model can be considered as a first order approximation of diffusion

model and this is valid for stable nuclei such as proton whose energy changing processes are slow. But as mentioned before when the interactions occur in the halo and the disk of the galaxy then LB model fails and diffusion model comes into play.

- The CR source distribution in the galaxy is usually assumed to be uniform in the LB model, whereas the spatial distribution function of the supernovae is given by [33]

$$Q = Q_0 \left(\frac{r}{r_\odot}\right)^\eta \exp\left(-\xi \frac{r - r_\odot}{r_\odot} - \frac{|z|}{0.2}\right) , \tag{1.15}$$

where $Q_0$ is the normalization constant, $r$ is taken as $\sqrt{X^2 + Y^2}$, $r_\odot$ is the distance of the solar system from the center of the galaxy, 0.2 (kpc) is the characteristic height of the galactic disk and the constants $\xi$, $\eta$ are determined from the diffuse $\gamma$-ray emission and $H_2$ to CO ratio [33, 34].

Actual CR propagation process is more complex than the simple LB model considerations, where CR particles escape the confinement volume with constant probability. As mentioned before the galactic magnetic field is one of the important components of ISM. The CR particles get scattered by the irregularities in the magnetic field and the CR propagation is usually described as diffusion from the source to the ISM. This also explains the isotropic distribution of high energy CRs and their long confinement time in the galactic volume.

The complete equation that describes CR propagation in galaxy can be written as [34]

$$\begin{aligned} \frac{\partial n\left(\vec{r},\, p,\, t\right)}{\partial t} &= Q\left(\vec{r},\, p,\, t\right) + \vec{\nabla} \cdot \left(D_{xx} \vec{\nabla} n - \vec{V_c} n\right) \\ &+ \frac{\partial}{\partial p} p^2 D_{pp} \frac{\partial}{\partial p} \frac{1}{p^2} n - \frac{\partial}{\partial p}\left[\dot{p} n - \frac{p}{3}\left(\vec{\nabla} \cdot \vec{V_c}\right) n\right] - \frac{1}{\tau_f} n - \frac{1}{\tau_r} n \,, \end{aligned} \tag{1.16}$$

where each term is explained below.

- $n\left(\vec{r},\, p,\, t\right)$ is the CR density with momentum $p$ at a position $\vec{r}$. In terms of phase-space density $(f(p))$ it can be written as $npdp = 4\pi p^2 f(p) dp$.

- $Q\left(\vec{r},\, p,\, t\right)$ is the source term, which includes the contribution from primary sources and also contribution from decay and spallation of heavier nuclei.

- $\vec{\nabla} \cdot \left( D_{xx} \vec{\nabla} n \right)$ describes the spatial diffusion process of CR particles and $D_{xx}$ is the spatial diffusion coefficient. The process of diffusion is usually assumed to be isotropic. Diffusion coefficient as a function of rigidity ($R = \frac{p}{Ze}$) can be written as

$$D_{xx} = \beta D_0 \left( \frac{R}{R_0} \right)^{\delta} , \tag{1.17}$$

where $\delta$ depends on the relativistic motion of charged CR particles in the magnetized plasma. Value of $\delta$ is typically $\frac{1}{3}$ in Kolmogorov type diffusion whereas, $\delta \sim \frac{1}{2}$ for Kraichnan type diffusion and detailed theoretical descriptions of these two models can be found here [35, 36]. At very high energies the propagation is dominated by diffusion process and for nuclei the energy loss processes are negligible. In this case eq. 1.16 reduces to $\frac{\partial n(\vec{r},p,t)}{\partial t} = Q\left(\vec{r},\, p,\, t\right) + \vec{\nabla} \cdot D_{xx} \vec{\nabla} n$. Now comparing with eq. 1.11, we see that the diffusion term can be replaced by $-\frac{n}{\tau_{\rm esc}}$ in the LB model. This is the reason why LB model can be used for nuclei to describe CR propagation in a simplistic way.

- Continuing from the previous point, a comparison of diffusion equation and LB model equation at high energies leads to equation of the form $\frac{\partial n(\vec{r},p,t)}{\partial t} = Q(\vec{r},\, p,\, t) - \frac{n}{\tau_{\rm esc}}$. In the steady state $Q = \frac{n}{\tau_{\rm esc}}$. So if we assume a power law spectrum for the primary sources (ex. $E^{-\gamma}$) then the observed primaries will have a power law behavior given by

$$n_{\rm prim} \propto E^{-\gamma} \tau_{\rm esc} \propto E^{-\gamma} D^{-1} \propto E^{-\gamma-\delta} .$$

Similarly, the energy dependence of the CR secondaries will be

$$n_{\rm sec} \propto n_{\rm prim} P_{\rm frag} \tau_{\rm esc} \propto E^{-\gamma-\delta} D^{-1} \propto E^{-\gamma-2\delta} ,$$

where $P_{\rm frag}$ is the fragmentation probability of the primary particles. From this the ratio of secondary to primary CR particles at high energies will be given by $\frac{n_{\rm sec}}{n_{\rm prim}} \propto E^{-\delta}$. This is important as measurement of B/C ratio at high energies will tell us the information about diffusion coefficient index $\delta$.

- $\vec{\nabla} \cdot \vec{V_c} n$ represents the change in CR density due to convection and $\vec{V_c}$ is the convection velocity. Even though diffusion is the most common mode of CR transport but presence of galactic winds suggest convective transport. In this

process it's usually assumed that convection velocity varies linearly with the distance from the galactic plane as

$$V_c(z) = \frac{dV_c}{dz} z \,, \tag{1.18}$$

where velocity gradient is a free parameter.

- $\frac{\partial}{\partial p} p^2 \, D_{pp} \frac{\partial}{\partial p} \, \frac{1}{p^2} \, n$ is the diffusion term in momentum space which is known as diffusive reacceleration. This process describes the stochastic acceleration (2nd order Fermi acceleration) of CR particles in the randomly moving magnetohydrodynamic (MHD) waves which is already discussed in section 1.1. The relation between the diffusion coefficient in momentum space $D_{pp}$ and the spatial diffusion coefficient is

$$D_{pp} D_{xx} = \frac{4 p^2 v_a^2}{3\delta(4-\delta^2)(4-\delta)} \,, \tag{1.19}$$

where $v_a$ is called Alfven velocity, characteristic velocity of the weak disturbances propagating in the magnetic field [37].

- $\frac{\partial}{\partial p} \dot{p} n$ represents the change in CR density due to energy loss during the propagation in ISM. In in this thesis work propagation and energy loss processes for electrons are important and inverse Compton scattering and synchrotron radiation as the main processes of energy loss of CR electrons are described in brief here. Energy loss due to synchrotron radiation is given by

$$-\left(\frac{dE}{dt}\right) = 2\sigma_T U_{\rm mag} \gamma^2 \sin^2\alpha \tag{1.20}$$

here $U_{\rm mag} = \frac{B^2}{2\mu_0}$, and Thomson cross-section $\sigma_T = \frac{e^4}{6\pi\epsilon_0^2 m_e^2}$ and $\alpha$ is the pitch angle, the angle between velocity vector and magnetic field vector [4]. Average energy loss due to synchrotron radiation is given by averaging over the isotropic distribution of pitch angles $p(\alpha)d\alpha = \frac{1}{2}\sin\alpha \, d\alpha$ and the result is

$$\begin{aligned} -\left(\frac{dE}{dt}\right) &= 2\sigma_T \, U_{\rm mag} \gamma^2 \frac{1}{2} \int_0^\pi sin^3\alpha \, d\alpha \\ &= \frac{4}{3} \sigma_T \, U_{\rm mag} \gamma^2 \end{aligned} \tag{1.21}$$

This is similar in nature with the loss due to inverse Compton scattering, where relativistic electrons scatter low energy photons to high energies and in

this process they lose energy. The loss due to IC scattering is given by

$$-\left(\frac{dE}{dt}\right) = \frac{4}{3}\sigma_T\, U_{\rm rad}\gamma^2 \tag{1.22}$$

where $U_{\rm rad}$ is the average density of the optical photons and CMB photons given by $U_{\rm rad_{ph}} \approx 6\times10^5 {\rm eV\,m^{-3}}$, and $U_{\rm rad_c} = 2.65\times10^5 {\rm eVm^{-3}}$ respectively [4]. Effect of the energy loss processes on CR electron spectrum are described later.

- $\frac{\partial}{\partial p}\left[\frac{p}{3}\left(\vec{\nabla}\cdot\vec{V}\right)n\right]$ is the convection term in the momentum space.
- $\tau_f$ is the timescale for density loss due to fragmentation.
- $\tau_r$ is the characteristic timescale for density loss due to radioactive decay.

Effect of the propagation parameters are described in detail later when CR propagation calculation and results are shown in Chapter 3.

## 1.4 Solar Modulation

Since almost all the CR detectors are within the heliosphere of the solar system, the turbulent solar wind and the embedded magnetic field play an important role in the observed CR spectrum. Among the space based detectors Voyager 1 for the first time on 2012 passed the heliopause and measured the LIS directly for the first time [38]. The solar wind originates in the solar corona and the magnetic field is frozen in the ionized material, which is dragged outwards from the Sun [4, 39]. The charged particles undergo convection and adiabatic deceleration and continuously lose energy. Several complex processes inside the heliosphere like diffusion due to magnetic irregularities in the heliospheric magnetic field, particle drift in the large scale magnetic field, outward convection by solar wind, adiabatic energy losses are quantified by Parker's equation [40]. The physics of the solar wind and the particle interaction with the frozen magnetic field in the solar wind is a vast topic of research in solar physics, and it is beyond the scope of this thesis work.

However, the problem of solving the Parker's equation can be reduced to a 1D spherically symmetric case using force-field approximations [41]. The force-field

model is the most commonly used model for describing solar modulation potential and the approximations are - 1) The solar wind is moving with a constant speed radially outward, 2) The diffusion tensor is isotropic and there's no drift (antisymmetric parts of diffusion coefficients are neglected), 3) There isn't any adiabatic energy loss and the system is in quasi-steady state (i.e. $\frac{\partial f}{\partial t} = 0$, where $f$ is the CR distribution function). With these assumptions, the Local Interstellar Spectrum (LIS) and the observed spectrum is related by

$$J(E,\, Z,\, A) = \frac{E^2 - m^2}{(E + \frac{Ze}{A}\phi^2)^2 - m^2} J_{\rm LIS}(E + \frac{Ze}{A}\phi,\, Z,\, A)\ , \tag{1.23}$$

where Z, A, m are atomic number, mass number and mass of the CR particle. The effect of solar modulation is described by the parameters $\phi$, known as the modulation potential. CRs with energies below 10 GeV can be significantly affected by the solar modulation and they get decelerated. Solar modulation potential is charge dependent and it also varies with time as shown in figure 1.3, by data taken at time different time with CLIMAX neutron monitor. It shows anti-correlation of count rates with the solar activity. When the sunspot number increases i.e. solar activity increases, increase solar wind results in more interaction with the CR particles and they lose energy. As a result the CR intensity decreases so the galactic cosmic ray intensity is anti-correlated with solar activity.

## 1.5 Cosmic Ray Observation

To understand the nature and properties of CRs many experiments were performed in the last century and many more are detectors are currently in operation. Basic principle of CR detectors is to identify particles through interaction with the detector material. CRs when reaches earth, it interacts with the atmosphere and as a consequence they cannot be measured directly in the ground. Instead, the air-showers they create can be detected indirectly in the ground based observatories. Depending on the particle energy the air-showers can spread over a large distance, and at higher energies the CR flux is extremely low (see figure 1.4), consequently large detectors are needed for accurate measurement of the showers. CR particles can directly be measured or detected in space and this is usually achieved through

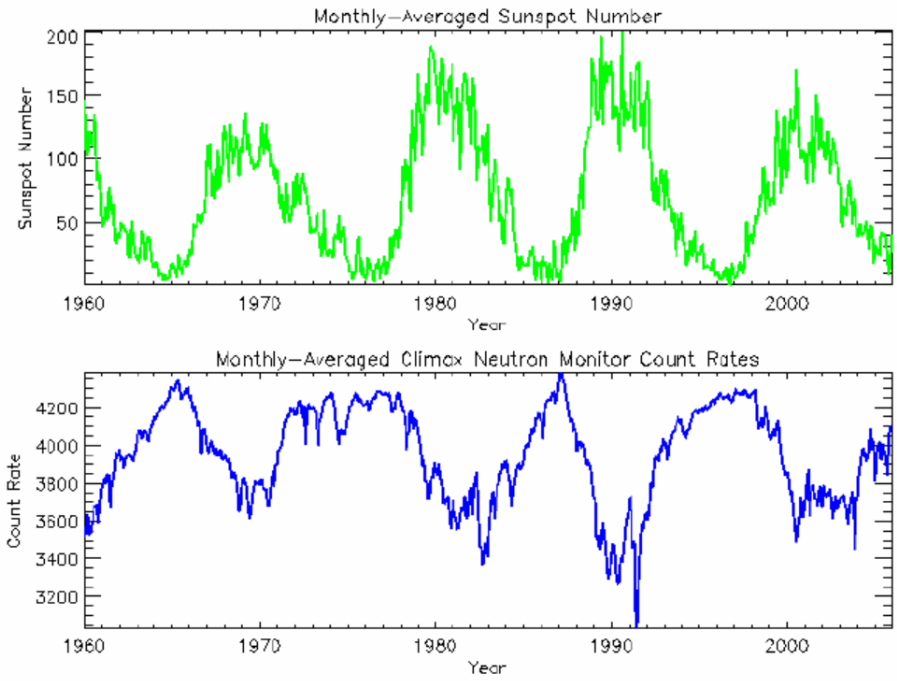


Figure 1.3: The anti-correlation between solar activity and galactic CR flux is shown by comparing the sun spot numbers (green line) with the neutron count rates (blue line) from the CLIMAX neutron monitor. Top panel shows the monthly averaged sun spot numbers from 1960 to 2005. Bottom panel shows the monthly averaged neutron monitor count rates from the CLIMAX neutron monitor [42].

satellite missions which operate at near earth orbit or via balloon flights that reach the height of the stratosphere.

First signature of CRs through radiation were measured by Victor Hess with balloon borne detector on 1912 during a solar eclipse to rule out the Sun as source of radiation. Using direct measurement of CRs the constituent particles are discriminated through energy and abundance. Balloon-borne detectors have longest history in CR detection as they allow multiple flights with a moderate budget and act as prototype tests for the space borne detectors for example balloon observation with CALET prototype [43] has been performed before the CALET detector was deployed in ISS [44, 45]. A number of balloon-borne detectors (ex: TRACER [11], ATIC [46], CREAM [10]) in the past two decades including provided some important results in CR physics. The limitations of balloon-borne detectors are coming from the limited exposure time and atmospheric overburden. Even though space missions are highly expensive, they ensure much longer period of observation, no atmospheric overburden and better systematics. Since CALET detector and its CR observation capabilities are important subject of this thesis, a more detailed description about it is given in the next section. Compared to the balloon experiments which operate at an altitude $\approx 40$ kms, space based detectors operate orbiting earth at height around $400-600$ kms. Various types of space based CR detectors are currently in operation now (ex. Fermi [6] AMS-02 [8], CALET [44], DAMPE [47, 48]) and upcoming high-precision data will uncover many mysteries in the near future. Compared to PAMELA [7] and DAMPE, which are a satellite based mission, AMS-02 and CALET are ISS based mission. Measurement of CRs over a wide energy range with fine energy resolution with these new-age detectors can solve many unsolved puzzles of CR science.

As can be seen from the flux of CRs measured with different experiments in figure 1.4, CRs with energy $\sim 10^{17}$ eV have extremely low flux, around $1\,\text{particle km}^{-2}\text{sr}^{-1}\text{yr}^{-1}$ and a huge detector acceptance is needed for measurement. As CR particles interact in the atmosphere and produce secondaries, these secondaries in the air shower can be detected in ground based observatories. So the basic principle of ground based observatories are to use the atmosphere as a giant calorimeter. Several detection techniques are used to retrieve information about the primary cosmic rays from the observed showers of secondaries. For example,

Cherenkov radiation emitted by particles while traversing in atmosphere is measured by Air Cherenkov telescopes such as HESS and VERITAS detectors. These detectors work best on a clear night without moonlight. The efficiency of Cherenkov telescopes are improved by using water tanks as medium like in HAWC detector. Among other options of detecting CRs from ground based observatories are using scintillation detector, and detection of fluorescence light emitted by nitrogen molecule in the atmosphere, which were exited by the shower particles. Combination of detection techniques are also used in detector such as Pierre Auger Observatory where fluorescence detectors measure the induced air-shower and Cherenkov detector determines the footprint in earth. Recently Pierre Auger Observatory measurement confirmed the extragalactic origin of very high energy ($8 \times 10^{18}$ eV) CRs [49]. CR data available from different experiments over a wide energy range is shown in figure 1.4 including proton, electron and positron.

## 1.6 CALET on International Space Station

### 1.6.1 CALET Detector Components

CALET (CALorimetric Electron Telescope) is a Japan-led astrophysical mission in collaboration with Italy and USA for the International Space Station. CALET was docked to the Exposed Facility of the Japanese Experiment Module on August 2015 and the data collection started from October 2015 [44, 51]. The primary goal of CALET experiment is to measure the CR electron + positron spectrum directly for the first time in the TeV region (up to 20 TeV) starting from 1 GeV. Apart from this CALET can also measure CR nuclei ($1 \leq Z \leq 40$) up to several 100 TeV [52] and $\gamma$-rays up to 10 TeV [53, 54]. The data obtained in CALET on ISS uses NASA TDRS satellites to transfer the data to Whitesands ground station and then it is transferred to JAXA. In JAXA the CALET Ground Support Equipment (CALET-GSE) was prepared to operate CALET on-board ISS. The real-time data received in CALET-GSE is then transferred to Waseda CALET Operation Center (WCOC), where the detector performance is monitored and observation during the operation of CALET on ISS is carried out [55].

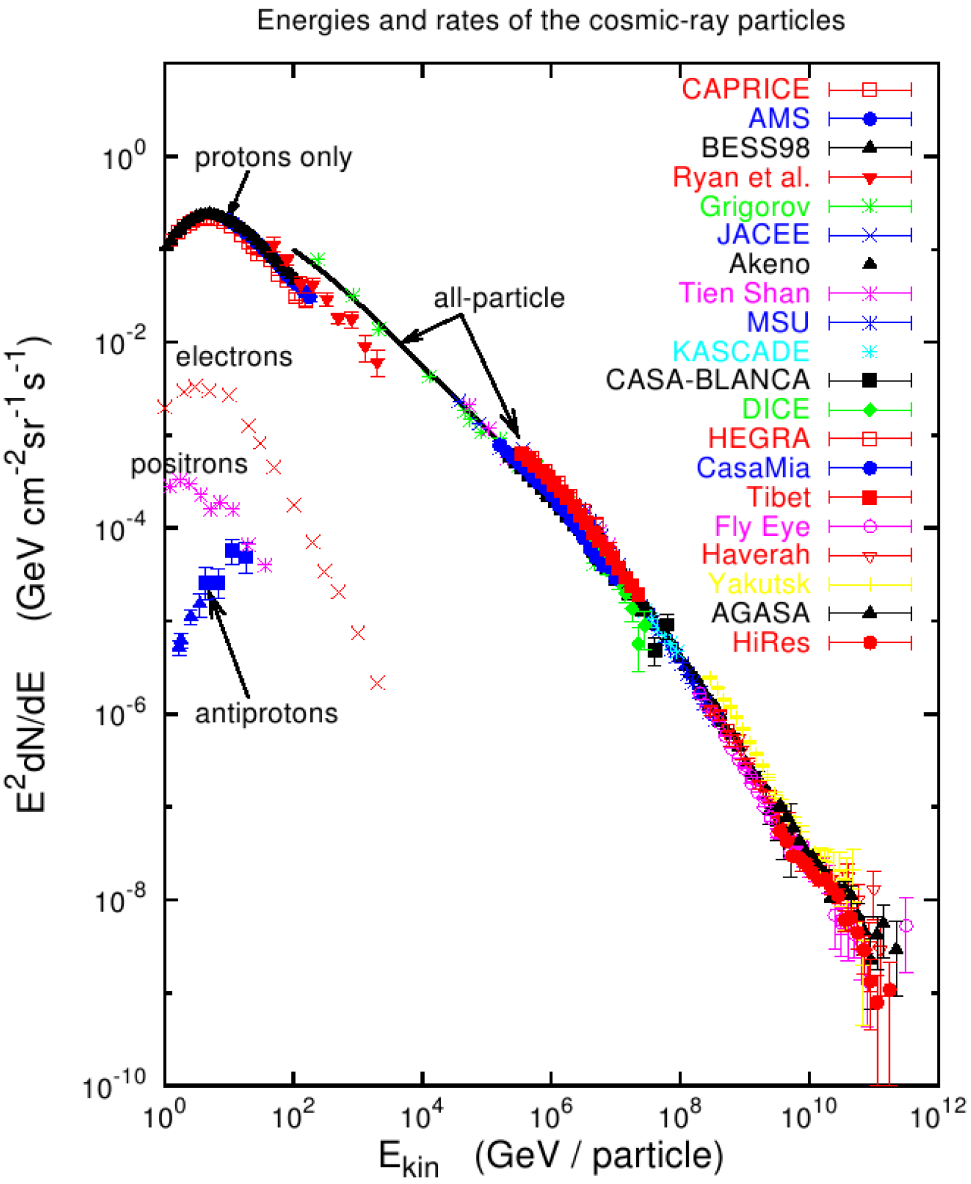


Figure 1.4: Major components of the CRs (including proton, electron, positron, antiproton) as observed at Earth measured by different detectors during different observation period over a wide energy range [50].

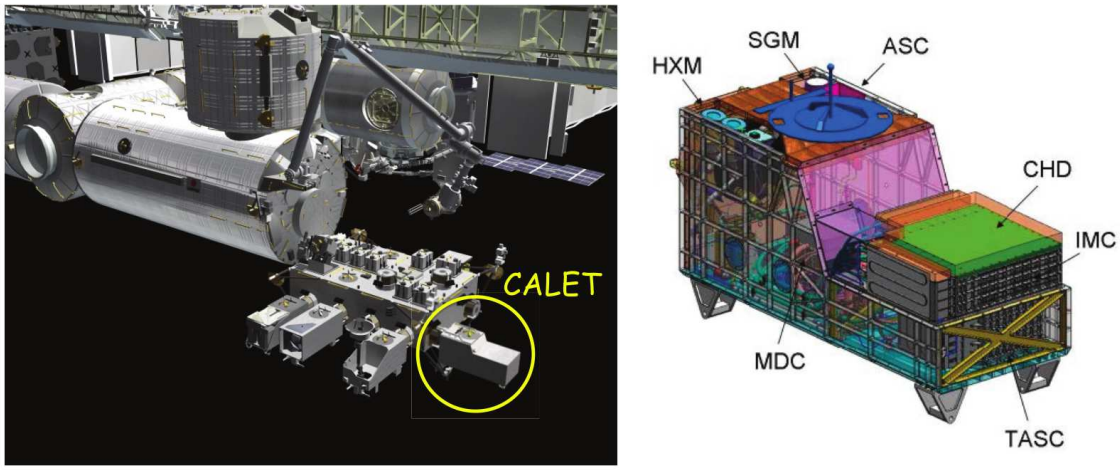


Figure 1.5: *Left*: CALET, robotically installed on the Japanese Experiment Module-Exposed Facility on the ISS at the port 9. *Right*: CALET detector and its components consisting of CHD, IMC, TASC and CGBM [44].

CALET is an all calorimetric instrument and with thick $30X_0$ (radiation length) calorimeter, it's fully capable of measuring the electron + positron spectrum in the TeV region. Even though CALET cannot distinguish the charge sign compared to the detectors based on magnetic spectrometers (such as AMS-02, PAMELA), due to its capability of discerning protons and electrons (high proton rejection ratio $1 : 10^5$), CALET will be used to search for fine structures in the CR electron spectrum.

CALET detector is a combination of 3 components-CHD (Charge Detector), IMC (Imaging Calorimeter) and TASC (Total Absorption Calorimeter). From the top of the detector, charge identification is done with CHD. It helps to identify the individual chemical elements in the CR flux. Then track reconstruction is done in pre-shower Imaging Calorimeter. Finally, the energy of the incident particle and discriminating hadronic shower from electromagnetic shower is done in TASC.

In CHD plastic scintillators are arranged in two perpendicular layers each containing 14 scintillators with dimensions 448 mm(L) $\times$ 32 mm(W) $\times$ 10 mm(H). Photomultiplier Tube (PMT) is used to collect the generated scintillation light and for read out. The resulting output is sent to FEC (Front End Circuit). The dynamic range of the FEC and the readout system is capable of providing particle

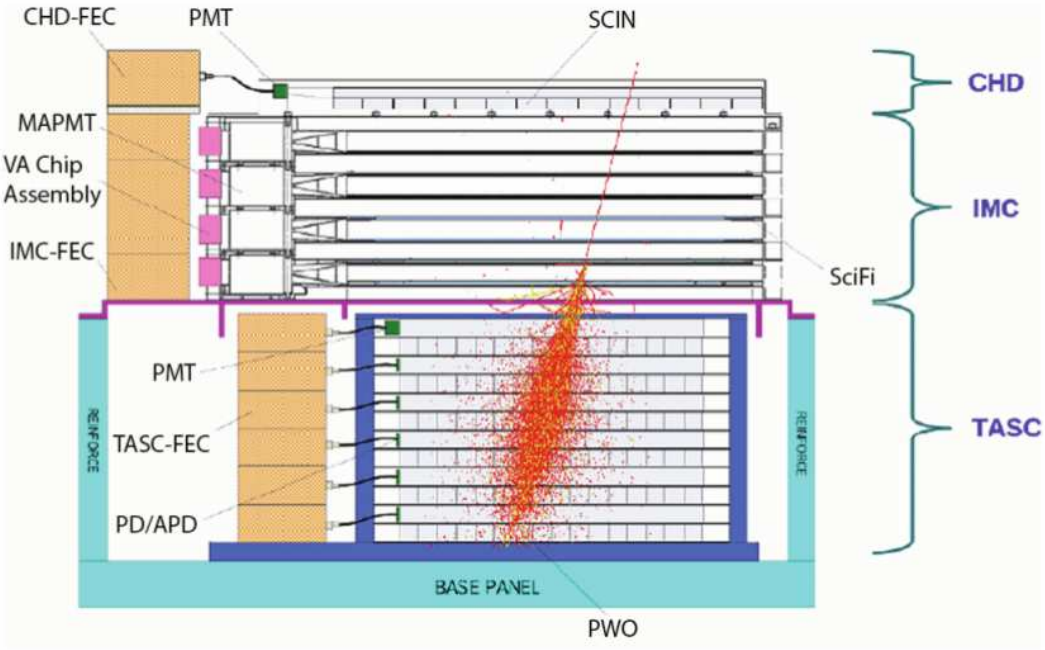


Figure 1.6: A schematic side view of the CALET CALorimeter (CALET-CAL). Simulated 1 TeV electron shower development inside the calorimeter is shown here. Image reference: [44].

identification from Z = 1 to 40. Whenever high energy electrons hit a block of material, due to Bremsstrahlung and pair-production runaway shower process will occur leading to rapid increase in the number of particles with the depth. This process will stop when the secondary particles are not energetic enough to create more particles and maximum number of shower particles will eventually die out due to ionization for electrons and Compton scattering for photons. The IMC is dedicated to image this shower profile which is designed with precision to determine the shower starting point and incident direction. The imaging pre-shower consists of 7 layers of tungsten plates each of them separated by 2 layers of 1mm square cross section scintillating fibers. The total thickness of this calorimeter is $3X_0$ which ensures proper development of electromagnetic shower in its initial stage is used for track reconstruction. The total absorption calorimeter (TASC) has a radiation length of $27X_0$ and it is composed of 12 layers where each layer consists of 16 lead tungsten logs (PWO or $PbWO_4$). Each logs has dimension $2.0 \times 1.9 \times 32.6$ (HWL) ($cm^3$) and with this design the TASC is able to image the shower development in 3D.

Apart from the main calorimeter CALET also has a $\gamma$-ray Burst Monitor (CGBM) and it uses two different kind of scintillators $LaBr_3(Ce)$, BGO [56]. The Hard X-ray Monitor (HXM) uses the Lanthanum compound and covers an energy range from 7 KeV to 1 MeV. The Soft $\gamma$-ray Monitor (SGM) is made of the Bismuth compound and covers the energy range from 20 KeV to 40 MeV.

Using all these detector components CALET is currently measuring nuclei, electron and $\gamma$-ray spectrum with unprecedented energy resolution and the implication of these high resolution measurements in CR science are discussed in the next section.

### 1.6.2 Science Goals of CALET Detector

*Search for Nearby Sources of High Energy Electrons:* High proton rejection ratio and fine energy resolution with measurement capability up to 20 TeV makes CALET a very sensitive probe for high energy electrons. High energy electrons lose energy mostly from inverse Compton radiation (ICR) and synchrotron radiation

while propagating and interacting with the galactic magnetic field and the ISRF. The energy loss processes are modeled as $\frac{dE}{dt} = -bE^2$ and the solution for this equation with the initial condition $E(0) = E_0$ is $E(t) = \frac{E_0}{1+b_0 E_0 t}$. From this it can be seen that electrons with energy $E_0$ cannot be older than $T_{\max} = \frac{1}{bE_0}$. It can be shown for electrons with energy 1 TeV, $T_{\max} \approx 10^5$ yr [57]. In the diffusive propagation the propagation length ($r_{\text{Diff}}$) is $r_{\text{Diff}} \propto \sqrt{T}$. So the propagation distance reduces and scales as $\frac{1}{\sqrt{E}}$ and it can be concluded that TeV electrons observed at the proximity of earth likely originated from nearby sources within 1 kpc distance. One of the most important objectives of CALET is to detect these nearby electron sources by the fine measurement of the TeV region of the spectrum. The number of these nearby electron sources are limited, like Vela [58], Monogem and few others [59]. Due to this the electron spectrum will carry some spectral features [60, 61], and at higher energies the arrival directions of electrons will appear anisotropic [62]. An example of simulated $e^+ + e^-$ spectrum according to the nearby SNR model described here in reference [57], measured with CALET assuming 5 years of data-taking is shown in figure 1.7a. This distinctive feature from Vela SNR in the TeV region of the spectrum depending on the time of the release of electrons from SNR, can be identified by CALET.

*Measurements of Primary and Secondary Nuclei:* Apart from measuring high energy electrons, CALET will also measure the nuclei spectrum up to few 100 TeV region. Due to this spectral features of the nuclei spectrum such as spectral hardening as reported by AMS-02 [63] or possibility of deviation from a pure power law spectrum could also be investigated. As mentioned before precise measurement of B/C ratio gives us information about diffusion coefficient index ($\delta$). Also measurement of ratio of nuclei is less prone to systematic errors rather than absolute flux measurements. Measuring B/C ratio up to TeV region with CALET will help to distinguish between Kolmogorov or Kraichnan type of diffusion models.

*Indirect Dark Matter Search:* Measuring the $e^+ + e^-$ flux and $\gamma$-ray flux up to TeV region with CALET will act as a great tool for the indirect DM detection searches. Even though AMS-02 can measure CR electron and positron spectrum separately up to TeV energy range [64], due to limitations of the magnetic spectrometer it cannot measure particles with energies beyond 1 TeV. CALET doesn't have a magnetic spectrometer so it cannot separate electrons and positrons, however, the

thick calorimeter ensures high precision measurement of $e^+ + e^-$ spectrum up to 20 TeV. Reported excess in the positron fraction over 10 GeV [8, 65, 66] is difficult to explain considering only the secondary production of positrons, however there are exceptions like this reference [67]. To explain the positron excess either DM annihilation or decay or astrophysical sources are proposed which produce electron-positron pairs. Fine energy resolution in the several 100 GeV to TeV region ensures that CALET has a great potential to search for distinctive features coming from DM decay or annihilation or a relatively smooth pulsar spectrum and this particular scenario is discussed in great detail and the results are presented in chapter 4. The smoking gun signal for DM annihilation or decay, the monochromatic $\gamma$-rays are also searched using CALET detector. Due to high energy resolution in the TeV region for the gamma-ray measurements an example of annihilation of neutralino DM at the galactic center producing monochromatic $\gamma$-ray signals [68] in the TeV region of the spectrum is shown in figure 1.7b. Since $\gamma$-ray and electron shower profile are almost same, to distinguish between them, $\gamma$-rays that interact after the first layer of IMC are taken into account, so that there won't be any signal in CHD and the top layer of IMC.

*$\gamma$-ray Search with CALET:* CALET will also compliment the dedicated $\gamma$-ray detector Fermi-LAT [6] with high statistic observation. Even though the Fermi-LAT detector area is larger than CALET, its calorimeter is comparatively thinner ($8\,X_0$) [6, 69] than CALET ($30\,X_0$), so the $\gamma$-ray showers at several 100 GeV region are fully contained inside the thick calorimeter. Recently, the search for X-ray and $\gamma$-ray counterparts of the gravitational wave event GW151226 [70] from the binary black hole mergers using CALET CGBM was reported here [54]. CALET right now is fully operational onboard and the new upcoming results will help to uncover many CR mysteries.

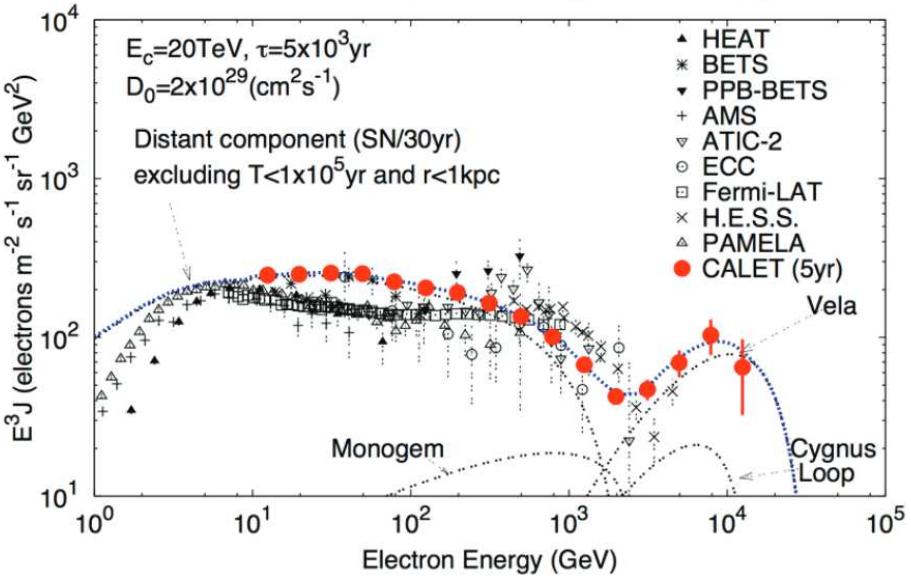


(a)

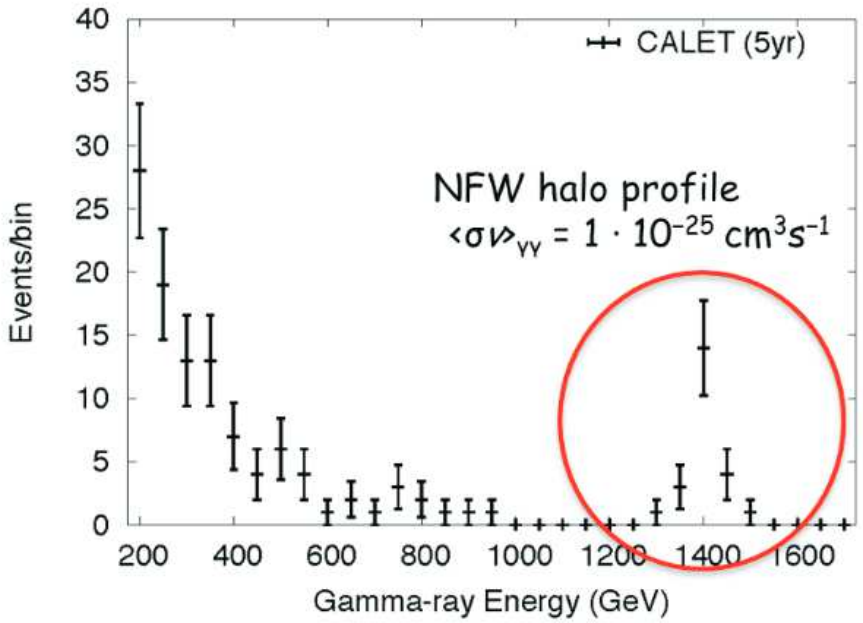


(b)

Figure 1.7: (a) Expected $e^+ + e^-$ spectrum measured with CALET assuming 5 years of observation for the nearby Vela SNR source model described by Kobyashi et.al. [57] is shown with red error-bars. (b) Assuming 5 years of CALET observation, a possible $\gamma$-ray line from the annihilation of 1.4 TeV DM at the galactic center is shown here. Image ref. [71]

# Chapter 2

# Dark Matter: Evidences and Detection Methods

## 2.1 Gravitational Effects of Dark Matter

Earliest evidences for DM came from the observance of velocity dispersion of individual galaxies within galaxy cluster. Fritz Zwicky noticed that the outer galaxies in Coma cluster were moving with far too speed that cannot be accounted by using simple Newtonian mechanics (virial theorem) and unseen large mass component is necessary [72]. Similar trends were found in Andromeda galaxy [73] where the rotation curve calculated from visible mass should drop off at higher distances ($v \propto \frac{1}{\sqrt{r}}$), instead it appeared flat. An example of flatness of rotation curve is shown in figure 2.1 for M33 galaxy [74]. Flatness of rotation curves for other spiral galaxies [75] also confirm the existence of large amount of unseen mass.

Apart from galaxy rotation curves, gravitational lensing is also another way to determine the mass of distant objects. According to Einstein's General Relativity theory presence of mass causes curvature in the spacetime and this in turn causes light to bend around the mass. So if light from distance source gets bend by a massive object (known as 'lens') between the source and observer (bending angle : $\theta = \frac{4GM}{c^2 R_{\rm scw}}$, where $R_{\rm scw}$ is the Schwarzschild radius of the 'lens', and $M$ denotes its mass), then the images of the source could reveal the information about the mass of

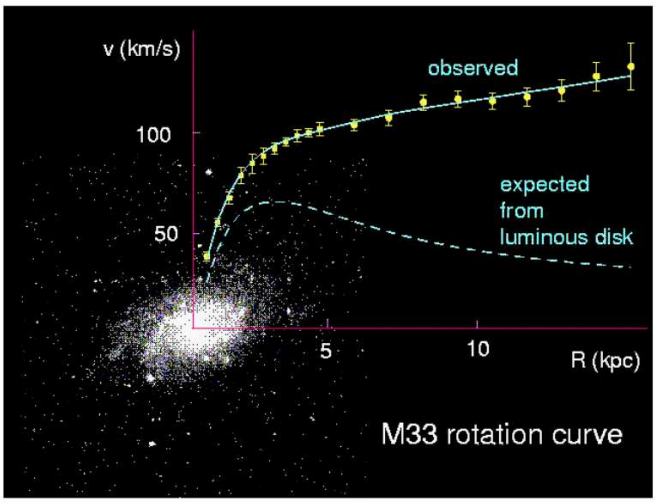


Figure 2.1: Rotation curve of nearby galaxy M33 superimposed on the optical image is shown here. If there's no matter apart from the luminous disk then the expected rotation curve follows an $\frac{1}{\sqrt{r}}$ distribution. Image reference: [76].

the object in between. Distant source clusters show far more gravitational lensing than what's expected from the visible mass distribution [77, 78]. This method also suggests presence of non luminous form of missing matter in the galaxies.

It is important here to note that non luminous matter collectively known as MACHOs (Massive Compact Halo Objects) like faint white dwarf stars, black holes and neutron stars cannot be taken as candidate for DM. Gravitational microlensing survey of the Magellanic cloud with EROS-2 experiment showed that MACHOs can account for only 8% of the halo mass [79]. Searching for red dwarfs (stars which are just massive enough to burn hydrogen) in galaxy also put stringent limit on low mass stars as candidate for DM [80]. Measurements from Planck or WMAP experiments show that MACHOs cannot be accounted as DM because the total estimated mass of the galaxies or clusters are much higher than measured by [81, 82]. These CMB anisotropy measurements along with supernova data allows us to estimate the matter density and DM density independently as shown in figure 2.4. Matter density parameter was independently derived using Solan Digital Sky Survey (SDSS) [83] by observing the clustering of galaxies and it show that baryons are responsible for only 20% of the matter in the universe ($\Omega_b h^2 \approx 0.022$) and the remaining is by DM ($\Omega_{\text{CDM}} h^2 \approx 0.11$). Here $H$ is Hubble Constant and $h = H/100\,\text{Km s}^{-1}\text{Mpc}^{-1} \approx 0.72$ [84] which was also estimated using the combined measurements.

Figure 2.2: Bullet Cluster, the image is constructed from X-ray distribution of gas (pink) and gravitational lensing of DM (blue). The image reveals weak interaction property of DM [85].

Probably the most promising evidence for DM is coming from the so called Bullet Cluster [85]. The Bullet Cluster is a merger of two clusters where weak lensing was used to map the DM distribution and X-ray was used to map the gas distribution. Apart from the fact that lensing map shows a lot of DM, the image reveals weak interacting property of DM. As shown in image 2.2 , the DM has passed through the gas clouds undisturbed while the gas interacted electromagnetically and and created a ballistic shape [1].

Apart from these evidences, the large scale structure of our universe also hint towards a substantial amount of DM. SDSS, a galaxy red-shift survey measuring red-shifts of $10^6$ galaxies, reveals information on the evolution of galaxy clustering [83]. This result when compared with large-scale N-body simulations, it shows the observed large scale structure of the luminous matter could only be formed in presence of DM [86, 87].

[1]Image Source: http://chandra.harvard.edu/photo/2006/1e0657/

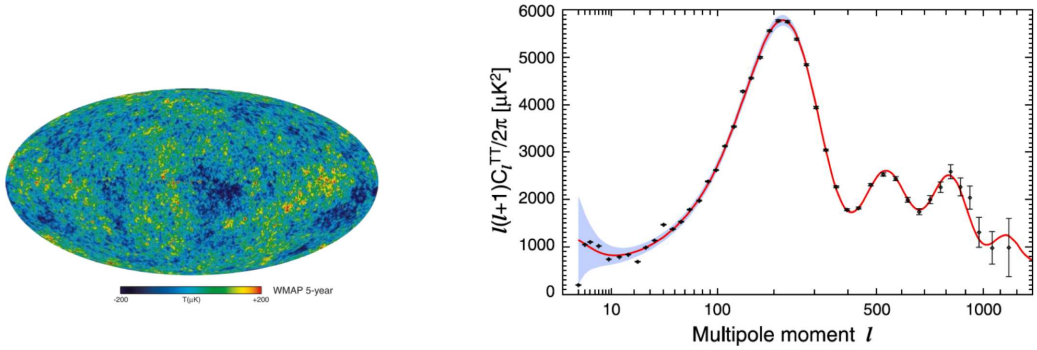


Figure 2.3: *Left*: CMB anisotropies as measured by WMAP for 9 years [81] is shown here. Change in colors represents the change in temperature from the uniform CMB temperature. *Right*: Λ-CDM model fit to the temperature of the angular power spectrum as measured by WMAP. The spectrum is plotted as a function of multipole moment ($l$) of the spectral functions which are used to quantify the angular size of the fluctuation observed by WMAP.

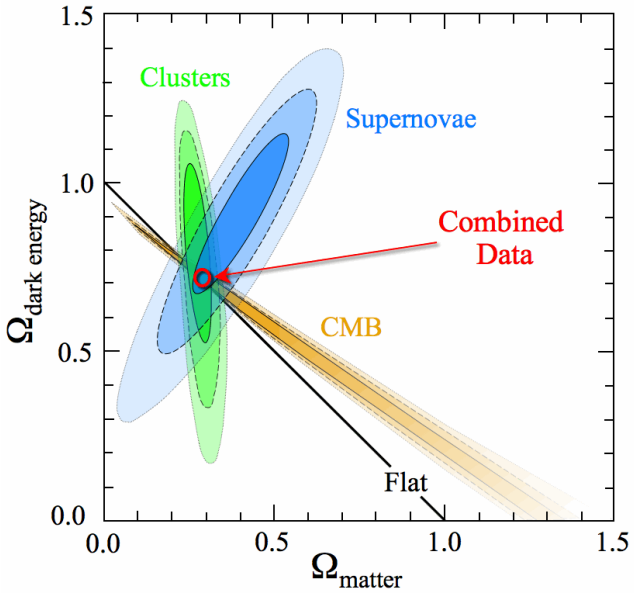


Figure 2.4: Supernovae, CMB and cluster abundance data are combined to set constraints to cosmological densities $\Omega_\lambda$, and $\Omega_m$. The flat Universe with $\Omega_\Lambda + \Omega_m = 1$ is shown with solid line [88].

## 2.2 Dark Matter Candidates

The evidences for the DM are usually coming from the gravitational effect of DM at cosmological scale. Bullet Cluster however supports the fact that DM are weakly interacting other than gravitational force, and the large scale structures hints that they are massive and non-relativistic in nature. Due to this, it is believed that DM constituents are massive neutral particles and weakly interacting. In the SM particle spectrum neutrinos are neutral and weakly interacting so they can be considered as candidate for DM but, cosmological simulations show that it's not possible to explain the clustering of galaxies with the low mass of SM neutrinos [89]. It's because in the early hot and dense universe, the neutrinos would be in thermal equilibrium with hot ordinary matter. Due to the low mass neutrinos are relativistic, even when the universe expands and cools down, they will be still relativistic at the time of structure formation. However, neutrinos are proposed as candidate for Hot Dark Matter (HDM), but it is shown that HDM alone cannot explain the large scale structure and the WMAP measurements and cold (non-relativistic) DM is necessary [90]. Also, the high DM density in the dwarf-spheroidal galaxies suggest that in these low mass galaxies neutrinos cannot be DM [91].

Models beyond SM are proposed to explain the DM density in our universe. Among them the most widely studied DM particles are designated as as Weakly Interacting Massive Particles (WIMPs), where the natural "freeze-out" mechanism [92–95] can explain the relic density calculated from the observed CMB anisotropy by PLANCK or WMAP, assuming DM played the leading role in structure formation at the early universe. As the universe expands and cools, the freeze-out temperature is usually defined as when the rate of expansion of space is more than the interaction rate, the particles decouples from the thermal bath. The evolution of the particles with time in the early universe is governed by the Boltzmann equation

$$\frac{dn_\chi}{dt} + 3Hn_\chi = \langle\sigma v\rangle \left(n_{\chi_{\rm eq}} - n_\chi\right) , \tag{2.1}$$

where, $n_{\chi_{\rm eq}}$ is the number density of particle species $\chi$ at equilibrium, $\langle\sigma v\rangle$ is the velocity averaged cross section for interaction processes like $\chi\chi \rightarrow$ other partilces. The density of the particles in thermal equilibrium is suppressed by the Boltzmann factor ($e^{-\frac{m}{T}}$). So if a particle species remained in thermal equilibrium still present,

it's abundance would be absolutely negligible, but if the particles freeze-out at a temperature where $\frac{m}{T}$ is not much greater than 1, then those particles will have significant abundance today. The Boltzmann equation 2.1 can be solved numerically [92], and to a good approximation for particles with WIMP mass range the relic density is

$$\Omega_\chi h^2 = 0.1 \frac{3 \times 10^{-26} \mathrm{cm}^3 \mathrm{s}^{-1}}{\langle \sigma v \rangle} \,. \tag{2.2}$$

So as it can be seen from this equation larger the interaction cross section, higher is the interaction rate and longer the particle species remain in equilibrium in the early universe, which in turn, lowers the abundance of them today. Also, considering weak interactions,and mass in the electro-weak scale (i.e. mass lies in the range from 100 GeV to few TeV), s wave ( due to low energy scattering approximation, orbital angular momentum (L) of the interacting particles are 0) annihilation cross section is $\approx 3 \times 10^{-26}\,\mathrm{cm}^3\mathrm{s}^{-1}$ [92, 96], so naturally it explains the DM abundance today. This is also known as 'WIMP-miracle'. Example of WIMP DM can arise in many theoretical particle physics models and one of the most extensively used models is Super-symmetric model, where the lightest neutralino is the most natural choice for DM candidate in a minimal super-symmetric model (MSSM) [94]. Other exotic theories such as theory of universal extra dimension also predicts DM, known as Lightest Kaluza-Klein Particle (LKP) by imposing discrete symmetries in the theory which ensures that neutral lightest particle remains stable and can act as a DM candidate [97]. In a simplest UED (Universal Extra Dimensions) model, with one extra dimension (total 5 dimensions) of size $R \sim 1\,\mathrm{TeV}^{-1}$ it is assumed that all the standard model particles exist. The theory has a conserved parity known as KK parity and the lightest KK particle is stable and acts as a DM candidate. The annihilation cross section of LKP DM into fermions is directly proportional to the fourth power of hypercharge of the final state fermions and thus the right handed leptons ($e_R$, $\mu_R$, $\tau_R$ with hypercharge $= -2$) are produced dominantly and the branching fraction of around $20 - 23\%$ for each generation is assumed [98]. An example of TeV scale LKP DM annihilation signature on CR electron spectrum is shown later in section 3.6.

A few of the WIMP theory related models which also predict DM candidates are - 1) *WIMPzillas*- these are weakly interacting, super-heavy particles formed out of thermal equilibrium [99], 2) WIMPless DM- where WIMP miracle

is proposed to happen through a hidden sector [100], 3) eXciting DM (XDM)-where WIMPS are in excited states and often used to explain the Sommerfeld enhancement [101]. Apart from WIMP and WIMP related candidates there are other particle physics models also proposed to explain DM and, sterile neutrinos is one such candidates. 1) Sterile neutrinos which were initially proposed to explain the neutrino mass [102], can be viable candidates for DM [103]. 2) Axions are one of the important non-WIMP candidates which were initially proposed to solve the strong CP (charge-parity) problem in particle physics [104]. Axions are light and stable on cosmological time scale and due to the possibility of non-thermal production (thermal production is also possible and in such case the the density is given by eq. 2.2), it can have low kinetic energy and can act as CDM [105, 106].

## 2.3 Dark Matter Detection Methods

### 2.3.1 Collider Search and Direct Detection of Dark Matter

The experiments to find evidences of DM particles beyond the gravitational effects are divided in three categories, collider search, direct detection and indirect detection. As shown in figure 2.6, the schematic diagram to highlight the detection strategies in different searches. If DM particles are weakly interacting and mass is close to the weak scale then in the Large Hadron Collider (LHC) the signature is expected to be in the missing energy in proton-proton collisions with interaction of type $pp \rightarrow \chi\bar{\chi} + x$, where $x$ can be hadronic jet, photon or $Z$, $W$ bosons coming from the decay of leptons [107]. Since the evidences of DM are searched in the missing energies of the jets, collider searches provide limits on the cross-section for candidate particles with mass ranging from few GeVs to few hundreds of GeV [108].

Another way to look for DM particles is to identify nuclear recoils produced by the collisions of the candidate particles for DM and a target nuclei in the detector and this method of search is known as direct detection. It was reported here [109] that if WIMP has a mass in the range 10–1000 GeV, then elastic scattering would produce nuclear recoils in the range 1–100 KeV. A possible way to reduce background in direct detection method is to search for annual modulation which

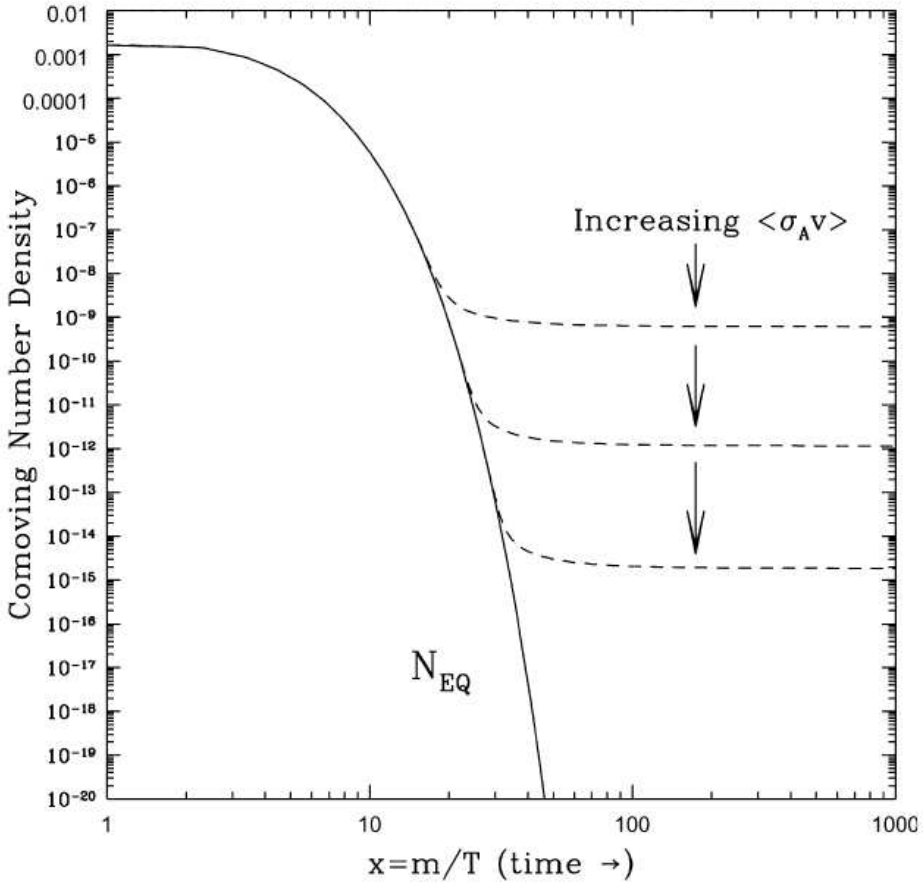


Figure 2.5: In the early universe if the particles follow the equilibrium distribution, present density would be negligible as shown with the straight line. However, 'freeze-out' mechanism ensures that the particles can have significant abundance today based on the annihilation cross-section of the particle. Larger cross-section implies longer time in the thermal equilibrium and consequently lower relic abundances [92].

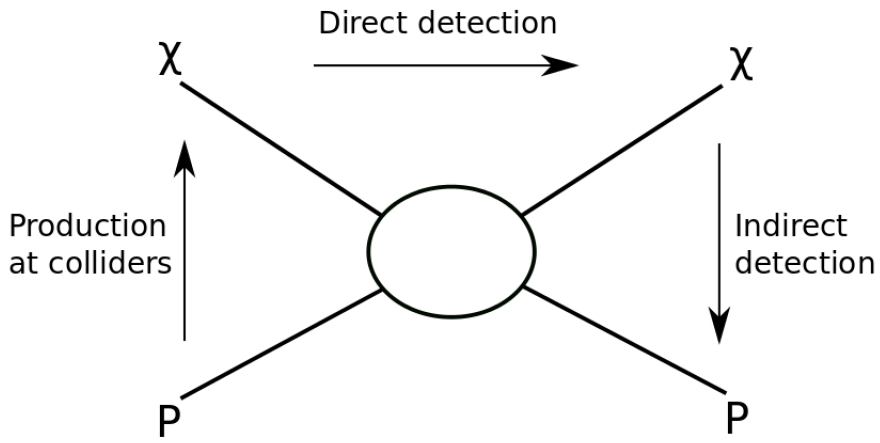


Figure 2.6: Schematic diagram to show the relation among various DM detection methods. The arrows indicate the direction of interaction, where $\chi$ is the DM candidate and $P$ is a SM particle [112].

arises because of the motion of the earth around the sun and the relative speed of the DM particles in the milky-way halo reaches maximum in June and minimum in December [110]. Such annual modulation was claimed to be seen with DAMA experiment [111], which however was not confirmed by any other direct detection experiments. In the upcoming future the detector sensitivity will get better and search for nuclear recoil signals will further constrain the parameter space for DM mass and weak cross-section.

Apart from collider search and direct search, another way of searching DM is to look for the stable messengers ($e^{\pm}, \gamma, \nu, \frac{\bar{p}}{p}$) in the CRs which may come from DM annihilation or decay. Indirect detection of DM and its relation with CR physics is discussed in detail in the next section as it's an important topic of this thesis work.

### 2.3.2 Indirect Dark Matter Detection

The indirect detection of DM is based on the factor that after freeze-out DM can still decay or undergo pair annihilation reactions. These WIMPs posses weak-scale annihilation cross section and the DM particles can produce equal amount

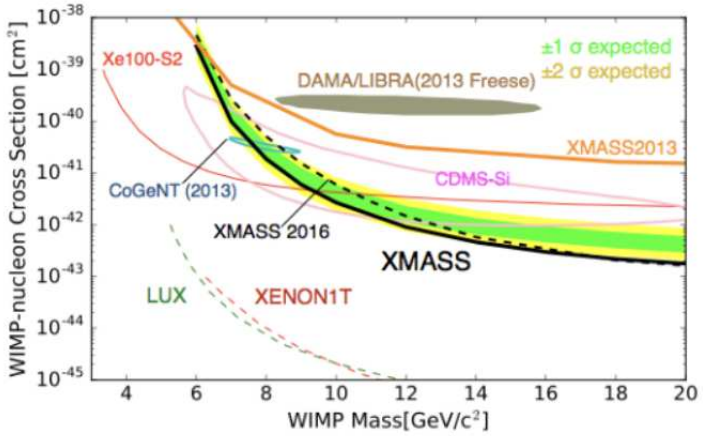


Figure 2.7: Limits on WIMP masses and spin-independent nuclear cross sections are shown here for XMASS detector. The black line shows the 90% CL exclusion from the XMASS modulation analysis and results from other experiments are shown here for a comparison.

of electron-positron pairs. The DM particles that suppose to constitute our own galaxy along with baryonic matter, using indirect detection method, it's possible to detect the primary or secondary annihilation products. Indirect detection aims at detecting the annihilation or decay signatures in the fluxes of CRs including charged particles (electrons, positrons, antiprotons, antideuterium), photons ($\gamma$-rays, X-rays, synchrotron radiation) and neutrinos. Specially the anti-particles which are much less abundant than particles are one of the main focus regions for search of DM.

Now to search for CR signals coming from DM annihilation or decay first the injected particle per volume and time at production should be known, which can be propagated in the galaxy using known CR propagation model to calculate the expected flux at the proximity of earth. The flux at production from the DM decay or annihilation depends broadly on the particle physics model of the DM and the DM distribution in the galaxy. The flux from the annihilation products of DM inside milky-way DM halo at a position $\vec{r}$ from the galactic center per unit time

and volume can be written as

$$Q_{\rm a}(\vec{r},\,E) = \underbrace{\rho^2(\vec{r})}_{\text{Astrophys.}}\;\underbrace{\sum_f \frac{\langle\sigma v\rangle_f\; dN_f}{2M_{\rm DM}^2\, dE}}_{\text{Particle Phys.}}\,, \tag{2.3}$$

and corresponding flux from the decay of DM is given by

$$Q_{\rm d}(\vec{r},\,E) = \underbrace{\rho(\vec{r})}_{\text{Astrophys.}}\;\underbrace{\sum_f \frac{\Gamma_f\, dN_f}{M_{\rm DM}\, dE}}_{\text{Particle Phys.}}\,, \tag{2.4}$$

where $M_{\rm DM}$, $\Gamma_f$ are the mass and decay rate of DM respectively and $\rho$ is density of DM particles in the milky way halo. $\frac{dN_f}{dE}$ is the energy spectrum of positrons produced in the annihilation and decay of DM for the channel $f$ [113, 114].

This branching ratios to different to different final states depends on the particle physics model. Usually the final states can be any SM particles if it's allowed by energetics. If the final states are not stable, they can quickly decay or hadronize to produce stable SM particles and this is known as prompt emission. The energy spectrum for each channel $\frac{dN_f}{dE}$ is either calculated using the event generator PYTHIA [115], or directly used from the publicly available repository PPPC4 [116], where the energy spectra at production for the charged particles ($e^{\pm}$, $\bar{p}$, $\bar{d}$), $\gamma$ and $\nu$ are computed using high-statistics simulation and presented in a table format. These are described in more detail when the flux of the charged particles from the DM decay or annihilation are calculated later on. If the DM decay or annihilation produces $\gamma\gamma$, $h\gamma$, $Z\gamma$, then a monochromatic photon line can be like a smoking gun signature, as the standard astrophysical processes does not produce this kind of signature [117, 118]. An example of prompt spectra for photons and electrons are shown in figure 2.10 for the selected channels ($e^{\pm}$, $\mu^{\pm}$, $\tau^{\pm}$, $W^{\pm}, t\bar{t}$, $b\bar{b}$) from an annihilating DM of mass ($m_\chi$) 500 GeV, obtained from PPPC4. In the right panel of figure 2.10, the prompt electron spectrum from the annihilating DM is the hardest compared to the other lepton channels like $\mu^+\,\mu^-$ and $\tau^+\,\tau^-$. The $e^+\,e^-$ spectrum however is not line like due to the Final State Radiation (FSR) which is included in PPPC4 for all annihilation products. The hadronic and gauge boson channels produce softest spectra as they are more massive and consequently relatively unstable compared to the leptons. This spectral shape is transmitted in the propagated spectrum of the decay or annihilation products from DM.

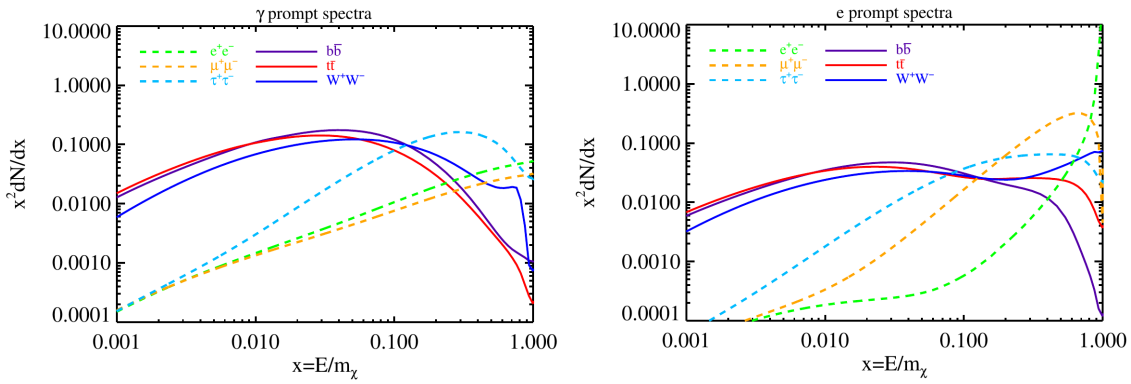


Figure 2.8: The differential energy spectrum per annihilation is shown as function of DM mass ($x = E/m_\chi$). Prompt spectra for $\gamma$-ray (left) and electron (right) from the annihilation of 500 GeV DM to the stable SM particles are shown with dotted and straight lines [116].

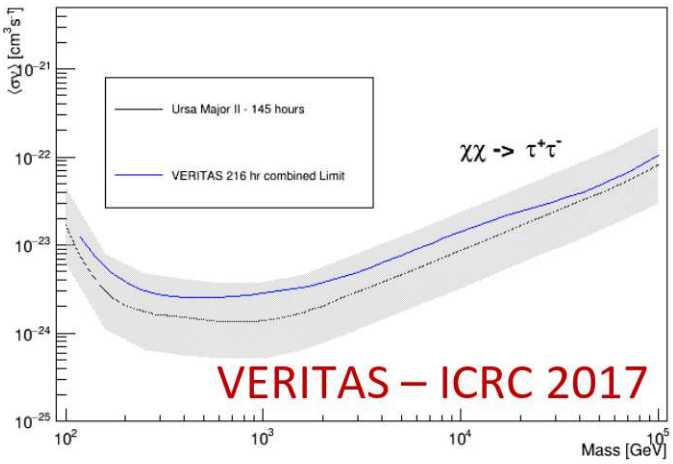


Figure 2.9: Preliminary results from VERITAS on limits on the DM self-annihilation cross-section by observing dSph Ursa Major over 145 hours is shown here. Current limits as presented in ICRC 2017 over 216 hours of observation exceeds the old limit at all masses for tau lepton. The grey band represents $1\sigma$ uncertainty in the $J$ factor. Image reference [119].

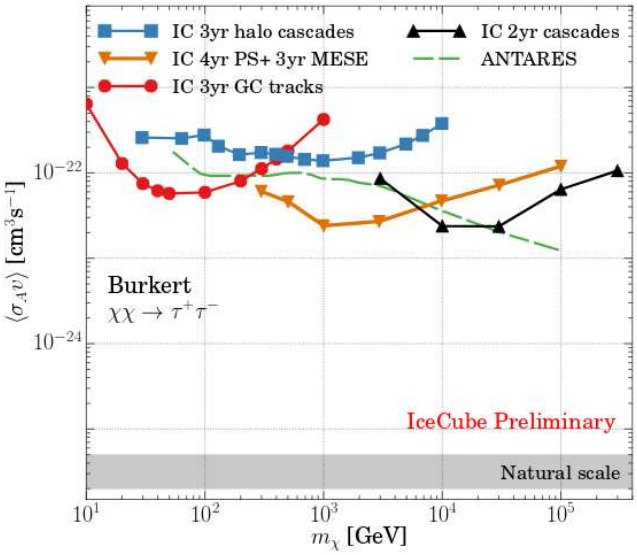


Figure 2.10: Upper limits of DM annihilation cross-section for the tau lepton channel as measured by IceCube, assuming Burkert profile is shown here. Image Reference [120]

From eq. 2.3 and 2.4, the flux in the annihilation scenario is proportional to square of the DM density but in the decay case it's linearly proportional with DM density. For searching signals of the annihilation or decay from DM it's necessary to reduce the background coming from the ordinary astrophysical processes. That's why even though the galactic center (GC) is DM dominated, because of the unknown and complex background [121, 122] and uncertainty in the DM density profile [123], the indirect search for DM usually concentrates away from the galactic center. For the DM halo profile or the DM distribution in the galactic halo there are several possibilities, like Einasto profile [124, 125], Isothermal profile [126], Burkert profile [127], Moore profile [128]. In figure 2.11 an example of variation of DM density for NFW, Einasto and Burkert profile are shown as a function of distance from the center of galaxy. Strong DM density at the galactic center can be achieved using either Einasto or NFW profile. Since in this thesis work mostly $e^+ + e^-$ spectrum in the energy region 10 GeV-few TeV is considered and as mentioned in section 1.6.2 due to high energy loss rate only nearby CR sources are relevant, the halo profile does not really affect calculations. For our study NFW profile is used as a benchmark profile which is motivated by the study of large-scale N-body

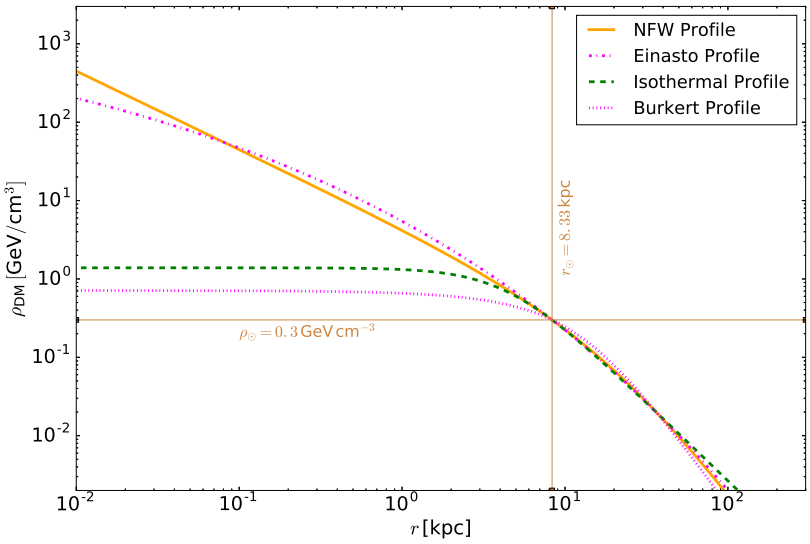


Figure 2.11: DM density variation with distance from the center of galaxy in NFW (orange line), Einasto (magenta dash-dot line), Isothermal (green dotted line) and Burkert profile are shown here. Normalization density is taken as $\rho_0 = 0.3$ GeV cm$^{-3}$ at a position $r_\odot = 8.33\,\text{kpc}$ [116].

simulation [129]. The NFW profile is defined as

$$\rho = \frac{\delta_c \rho_c}{(r/r_s)\,(1 + r/r_s)^2} \tag{2.5}$$

$\delta_c$ is defined as

$$\delta_c = \frac{200}{3} \frac{c_v^3}{\ln(1 + c_v) - (c_v/(1 + c_v))} \ , \tag{2.6}$$

where $c_v$ is defined as the ratio of virial radius ($r_v$) and scale radius ($r_s$), and we assume $c_v = 10$ [130]. $\rho_c$ is determined from the mass of the halo as

$$\rho_c = \frac{\frac{4}{3}\pi r_v^3}{M_v} \ , \tag{2.7}$$

where $r_v$, $M_v$ are taken as 200 kpc and $1.5 \times 10^{12} \text{M}_\odot$ [131]. Once the flux at production is known the it is propagated in galaxy and resulting flux is obtained at the proximity of Earth by solving the diffusion equation (eq. 1.16).

# Chapter 3

# Calculation of Cosmic Ray Propagation

## 3.1 Analytical Method to Solve Transport Equation

Models describing CR propagation in galaxy such as Leaky-Box Model and diffusion model are described in detail in section 1.3. For solving the propagation equation and calculating CR density at earth two approaches are widely used namely Analytical approach and Numerical approach. Apart from these, semi-analytical approach was also used to solve CR transport equation [132]. In the analytic and semi-analytic approach it's assumed that the galactic disc is much thinner than the galactic halo as shown in figure 3.1. CR sources and interactions are all confined in the thin disc and the diffusion occurs throughout the disc and the halo with same strength. To solve the CR diffusion equation analytically, widely used Green's function technique is described here in short. For example considering negligible energy loss for CR protons in the ISM the diffusion equation (eq. 1.16) can be reduced to

$$\frac{\partial n}{\partial t} = \nabla \left( D \nabla n \right) + Q \,. \tag{3.1}$$

For a delta-function source term $Q(\vec{r},\, E,\, t) = \delta(\vec{r} - \vec{r'})\,\delta(t - t')$, the Green function is given by

$$G(\vec{r},\, \vec{r'},\, t,\, t') = \frac{1}{8\,(\pi D(t-t'))^{\frac{3}{2}}} \exp\left[\frac{-(\vec{r'} - \vec{r})^2}{4D(t-t')}\right] . \tag{3.2}$$

Using this Green function for a linear equation with delta function source, the general solution of eq. 3.1 can be obtained [133] as

$$n(\vec{r},\, E,\, t) = \int_{-\infty}^{\infty} d\vec{r'} \int_{-\infty}^{t} dt' G(\vec{r},\, \vec{r'},\, t,\, t')\, Q(\vec{r'},\, E,\, t)\,. \tag{3.3}$$

Using variable separation $Q(\vec{r'},\, E,\, t) = q(\vec{r'})\, q(E)\, q(t)$, where $q(E)$ denotes the source spectrum and for a power-law source spectrum it can be approximated as $q(E) = C\, E^{-\gamma}$. Considering a burst-like emission of particles at time $t_0$, the temporal source term can be written as $q(t') = \delta(t' - t_0)$. Using this, eq. 3.3 can be written as

$$n(\vec{r},\, E,\, t) = \frac{q(E)}{8\,(\pi D(t-t_0))^{\frac{3}{2}}} \int_{-\infty}^{\infty} d\vec{r'} \exp\left[\frac{-(\vec{r'} - \vec{r})^2}{4D(t-t_0)}\right] q(\vec{r'})\,. \tag{3.4}$$

Setting the Earth as origin of the coordinate system ($\vec{r} = 0$) and assuming a point-source located at a distance $\vec{r_s}$ from Earth, the spatial source term can be written as $q(\vec{r'}) = \delta(\vec{r'} - \vec{r_s})$. Using this, proton density at Earth can be written as

$$n(E,\, t) = \frac{q(E)}{8\,(\pi D(t-t_0))^{\frac{3}{2}}} \exp\left[\frac{-r_s^2}{4D(t-t_0)}\right] , \tag{3.5}$$

This is the usually adopted solution considering nearby single point-source contribution. Assuming a power-law behavior of spatial diffusion coefficient (eq. 1.17) as $D(E) \propto E^{\delta}$, then for high-energy protons eq. 3.5 can be approximated as $n \propto E^{-\gamma + \frac{3}{2}\delta}$. However, for electrons and positrons the energy loss term is important and following eq. 1.16, the diffusion equation takes the form

$$\frac{\partial n}{\partial t} = \nabla(D \nabla n) + \frac{\partial}{\partial p}(\dot{p} n) + Q\ . \tag{3.6}$$

The energy loss term for electrons is modeled as $\frac{dE}{dt} = -bE^2$. The energy loss coefficient ($b$) is defined as

$$b = \frac{4\sigma c}{3(mc^2)^2} \left(\frac{B^2}{8\pi} + w_{\rm ph}\right) , \tag{3.7}$$

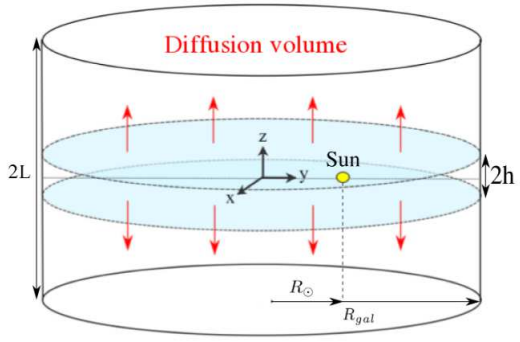


Figure 3.1: A schematic diagram of the 2D cylindrical diffusion of CRs in the galaxy. The sources are confined in the thin galactic disc ($h \approx 0.1$ kpc) whereas the diffusion zone or the halo is extended up to 6–10 kpc. Position of the sun with respect to the galactic center is shown (not scaled) [134].

where $E$ is the electron energy, $\sigma$ is the Thomson scattering cross section, $B$ is the galactic magnetic field strength and $w_{\rm ph}$ is the energy density of interstellar photons [57]. So the energy loss consists of synchrotron and IC losses and these two terms are described in detail later. For a non-linear equation of this type the analytical approach is still possible under the condition that propagation distance is smaller than the galactic halo thickness. The detail solution of this equation was described in detail in this reference [57]. For a point source located in the galactic plane, the electron density can be written as (see eq. 3.5 for comparison) $n \sim \frac{CE^{-\gamma}}{(4\pi D_1)^{\frac{3}{2}}}(1-btE)^{\gamma-2}\exp\left[\frac{-r_s^2}{4D_1}\right]$, where $D_1$ is given by $D_1 = \frac{D_0[1-(1-bEt)^{1-\delta}]}{b(1-\delta)\,E^{1-\delta}}$ [57] and $D_0$ is the normalization for the diffusion coefficient as defined in eq. 1.17.

In the semi-analytical approach the propagation equation can be written starting from the continuity equation. The CR particle density variation with time is given by

$$\partial_t n + \partial_\mu J^\mu = Q\,, \tag{3.8}$$

where $\vec{J} = (\vec{V_c} - D\nabla)n$ and $J_E = (b - D_E\partial_E)n$. Comparing with the diffusion equation 1.16 it can be seen that it's similar, with total energy loss rate is same as before and it is given by $b(E) = \frac{dE}{dt}$. However, a new term describing the diffusion in momentum space appears here with the coefficient of diffusion is given by $D_E$. As the interaction and sources are confined in the thin disc, a term $2h\delta(z)$ is added

to the source term and terms relating to the interaction and energy loss processes and eq. 3.8 in the steady state can be written as

$$-\nabla(D\nabla n) + V_c\frac{\partial}{\partial z}n + 2h\delta(z)\,\partial_E\left(-D_E\partial_E n + b(E)n\right) = 2h\delta(z)\,Q\,. \tag{3.9}$$

Assuming cylindrical symmetry eq 3.9 can be solved by means of Bessel expansion method.

One important point here is that the energy loss rate $b(E)$, includes the total energy loss in the thin disc ($b_{\rm disc}$) and the halo ($b_{\rm halo}$). The energy loss processes in the disc includes ionization, adiabatic loss, bremsstrahlung, coulomb energy loss and for the halo it includes synchrotron radiation and inverse Compton scattering and these are dominant for electrons compared to massive nuclei (ex. Proton). This also leads to conclusion that high energy electrons ($\sim$ TeV) are produced by young and nearby sources [57,61,135]. For the nuclei energy loss processes dominates only in the disc, so $b_{\rm halo}$ is not present and the equation can be solved for the nuclei and the results are shown here [136] elaborately up to $Z = 30$. However, this approach is not valid for electrons or positrons where energy losses in the galactic halo due to synchrotron radiation and inverse Compton scattering are not negligible (from eq 3.9, $b(E)$ now approximates as $b(E) = 2h\delta(z)b_{\rm disc} + b(E)_{\rm halo}$) [137]. Presence of $b(E)_{\rm halo}$ term prevents eq 3.9 to be solved analytically. This is the first limitation of analytical approach for correctly calculating the flux of electrons or positrons at earth. However, considering only high energy positrons or electrons (energy above few GeV) it is shown that the dominant propagation processes are only diffusion and energy loss in the halo [138]. So in this scenario, neglecting reacceleration, convection and energy loss processes in disc, eq 3.9 is simplified as

$$-\nabla(D\nabla n) + \partial_E(b(E)n) = Q\,. \tag{3.10}$$

This equation can be solved analytically by using the pseudo-time method [139]. The flux at the earth can then be computed for secondary electrons as well as electrons produced from DM annihilation, decay or astrophysical objects like pulsar [140].

Apart from the fact that analytical method can solve the propagation equation for electrons and positrons only with some approximations, it has also several drawbacks. The gas distribution in the ISM in analytical method is assumed

uniform, whereas in reality it is a function of the galactic coordinates and inhomogeneous. Several software packages are developed to solve the propagation equation. USINE is a package used for solving the CR equation analytically, which is still not publicly available [136]. On the other hand, GALPROP and DRAGON are publicly available packages for solving the propagation equation numerically [141, 142]. The cosmic ray source distribution in numerical approach are more realistic and taken in such a way to reproduce the diffuse $\gamma$-ray measurements (eq 1.15). The ISRF, which has a strong influence on electron energy losses are modeled taking into account of the stellar population, dust distributions and scattering of starlight in numerical propagation codes which is not the case in analytical approach. Because of the complicated gas and source distribution in galaxy and realistic energy loss processes for all the charge particles are taken into account in numerical codes, to solve the propagation equation in 2-D or 3-D approach is much more time consuming compared to the fast calculations in analytical approach. For the study of nuclei, electron, positron and $\gamma$-ray propagation in galaxy, numerical code GALPROP for the solution of the transport equation is used in this thesis and this is described in detail in the next sections of this chapter.

## 3.2 GALPROP: Numerical Calculation of Cosmic Ray Propagation

### 3.2.1 Numerical Solution of Diffusion Equation

The numerical solution for diffusion equation in a time-dependent situation can be computed using finite difference method. To show an example of how it's done let us consider time dependent one dimensional diffusion equation.

$$\frac{\partial u}{\partial t} = C\frac{\partial^2 u}{\partial^2 x} \tag{3.11}$$

Now in FTCS scheme time derivative term is approximated with forward difference and space derivatives are approximated with second order central differences. This gives

$$\frac{{u_i}^{n+1} - {u_i}^n}{\triangle t} = \frac{{u_{i-1}}^n - 2{u_i}^n + {u_{i+1}}^n}{\triangle x^2} \ , \tag{3.12}$$

where $x_i = i\triangle x (i = 0, 1, 2, 3, ....N)$ and $t_n = n\triangle t (n = 0, 1, 2, ...)$. To distinguish between space and time coordinates, index $n$ is used for time coordinate and $i$ is used for space coordinates. Here if eq. 3.11 represents the heat flow on a long thin rod then $N$ denotes the number of the points on the length of the rod. At any typical node the finite difference equation can be written as

$$u_i{}^{n+1} = u_i{}^n + r(u_{i-1}{}^n - 2u_i{}^n + u_{i+1}{}^n) \ , \tag{3.13}$$

where $r$ can be written as $\frac{C\triangle t}{\triangle x^2}$. Since the previous equation has only one unknown for any $i$ and $n$ it's called as an explicit scheme. The stability and the convergence depends upon the step length in space ($\triangle x$) and time ($\triangle t$).

Another way of solving diffusion equation is known as Crank-Nicolson method which used not only the explicit scheme discussed above but implicit scheme also [143]. For example if the forward difference approximation in time derivative of eq. 3.11 is replaced with backward difference and keeping the central difference scheme for space derivative term the same, then the equation becomes

$$\frac{u_i{}^n - u_i{}^{n-1}}{\triangle t} = C\frac{u_{i-1}{}^n - 2u_i{}^n + u_{i+1}{}^n}{\triangle x^2} \ . \tag{3.14}$$

This equation can be re-written as

$$\frac{u_i{}^{n+1} - u_i{}^n}{\triangle t} = C\frac{u_{i-1}^{n+1} - 2u_i{}^{n+1} + u_{i+1}^{n+1}}{\triangle x^2} \ . \tag{3.15}$$

This equation can be simplified as

$$\begin{aligned} u_i{}^{n+1} &= u_i{}^n + r(u_{i-1}{}^{n+1} - 2u_i{}^{n+1} + u_{i+1}{}^{n+1}) \\ u_i{}^n &= (1 + 2u_i{}^{n+1}) - ru_{i-1}{}^{n+1} - ru_{i+1}^{n+1} \end{aligned} \tag{3.16}$$

Since there are 3 unknown terms (with indices $n + 1$), this is known as implicit scheme. Crank-Nicolson method is obtained by taking average of implicit and explicit schemes.

$$\frac{u_i{}^{n+1} - u_i{}^n}{\triangle t} = \frac{C}{2}\left[\frac{u_{i-1}^{n+1} - 2u_i{}^{n+1} + u_{i+1}{}^{n+1}}{\triangle x^2} + \frac{u_{i-1}^n - 2u_i{}^n + u_{i+1}{}^n}{\triangle x^2}\right] \ , \tag{3.17}$$

which can be further reduced as

$$u_i{}^{n+1}[1 + r] - \frac{r}{2}u_{i-1}{}^{n+1} - \frac{r}{2}u_{i+1}^{n+1} = \frac{r}{2}u_{i-1}{}^n + [1 - r]u_i{}^n + \frac{r}{2}u_{i+1}{}^n \ , \tag{3.18}$$

where $i = 1, 2, 3, ....N$, and $n = 0, 1, 2, 3, ....$ Here also three unknown terms are present, so Crank-Nicholson method is an implicit scheme and to solve this tri-diagonal matrix method is used.

### 3.2.2 Crank-Nicolson Method for Solving Cosmic Ray Diffusion

Crank-Nicolson method is developed as a improvement over the explicit method due to better convergence, stability of the solution. In Crank-Nicolson method the CR propagation equation (eq. 1.16) can be finite-differenced in a form

$$\frac{\partial n_i}{\partial t} = \frac{n_i^{t+\Delta t} - n_i^t}{\Delta t} = \frac{\alpha_1\, n_{i-1}^{t+\Delta t} - \alpha_2\, n_i^{t+\Delta t} + \alpha_3\, n_{i+1}^{t+\Delta t}}{2\Delta t} + \frac{\alpha_1\, n_{i-1}^{t} - \alpha_2\, n_i^{t} + \alpha_3\, n_{i+1}^{t}}{2\Delta t}\ , \tag{3.19}$$

where $i$ represents the spatial position. Simplifying it gives

$$n_i^{t+\Delta t} = n_i^t + \frac{\alpha_1}{2} n_{i-1}^{t+\Delta t} - \frac{\alpha_2}{2} n_i^{t+\Delta t} + \frac{\alpha_3}{2} n_{i+1}^{t+\Delta t} + \frac{\alpha_1}{2} n_{i-1}^{t} - \frac{\alpha_2}{2} n_i^{t} + \frac{\alpha_3}{2} n_{i+1}^{t}\,. \tag{3.20}$$

Crank-Nicolson method is stable for all $\alpha$ and $\Delta t$. As the quantities are known at time $t$, rearranging the terms will give us

$$-\frac{\alpha_1}{2} n_{i-1}^{t+\Delta t} + \left(1 + \frac{\alpha_2}{2}\right) n_i^{t+\Delta t} - \frac{\alpha_3}{2} n_{i+1}^{t+\Delta t} = \frac{\alpha_1}{2} n_{i-1}^{t} + \left(1 - \frac{\alpha_2}{2}\right) n_i^{t} + \frac{\alpha_3}{2} n_{i+1}^{t}\ , \tag{3.21}$$

where the R.H.S. of the equation is known and it's solved for $n_i^{t+\Delta t}$. The above equations are shown for one-dimensional case. As mentioned before just like eq.3.18, above eq. 3.21 can also be solved using tri-diagonal matrix method. However for CR propagation where either 2 or 3 spatial dimension and 1 time dimension is used, tri-diagonal method is no more valid. In this case Alternating Direction Implicit (ADI) method is used and in this case the implicit solution is applied to each dimension and this method is valid for small timesteps [144].

### 3.2.3 Cosmic Ray Propagation using GALPROP

For solving the CR diffusion equation (1.16) and study of CR propagation in galaxy, in this thesis work GALPROP [1] numerical code is used on several occasions. The source code is written in c++ along with few FORTRAN 77 routines. Apart from the main GALPROP package, it uses several publicly available other packages such as CCfits, HEALPIX, cfitsio, GSL and CLHEP. Also there's a precompiled version of

[1] https://galprop.stanford.edu/

GALPROP available in webrun facility [141], where GALPROP calculations are done in a dedicated supercomputer in Stanford University.

GALPROP solves the propagation equation either in 2D $(r, Z)$ or 3D $(X, Y, Z)$ where $r = \sqrt{X^2 + Y^2}$. The solar system lies in the galactic plane at a distance of 8.5 Kpc away from the center of galaxy. The boundary of the diffusion zone in height and radius and also the size of the spatial grid are all user defined variables. Apart from the spatial grid there is a momentum grid. Minimum and maximum energy of particles per nucleon in MeV defines the range of energy of calculation of CR fluxes. The energy grid points are logarithmic in nature. For example the energy of grid point $i$ is calculated as $E_i = E_{min}(E_{factor})^i$, where $(E_{min})$ is the minimum energy and $E_{factor}$ is the ratio of energy in successive grid points. For calculation of CR fluxes each grid point is assumed to represent the cosmic ray particles inside a bin with lower boundary $E_{i(low)} = E_{min}(E_{factor})^{i-0.5}$ and upper boundary $E_{i(high)} = E_{min}(E_{factor})^{i+0.5}$. For diffusion, diffusive reacceleration and convection all the parameters as described in eq 1.17, eq 1.18 and eq 1.19 can be controlled as input parameters in the propagation calculation.

The GALPROP source distribution is modeled after the SNR distribution derived from the EGRET $\gamma$-ray observation [145]. It is assumed in GALPROP that source distribution in GALPROP for all the primaries are same. The spatial distribution of the source function in GALPROP [33] is defined as

$$q = q_0 \left(\frac{d}{d_0}\right)^{\eta} \exp\left(-\zeta \frac{d - d_0}{d_0} - \frac{|Z|}{0.2}\right) \tag{3.22}$$

where $q_0$ is the normalization constant, and $\eta$, $\zeta$ are taken as 0.5 and 1 respectively in the default version which are input parameters and can be changed by user. $d$ in 3D propagation is defined as $\sqrt{X^2 + Y^2}$ and $d_0$ is the distance of the Sun from the galactic center, which is by default set to 8.5 kpc. The second term on the R.H.S. of this equation highlights the fact that CR sources are mostly confined within a galactic disc of height 200 parsec. The distribution of atomic hydrogen in GALPROP is taken as

$$n_{\mathsf{HI}}(R, Z) = n_{\mathsf{HI}}(R) e^{-(\ln 2)(Z/Z_0)^2}, \tag{3.23}$$

where $n_{\mathsf{HI}}(R)$ is taken from this reference [146] and $Z_0(R)$ is defined in such a way that the HI layer outside the solar system increase exponentially. This is in contrast

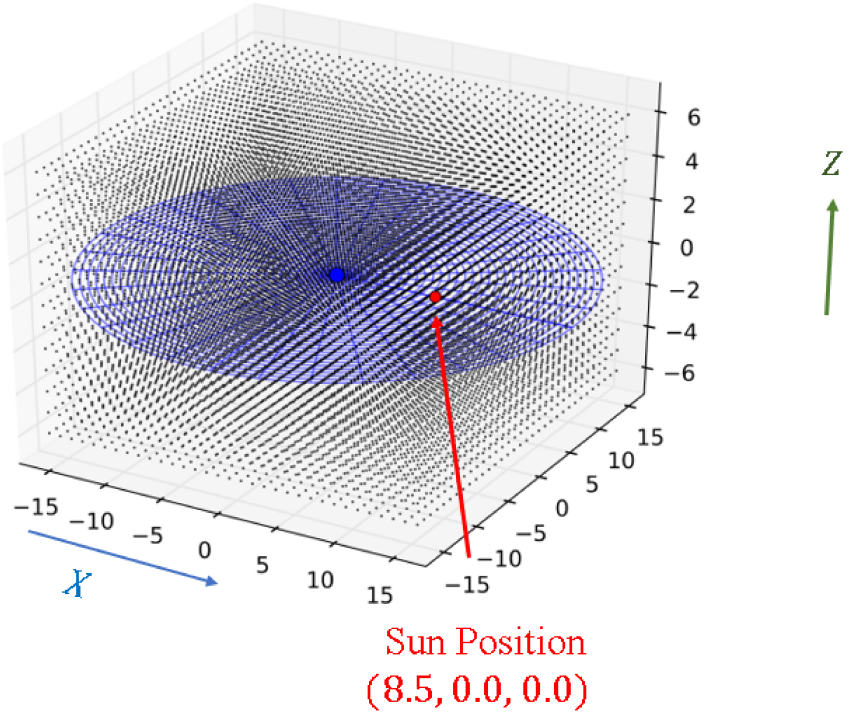


Figure 3.2: Schematic diagram of spatial grid system with 3-D coordinate system in GALPROP is shown here. The galactic plane is the shaded blue region and the solar system is 8.5 kpc away from the galactic center. Here a spatial binning of 1 kpc in $X$, $Y$, $Z$ directions are shown, however the bin size depends upon the problem and they are adjustable parameter in GALPROP.

with the simplistic uniform density assumed in analytical models of propagation. The production of secondary electrons and positrons which are the decay products of charged pions coming from the *pp* collision are extensively tested with different models and parametrization [147].

The numerical solution of diffusion equation is done using Crank-Nicolson method which is described in section 3.2.2. From eq. 3.21, the coefficients $\alpha_1$, $\alpha_2$, $\alpha_3$ needs to be known for different processes involved in CR propagation (diffusion, reacceleration, energy loss etc.), for solving the propagation equation. In general GALPROP solves the cosmic-ray time-dependent propagation equation. The boundary conditions that is imposed at each iteration for 3-D case are

$$n(\pm X_{\rm max}, Y, Z, p) = n(X, \pm Y_{\rm max}, Z, p) = n(X, Y, \pm Z_{\rm max}, p) = 0. \qquad (3.24)$$

This is done only for the spatial grid and no boundary conditions are imposed in $p$. The spatial grid intervals are typically $\Delta X = \Delta Y = 0.5$ kpc and $\Delta Z = 0.1$ kpc. The solution of the equation proceeds starting from a large timestep and repeated 20 times typically until a steady state is reached. In each repetition the timestep is reduced successively and start timestep, end timestep, timestep factor and repeat are all input parameters in GALPROP. The small timestep solutions which is controlled by the timestep-factor parameter in GALPROP are more reliable as it ensures a proper convergence for electron and positron propagation in galaxy [144]. The end-timestep which is dominated by energy-loss processes, for lighter elements like electron this value is usually kept at 10 years whereas for nuclei where energy loss processes are not significant end timestep value can be set to $10^4$ years for reliable calculation [144]. Thus electron propagation takes more time for a given computer resource compared to protons. Reducing the timestep-factor parameter increases the propagation calculation time considerably and requires reasonably high computer resources. GALPROP propagation starts with the calculation of propagation equation for the heaviest nuclei with $Z = 28$ ($^{64}$Ni) and the atomic number is an input parameter. In GALPROP depending on the value of $Z$, the calculation starts from heavier nuclei and then the secondary source function is calculated for a given gas distribution and reaction cross-section and then the secondaries are propagated. This top-down approach is done to properly include the spallation products for nuclei and finally the calculation ends with electron, positron and antiproton calculation. For this propagation calculation momentum is taken as

the kinematic variable which makes the reacceleration calculation easier [33]. There are options to include processes like K-capture of electrons or knock on electrons and even tertiary antiproton propagation.

Not only the charged nuclei, GALPROP can also calculate the $\gamma$-ray flux. For the calculation of $\gamma$-rays, interstellar gas data (for decay of pions and bremmstrahlung) and the Interstellar Radiation Field (ISRF) model are used [148] and the results are shown here in ref. [25] and compared with the experimental measurements from EGRET and COMPTEL. $\gamma$-rays from a particular region of sky can be calculated by specifying the longitude and latitudes as the input parameters and this is described later in the thesis for the calculation of secondary $\gamma$-rays from the DM decay products.

## 3.3 Energy Loss of Cosmic Ray Electrons in GALPROP

These energy loss terms constitute the momentum loss term $(\frac{\partial}{\partial p}\dot{p}\psi)$ in GALPROP. This term is calculated in GALPROP beforehand for the fixed values of the energy grid, and stored in an array for use during calculation of the CR propagation. This causes the precision of the energy loss calculation for electrons to be dependent on the energy grid bin size. This is explained in Figure 3.3 by a simplified example. Considering a power law spectrum $E^{-3}$ and calculating the average energy of the particles given by $\bar{E} = (\int_{E_n}^{E_{n+1}} f(E)EdE)/(\int_{E_n}^{E_{n+1}} f(E)dE)$ inside one energy bin, it is shown that for fine energy binning this average energy is very close to the energy grid point, while it is significantly shifted to lower energy for the coarse binning. Therefore the energy loss of electrons is more accurately taken into account for a fine energy binning calculation. The effect of this binning dependence is shown in Figure 3.4, where reducing the bin size i.e. reducing the energy factor for successive energy bins make the electron spectrum softer. In figure 3.5 it is also demonstrated that the effect is not prominent for hadrons as their radiative energy loss rate is much lower compared to electrons.

For solving CR propagation equation using Crank-Nicolson method, the

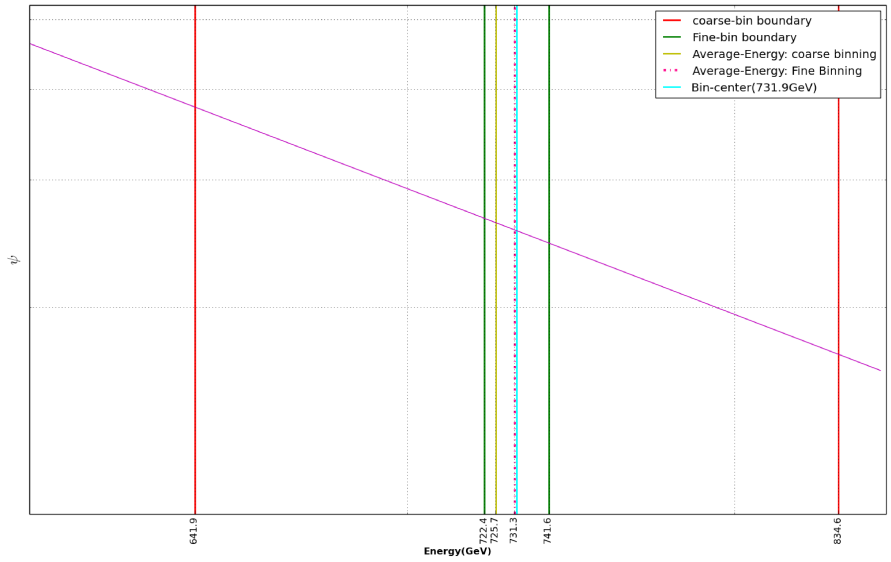


Figure 3.3: The magenta line represents a power law spectrum $\psi E^{-3}$ inside the energy bin with bin center at 731.9GeV given by the Cyan vertical line. The bin boundaries are described by the red lines for coarse binning($E_{factor}$ : 1.3) and the green lines for finer energy binning($E_{factor}$ : 1.03). The average energy of the particles inside this bin is 725.7GeV for coarse binning(yellow line) and 731.3GeV for finer binning. The deviation of the energy is much smaller for fine binning(0.6)GeV, than (6.20)GeV for coarse binning.

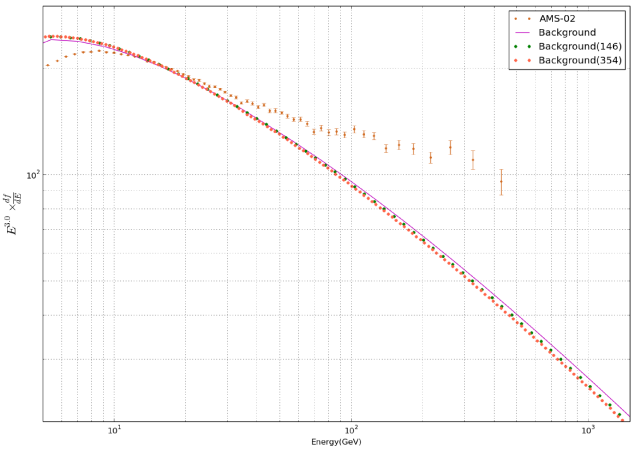


Figure 3.4: Electron Spectrum calculated at different energy bins - 354 bins (red dots), 146 bins (green dots), 54 bins (magenta line) shows a gradual change in the slope of the spectrum with energy bins. As the energy bin size decreases the spectrum becomes softer.

coefficients $\alpha_1$, $\alpha_2$, $\alpha_3$ in eq. 3.21 are necessary to be known. In 2D propagation these coefficients for diffusion, and energy loss processes are listed in the table 3.1.

To address the energy-bin problem in GALPROP the Crank-Nicolson coefficients for energy loss processes are modified. As shown in figure 3.3, for a simple power law spectrum the particle densities at $i$th and $i+1$th energy bins are wrongly calculated due to mismatch of average energy inside the bin from the the bin-center. So considering particle density as a function, several interpolation pro-

| *Process* | *Coordinates* | $\alpha_1/\Delta t$ | $\alpha_2/\Delta t$ | $\alpha_3/\Delta t$ |
|---|---|---|---|---|
| Diffusion | $R$ | $D_{xx}\frac{2R_i-\Delta R}{2R_i(\Delta R)^2}$ | $D_{xx}\frac{2R_i}{2R_i(\Delta R)^2}$ | $D_{xx}\frac{2R_i-\Delta R}{2R_i(\Delta R)^2}$ |
| | z | $\frac{D_{xx}}{\Delta z^2}$ | $\frac{2D_{xx}}{\Delta z^2}$ | $\frac{D_{xx}}{\Delta z^2}$ |
| Energy Loss | $p$ | 0 | $\frac{\dot{p_i}}{p_{i+1}-p_i}$ | $\frac{\dot{p_{i+1}}}{p_{i+1}-p_i}$ |

Table 3.1: Crank-Nicolson coefficients (eq. 3.21) for diffusion and energy loss processes used in GALPROP are shown here. The coefficients are shown for 2D propagation with $R$ and $z$ as spatial coordinates.

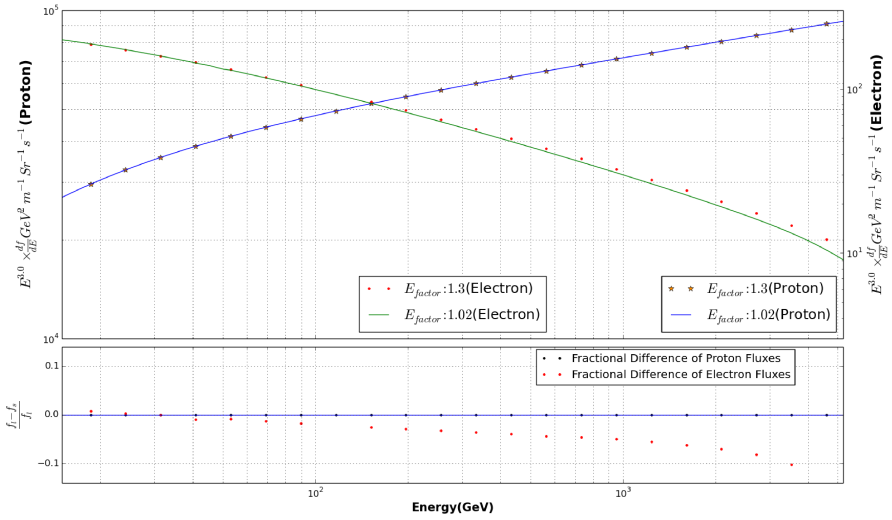


Figure 3.5: The figure above shows proton and electron spectrum plotted at two different energy bins(for proton orange stars-$E_{factor}$ : 1.3, blue line-$E_{factor}$ : 1.02 and red dots-$E_{factor}$ : 1.3, green line $E_{factor}$ : 1.02) calculated with GALPROP. The lower panel shows the fractional difference of fluxes calculated with these two energy binning for proton(black dots) and electron(red dots).

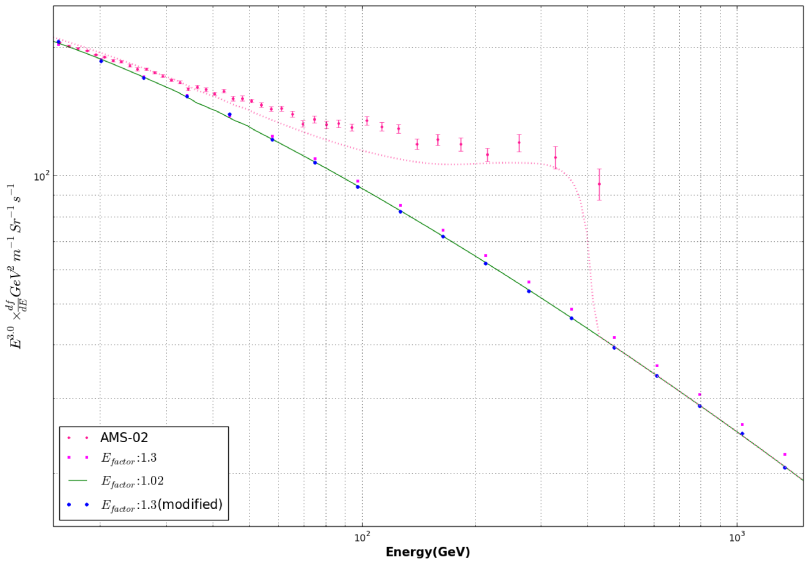


Figure 3.6: Electron spectrum propagated using coarse bin calculation with the modified GALPROP (blue dots) matches well with the fine bin calculation (green line). Electron flux calculated using coarse bin without modification is shown with the red dots.

cedures were tested and the best results were found when the interpolation takes the form $P = \left(\frac{\psi_i - \psi_{i+1}}{\psi_i}\right)^2$. In the GALPROP source code the routine for calculating these coefficients (propel.cc) were modified in the energy loss calculation section and using the interpolation function, $\alpha_2$ and $\alpha_3$ are redefined as

$$\begin{aligned} \alpha_{2i} &= \frac{\dot{p_i}}{p_i - p_{i+1}} \times (1.0 - P) \\ \alpha_{3i} &= \frac{\dot{p}_{i+1}}{p_i - p_{i+1}} \times P\,. \end{aligned} \tag{3.25}$$

The effect of this modification is shown in figure 3.6, where electron spectrum calculated using coarse bin in the modified GALPROP matches well with the fine bin calculation. Later on the DM annihilation spectrum at production is also propagated using this modified version and the results are discussed in section 3.6.

## 3.4 Calculation of Dark Matter Signatures with GALPROP

The process of calculating fluxes from possible DM decay or annihilation is described in section 2.3.2. Depending on different DM theories the decay or annihilation products are different (ex: leptons: such as $e^{\pm}$, hadrons: such as $q\bar{q}$, gauge bosons: such as $W^{\pm}$, or even higgs boson). From eq. 2.4 and 2.3 for a certain DM density profile we need to know $\frac{dN}{dE}$ which is the spectrum of outgoing particles produced per annihilation or decay. DM annihilation or decay spectra is believed to be very different from spectra obtained from astrophysical sources such as pulsars or SNRs which usually have a featureless power law spectra. In case of annihilation and decay the maximum energy of the outgoing particles can be mass of DM and half of the mass of DM respectively. To obtain the DM annihilation flux at production, at first publicly available table PPPC4DMID is used. It uses the Monte Carlo simulation programs PYTHIA [115] and HERWIG [149] to include parton showers and hadronization and finally the fluxes of $e^{\pm}$, $\bar{p}$, $\bar{d}$, $\gamma$, $\nu_{e,\mu,\tau}$ at production are calculated. The tables, which are available online [2], provides the spectra $\frac{dN}{d\log_{10}x}$ at production per one annihilation as a function of DM mass (with mass of DM ranging from 5 GeV to 100 TeV). Here $x$ is the ratio of kinetic energy of the outgoing final state stable particles and mass of DM.

Before using the flux of DM annihilation at production from PPPC4 in GALPROP, it is checked with another high energy calculation package, micrOMEGAs [150]. micrOMEGAs, which contains both C and FORTRAN routines, is a package to calculate the CDM properties. Even though it was developed to calculate relic density of DM in different models, it can also calculate the direct and indirect detection rate [151]. After obtaining $\frac{dN}{dE}$ for the desired outgoing channels from PPPC4, the GALPROP code is modified so that it can take into account the DM flux per unit time and volume by assuming NFW profile for DM density. The same propagation parameters used for the background CR propagation are taken for the electron/positron propagation coming from DM annihilation.

[2] http://www.marcocirelli.net/PPPC4DMID.html

## 3.5 Choice of Propagation Parameters for Dark Matter Propagation

For self-consistent propagation calculation using numerical simulation, it is necessary to have same propagation parameters for all CR species, including propagation of decay or annihilation products from DM. Before determining CR propagation parameters by comparison with current measurements, first the effect few important input parameters in GALPROP on CR electron spectrum are shown in figure 3.7. The effect of changing energy-bin size in GALPROP, on electron spectrum are already discussed. Among other parameters, the effect of changing the diffusion zone height on CR electron spectrum is shown in figure 3.7a and the lower panel shows the difference of electron fluxes for different halo height and the effect is prominent only at the low energy region. Effect of diffusion coefficient and alfven speed on electron spectrum propagated in GALPROP are sown in figure 3.7b, and it is confirmed that reacceleration process is only dominant in the energy region below 10 GeV for the electron flux. Choosing a set of parameters for calculating propagation of all the charged CR species are described below.

In GALPROP using the propagation parameters obtained from best-fit to Proton and B/C ratio measurements by AMS-02 (figure 3.9), produces a very hard electron spectrum as shown in figure 3.10. Even without any extra source contribution to the CR electrons (which is needed for explanation of the positron excess), this spectrum is too hard to match the AMS-02 observation at all. To investigate this problem, the CR source distribution model in milky-way galaxy is studied in detail. Looking from the Earth it's possible to see the spiral arm structure of external galaxies but living in the disc plane of Milky Way makes it difficult to ascertain the properties or distances of the spiral arms in Milky Way. However, measurements from *Spitzer Space Telescope* [152] has provided deeper understanding of star formation, interstellar dust and large scale structure of Milky way. In a follow up study [153] using GLIMPSE (Galactic Legacy Infrared Midplane Survey Extraordinaire), it is shown that Milky Way is organized into four spiral arms, with two primary arms being the Scutum-Centaurus and Perseus arm and the two secondary arms being Sagittarius and Norma arms (outer arms). This is shown in figure 3.8, where the schematic sketch of Milky Way is presented from

face-on perspective. The galactic coordinates are also shown to locate the position of spiral arms and the Sun lying between two spiral arms in a relatively under-dense region. Evidences of OB stars [154] and star-forming regions [155] tracing spiral arms, suggests that CR sources such as supernova and pulsars do the same. Therefore it's reasonable to study the effect of some fraction or all the galactic CR sources lying in the spiral arm of Milky Way. If the CR sources lie in the spiral arms of Milky Way, then they will experience more energy losses due to increase in propagation distance and the spectrum at Earth will be softer for leptons [142].

The GALPROP source distribution is chosen in such a way that it can reproduce the EGRET $\gamma$-ray observation [145]. The source function in GALPROP as a function of spatial variables [33] is given by eq. 3.22 and the constants are adopted to fit the gamma-ray gradient. This source distribution is assumed to be same for all CR primaries. However, this is not a true representation of the the spiral arm structure of our galaxy [142, 153, 156]. The source distribution is modified and is modeled as 4 concentric rings with a Gaussian density profile. The half-width of the Gaussian density profile is ($\sigma$) and it represents the ring thickness. To study the effect of the ring thickness in the CR spectrum, $\sigma$ is varied in the range 0.5–0.7 kpc. This new spatial distribution of the source function is given by

$$q_N = q \times \left( \sum_{i=1}^{4} e^{-\frac{(d-r_i)}{2\sigma^2}} \right) \ , \tag{3.26}$$

here $r_i$ are the distances of the ring profile centers from the center of the galaxy. Compared to the original GALPROP source distribution, this spiral arm structure causes the primary cosmic rays to propagate on average a larger distance and experience more energy loss, which makes the CR electron spectra softer. A comparison between the new source distribution and the GALPROP source distribution is shown in the left panel of figure 3.10. The effect of the thickness of the spiral arms, which is represented by the $\sigma$ parameter in eq. (3.26), on the electron spectrum is shown in the right panel of figure 3.10. In the GALPROP simulation including spiral arms, the ring centers are assumed to be separated by 4 kpc [157] and the first ring is taken at a distance 2.5 kpc away from the galactic center. Assuming the solar system at a distance 8.5 kpc from the galactic center and Perseus arm $\approx$ 2 kpc away from Earth [158], the third ring is located at 10.5 kpc away from the galactic center and the final ring is located at 14.5 kpc.

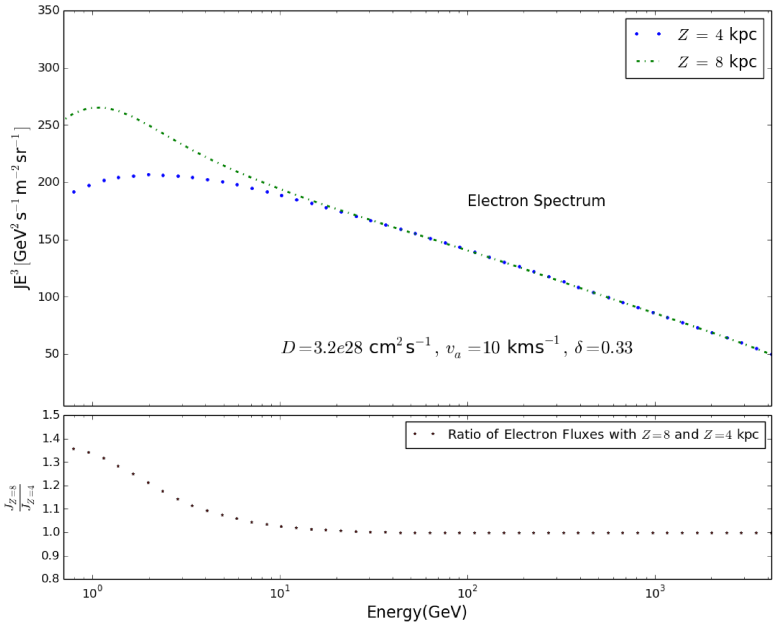


(a)

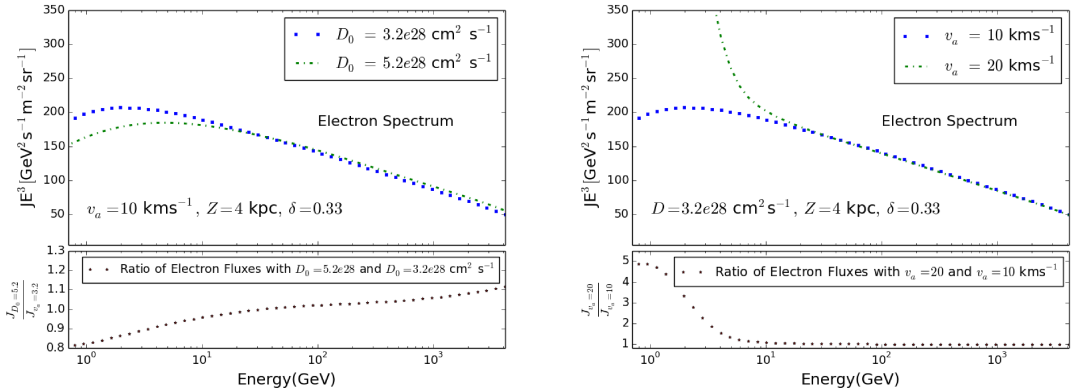


(b)

Figure 3.7: (a) Primary Electron Spectra calculated with $Z = 4$ kpc (blue dots) and $Z = 8$ kpc (green dotted line) are shown in the upper panel. With increasing diffusion zone height more low energy electrons can reach to the proximity of the earth. This difference is shown by plotting the ratio of fluxes $\left(\frac{J_{Z=8}}{J_{Z=4}}\right)$ in the lower panel of this figure, calculated for different diffusion zone heights. (b) Same as figure 3.7a but now the effect of diffusion coefficient (left) and alfven speed (right) on calculation of electron flux in GALPROP are shown.

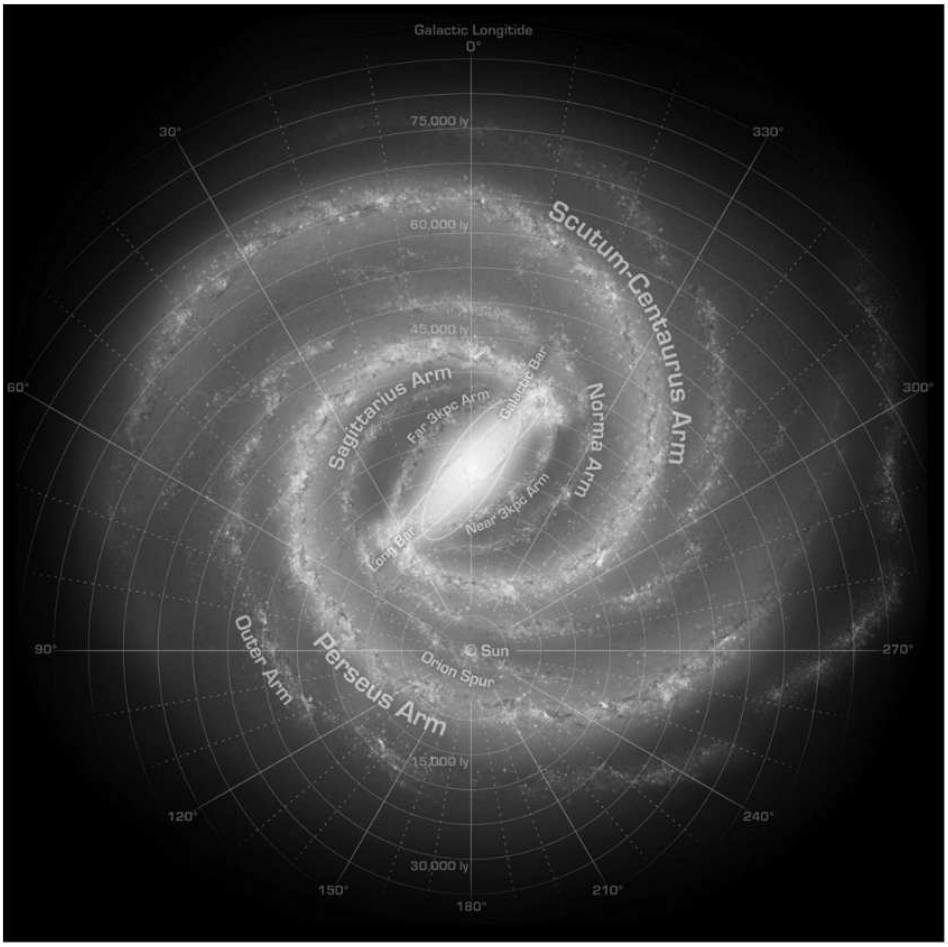


Figure 3.8: Schematic sketch of spiral arm structure of Milky Way in the galactic coordinates is shown here. Two main spiral arms are Perseus and Scutum-Centaurus and among several secondary arms the two dominant are Sagittarius arm and Outer Arms (Norma Arms) [153]. Solar system lies in a under-dense region near the Orion spur.

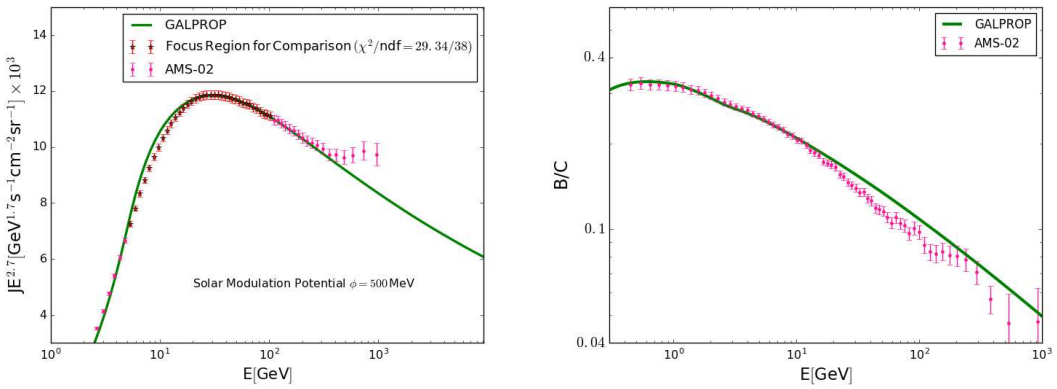


Figure 3.9: Proton spectrum and B/C ratio calculated with GALPROP (green line) for the propagation parameters given in table 3.2 are compared with the experimental measurements by AMS-02 (magenta dots).

Since all the CR species (nuclei, electrons and positrons) are propagated in GALPROP with the modified spiral arm source distribution in a single run, for accurate calculation of electron spectrum, a high value for the timestep-factor (0.90) with 10 years as the end-timestep is used. This ensure the convergence of solution in the Crank-Nicolson method used to solve the CR propagation equation in GALPROP [144]. Effect of timestep-factor and start-timesteps are shown in figure 3.12 for electron propagation coming from the annihilation of LKP DM.

## 3.6 Self-Consistent Simulation of Background and Dark Matter Signals

To study the self-consistent propagation of background cosmic rays and DM using GALPROP, we chose an example of 1 TeV LKP (Lightest Kaluza Klein Particle) [159, 160] as a candidate for DM [97]. As mentioned in section 2.2 LKP annihilation dominantly produces right handed fermions. However, LKP dark matter annihilates to SM Higgs also. The branching ratios used for LKP DM annihilation channels are as follows ($e^+, \mu^+, \tau^+ : 21\%, u, c, t : 11\%, H^+/H : 2\%$) [98, 161]. 700GeV LKP dark matter and a boost factor of 300 was used to compare the electron spectrum with AMS−02 data. The DM annihilation spectra at production is

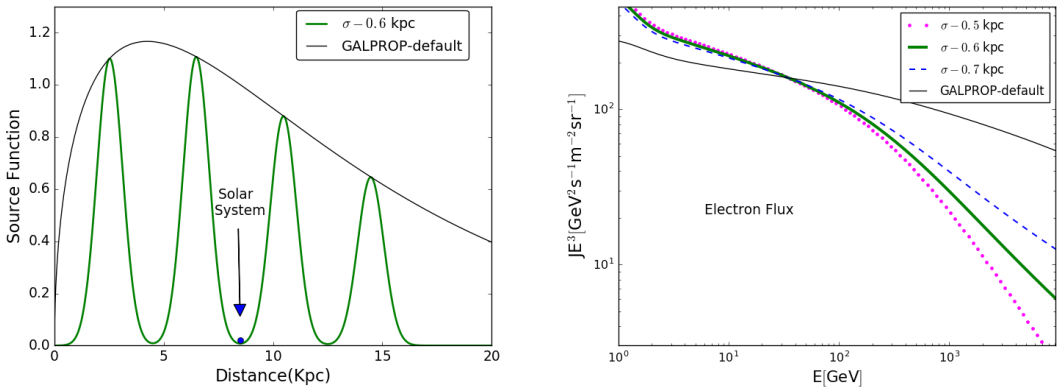


Figure 3.10: In the left panel we show the modified source function (in green thick line) with $\sigma = 0.6$ kpc (see eq. (3.26)) compared with the original GALPROP source function (black thin line). Position of the solar system is shown with the blue dot. Dependence of the $(e^+ + e^-)$ spectrum on $\sigma$ is shown in the right panel.

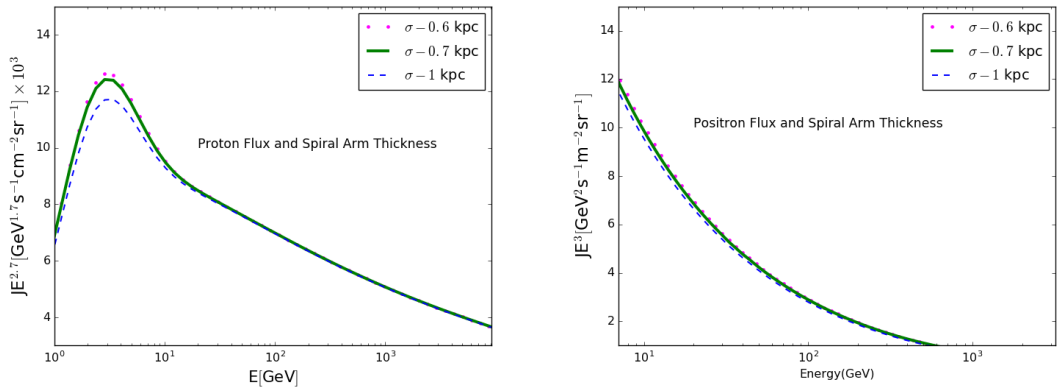


Figure 3.11: In the left panel proton spectrum for different sigma values are shown. Since the energy loss processes are less significant compared to electrons, the variation of proton flux with spiral arm thickness (governed by parameter $\sigma$ in eq. 3.26) is negligible. This is confirmed on the right panel of the figure where positrons, the secondary products of protons in galaxy, show similar effect as proton spectrum for different spiral arm thickness.

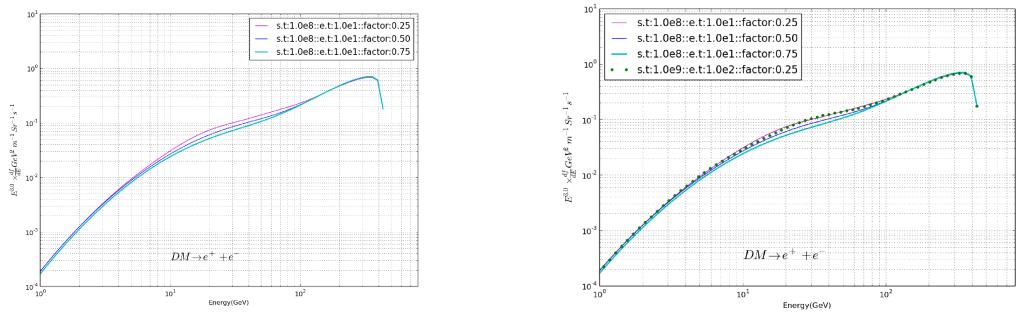


Figure 3.12: DM annihilation spectra calculated with different time step conditions are shown here. Figure on the left shows DM annihilation($e^+ + e^-$) spectra calculated with different time step factors but for same start and end time step values differ with each other. The figure on the right shows that when time step factor remains the same different start and end time step calculations(green dots and pink line) matches well.

obtained from PPPC4 for the branching fraction mentioned above. For DM annihilation, the flux at production per unit time and volume is given by eq. 2.3 and for DM density in milky way, NFW profile is assumed (eq. 2.5) and parameters related to this equation are described in section 2.3.2. We show an example of 400GeV LKP DM with an arbitrary boost factor, propagated simultaneously with the background spectrum in figure 3.13. The effect of modification for the energy bin effect in GALPROP is highlighted in the lower panel of the figure 3.13, where the fractional difference of fluxes calculated at two different binning is reduced to 1% with the modified version from 10% when calculated with original version.

To highlight the effect of the modification in regard to the fine energy resolution measurement of electron spectrum with CALET, at first the results were fitted to AMS-02 measurement [162]. The flux from the LKP DM is scaled by boost factor $x$, and the energy index of the background spectrum is adjusted by $\gamma_e$. This reduces the time consuming calculations which is otherwise necessary to determine propagation parameters in GALPROP precisely, to reflect the variability in the spectral shape. The background spectrum is normalized ($E_N$) at 11.4 GeV (one of the AMS-02 energy bins), the energy index adjustment can be written as $\phi_{\rm bkg} \times \left(\frac{E}{E_n}\right)^{\gamma_e}$. While comparing with AMS-02 measurements, the data points below 15 GeV are neglected to reduce the number of free parameters as the low energy

| *Parameter* | *Value* | *Unit* |
|---|---|---|
| $Z_{max}/\Delta Z$ | 6/0.25 | kpc |
| $X_{max}/\Delta X$ | 16/0.25 | kpc |
| $Y_{max}/\Delta Y$ | 16/0.25 | kpc |
| $E_{min}$ | 10 | MeV |
| $E_{max}$ | 100 | TeV |
| $D_0$ (Diff. coeff.) | $2.90 \times 10^{28}$ | $cm^2\,s^{-1}$ |
| $R_0$ (ref. rigidity for diff. coeff.) | 4 | GV |
| $\gamma_1/\gamma_2$ (injection index) | 1.70/2.45 | |
| $R_\gamma$ (Break in injection Index) | 7 | GV |
| $\delta$ (Diff. coeff. index) | 0.40 | |
| $v_A$ (Alfven Velocity) | 12.0 | $km\,s^{-1}$ |
| start-timestep | $6.4 \times 10^7$ | years |
| end-timestep | 10 | years |
| timestep-factor | 0.90 | |
| timestep-repeat | 20 | |

Table 3.2: GALDEF file parameters used for CR propagation in GALPROP.

| *Parameter* | $E_{factor}$ : 1.02 | $E_{factor}$ : 1.3 (Unmodified G.) | $E_{factor}$ : 1.3 (Modified G.) |
|---|---|---|---|
| $\chi^2$/NDF | 21.4/42 (fit) | 46.6/42 ($\gamma_c, x$ fixed) | 29.2/42 ($\gamma_c, x$ fixed) |
| $\gamma_c$ ($x = 1307$) | $-0.018$ | $-0.023$ | $-0.019$ |
| $x$ ($\gamma_c = -0.018$) | 1307 | 1126 | 1250 |

Table 3.3: Comparison of $\chi^2$ and fit parameters between Modified and Unmodified Galprop.

part of the CR spectrum get influenced by solar modulation, diffusive reacceleration and a possible break in the injection spectrum. We minimize the $\chi^2$ which is given by

$$\chi^2 = \sum \frac{((\phi_{\rm bkg} \times (E/E_N)^{\gamma_e} + \phi_{\rm DM} \times x) - \phi_{\rm AMS})^2}{\sigma^2_{\rm AMS}} \ , \tag{3.27}$$

where $\sigma_{\rm AMS}$ includes statistical and systematical error of AMS-02 measurement. We use the MINUIT [3] minimizer package for the minimization and compare the results obtained using $E_f = 1.3$ from the default GALPROP with the modified version. These results are compared to the results obtained from a very fine energy bin calculation ($E_f = 1.02$). To compare the results of the modification with fine bin calculations 3 different cases are considered - (1) $x$, and $\gamma_e$ both are kept fixed to the values obtained from the fit results with fine binning calculations, (2) $x$ fixed and $\gamma_e$ as a variable, (3) $\gamma_e$ fixed and $x$ as a variable. The results are shown in table 3.3 and for all the studied cases the fit results obtained from the modified version of GALPROP calculation are close to the fine bin calculation compared to the unmodified version.

[3]MINUIT: http://cern.ch/minuit

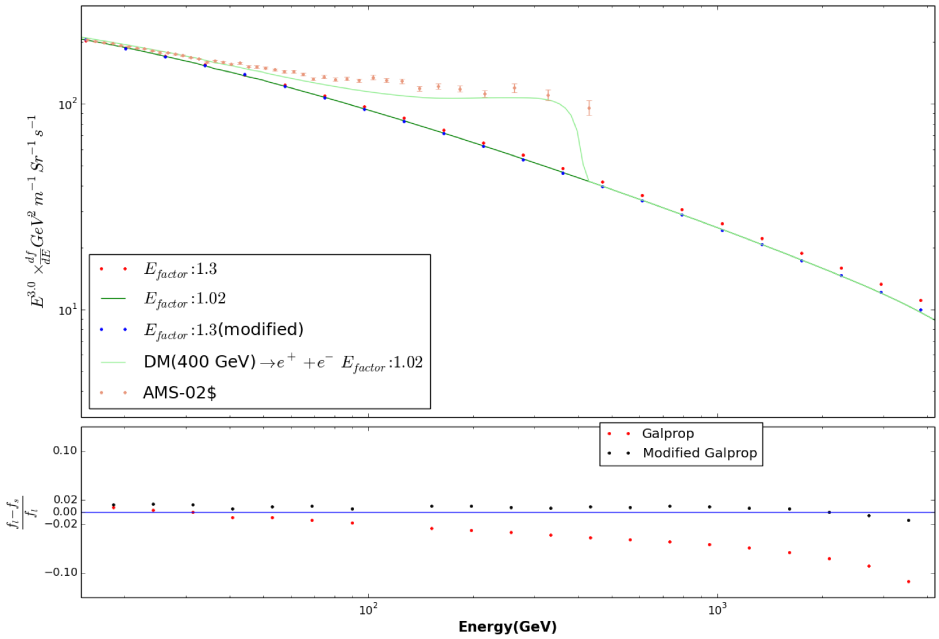


Figure 3.13: Red dots on the upper panel shows the background spectrum calculated with coarse binning and the green line shows of propagation of electron-positron pairs from the annihilation of 400 GeV LKP DM along with the background spectrum, calculated with fine energy bins. The mass of DM and boost factors are taken as 700GeV and 400. The effect of modification to reduce energy bin effect in GALPROP is shown with the blue dots. In the lower panel fractional difference of fluxes calculated with coarse energy bins and fine energy bins, with and without modification are shown with blue and red dots respectively.

# Chapter 4

# Discerning Signals of Fermionic Dark Matter Decay from Single Pulsar with CALET

## 4.1 Observance of Rise in Cosmic Ray Positron Fraction

As discussed in section 2.3.2, measuring charged CR fluxes at earth, especially antiparticles, are a unique probe for indirect detection of DM annihilation or decay. If DM particles annihilate or decay in the galactic halo, then it can produce $e^{\pm}$, $p\bar{p}$ and $\gamma$-rays. The charge particles which move under the influence of galactic magnetic field can produce a diffuse spectrum at earth. Anti-particles detected in the CR flux are usually thought to be of secondary origin. Primary CRs such as proton and electron interacting with the ISM and produces secondary particles which also consist of anti-particles. For example, if protons collide with a hydrogen atom at rest, producing charged pions. These pions can eventually decay to produce muons

which can produce positrons. This chain reaction is shown below

$$\begin{aligned} \mathrm{p} + \mathrm{H} \quad &\rightarrow \pi^+ + N, \\ \pi^+ \quad &\rightarrow \mu^+ + \nu_\mu, \\ \mu^+ \quad &\rightarrow e^+ + \bar{\nu_\mu} + \nu_e \end{aligned} \tag{4.1}$$

Assuming this secondary origin one can calculate the $\bar{p}$, $e^+$ flux from the estimated interaction cross-section of primaries with the the ISM [163] and models for galactic propagation. The results seem to be in agreement with the measurements up to 10 GeV [164]. Assuming positrons to be of secondary origin, the positron fraction $\left(\frac{e^+}{e^+ + e^-}\right)$ is expected to be a monotonically decreasing function of energy over few GeV. However, the recent measurements from Alpha Magnetic Spectrometer (AMS-02) in the ISS has confirmed that positron fraction rises above 10 GeV [8, 165]. This similar trend was initially observed in the measurements from PAMELA [66] and Fermi-LAT [166] detectors also. The grey band in the figure 4.1 represents the predicted positron fraction considering the secondary production mechanism and uncertainties in the modeling of galactic propagation and interaction cross-section of primaries. The difference in the AMS-02 and PAMELA measurement below 10 GeV can be accounted by different solar modulation potential due to different observation time. The disagreement between the Fermi-LAT and AMS-02 data points at few tenths of GeV may result from high systematics associated with the Fermi-LAT experiment, which is a dedicated $\gamma$-ray detector.

## 4.2 Dark Matter or Pulsar as Extra Source of Cosmic-Ray Positrons

As mentioned in the previous section, the rise of positron fraction which is difficult to explain considering only the secondary production, requires the existence of high energy positron source(s). Two of the leading proposals for positron sources are- 1) Nearby pulsars injecting high energy positrons into the ISM [167–169] and 2) DM particles decaying or annihilating in the galactic halo [170–174]. Apart from these two interpretations few other interpretations for positrons excess are if the shock-waves in supernova remnants accelerate protons then from hadronic interaction it

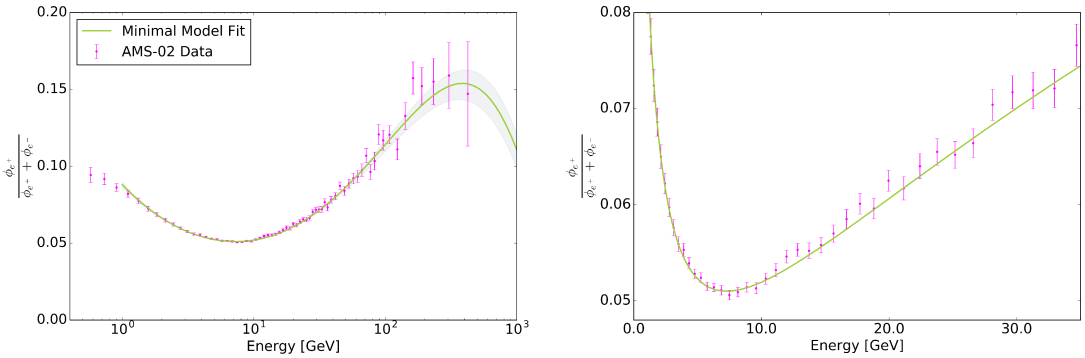


Figure 4.1: Left: Positron fraction as measured with AMS-02 detector is shown here. The minimal model described in this reference [8], is fitted to the experimental data points. Right: This figure shows the decrease in the positron fraction till 8 GeV, followed by steady increase, which is in contradiction to the the usual understanding of the secondary production.

can produce pions ($\pi^{\pm}$), which can decay to produce positrons, electrons [175]. It is also argued here [142], considering spiral arm distribution of Milky-way galaxy, AMS-02 positron fraction data can be reproduced considering shock acceleration scenario with nearby source contribution significantly reduced to avoid tension with anisotropy measurements [176].

In the annihilating DM scenario to explain the rise in positron fraction, velocity averaged cross-section ($\langle\sigma\,|v|\rangle$) needs to be several order higher than the value at 'freeze-out' ($3 \times 10^{-26}\,\mathrm{cm^3\,s^{-1}}$), which is necessary for the DM abundance as seen today by WMAP/PLANCK [81, 82]. As shown in these works [177, 178], to account for the current positron fraction DM must annihilate to leptons with interaction cross section ($3 \times 10^{-24}$–$10^{-23}\,\mathrm{cm^3\,s^{-1}}$). As mentioned in section 2.2 and shown in figure 2.5, increasing interaction cross-section implies DM particles would remain in thermal equilibrium in the early universe longer and this would significantly reduce DM density, contradicting CMB measurement results. Also, considering the clumpiness properties of DM, the N-body DM simulation shows that boost factor cannot be more than 10-20 [179, 180]. To overcome this problem models for enhancement of annihilation cross section has been proposed namely Sommerfeld or Breit-Weigner enhancement [181, 182]. But this enhancements are usually accompanied by excess $\gamma$-ray production and severely restricted [183, 184].

Restriction on annihilation or decay products of DM to leptons is necessary as leptonic product ensures we don't need to consider about recent anti-proton measurements [164, 185]. Annihilation to quarks, gauge bosons or even tau leptons at a rate which is compatible with leptonic rate to produce positrons necessary to explain positron fraction is accompanied by high $\gamma$-ray flux from prompt emission at the galactic center [183, 186] and inner galaxy [187].

Compared to the annihilation scenario the decaying DM scenario needs no such enhancement in cross-section or boost factor and can naturally explain the positron excess if the lifetime of the DM is around $\sim 10^{25}$ s [170]. To explain the positron excess several DM decay models are proposed including candidates like neutralino, gravitino, gaugino and fermionic DM [188–192] and studied in detail to set constraints. Unstable DM of mass in the range GeV-TeV which can explain positron excess also encounter problems from diffuse $\gamma$-ray constraint [193] but just like the annihilation scenario the $\gamma$-rays from the decay can be lowered provided it decays only to electron and muon as it is shown here that $\tau$-leptons produce most $\gamma$-rays among the leptonic decay products [194]. Several DM decay models and $\gamma$-ray constraint on them are shown in this reference [195].

Like DM, pulsars which are rapidly spinning neutron stars can also act as a source for CR positrons. The rotating magnetic field of pulsars can tear particles away from the surface. These particles get accelerated in the pulsar magnetosphere and the mechanism of this acceleration is described by either polar cap model [196, 197] or outer gap model [198]. In these mechanisms, accelerated electrons or positrons while propagating through the intense magnetic field of the pulsar produce a synchrotron radiation. This radiation has sufficient energy to produce electron-positron pair which then get accelerated by the electric field of the neutron star. These charged particles usually get trapped in the surrounding nebula and the relativistic wind produced by the pulsar releases them in the ISM. Source of the most emission from the Pulsar Wind Nebulae (PWNs) are the rotational energy of the pulsars. Newly formed PWNs can have rotational periods of hundreds of milliseconds and as a result of magnetic-dipole braking the period eventually slows down. If an isolated pulsar has a period $P$, which can be determined from the observation of pulsed signal, then the rate of change of period is given by $\dot{P}$. The energy loss rate of the pulsar ($\dot{E} = \frac{dE}{dt}$) can be written as $\dot{E} = 4\pi^2 I \frac{\dot{P}}{P^3}$ and this is

known as spin down luminosity of a pulsar, where $I$ is the moment of inertia of the neutron star. Young pulsars lose their energy rapidly, typically within $\sim 10^5$ years, due to high rotational speed. It is shown here [167], that total energy output of a mature pulsar is $\approx 10^{49}$ erg, which is good enough to account for the high energy positron flux. The spectral shape of electrons or positrons from a pulsar is often parametrized as a power law with exponential cut-off in energy [199].

$$\frac{dn}{dE} \propto E^{-\alpha} \exp(-E/E_{\rm pwn}) \,, \tag{4.2}$$

where $\alpha$ and $E_{\rm pwn}$ are the spectral index and energy cut-off of a pulsar. It's shown here that this parametrization can correspond well to that of a single pulsar [200]. Moreover, from the ATNF catalog [201], several nearby pulsars with distance less than 500 parsec and age $4 \times 10^4$–$4.5 \times 10^5$ years can provide a single source explanation of the positron excess measured by AMS-02 [202]. In the same reference [202] it is also shown that, if contributions from multiple pulsars are included to calculate positrons that can account for positron excess, it can produce spectral feature in the spectrum due to different cut-off energies of the pulsars. During the preparation of this thesis, High-Altitude Water Cherenkov (HAWC) collaboration showed that considering positron contribution from two of the nearest pulsars (Geminga and Monogem), it is not possible to explain the observed positron excess [203]. However, this explanation is based on the low diffusion coefficient derived from their measurements at several 10 TeV energies and this conclusion requires the extrapolation of this diffusion coefficient by the assumption of a power law to the $\sim$ 100 GeV region relevant for the sources of the positron excess.

To distinguish the origin of the positron excess from CR measurements, one tool is the search for anisotropy of the arrival directions of the positrons or electrons + positrons [176,204,205]. If the high energy electron-positron spectrum is dominated by a single nearby source then it is possible to detect a dipole anisotropy in the arrival direction. Even considering diffusion where the direction information of the charged particles get lost, high energy electron/positrons from nearby pulsars can still give rise to a small anisotropy. The anisotropy associated with the diffusive propagation is given by

$$\delta_a = \frac{I_{\rm max} - I_{\rm min}}{I_{\rm max} + I_{\rm min}} = \frac{3D \left| \nabla \left( dN/dE \right) \right|}{c \left( dN/dE \right)} \,, \tag{4.3}$$

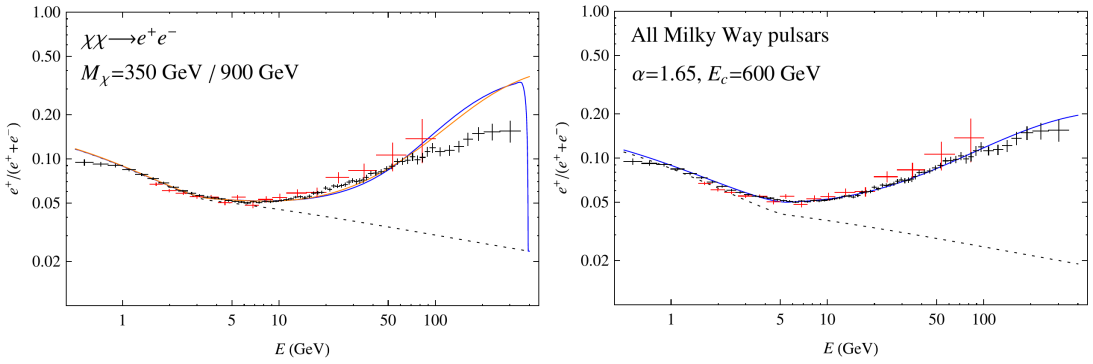


Figure 4.2: *Left*: Explaining CR positron fraction considering an annihilating DM $\rightarrow e^+ e^-$ of mass 350 GeV (blue line) and 900 GeV (red line) as extra source. The flux is compared with PAMELA (red errorbars) and AMS-02 (black errorbars) measurements. Considering classical model of CR propagation the positron fraction will follow the black dotted line. *Right*: Same as figure on the left but now the source of positron are the milky way pulsars. The parameters $\alpha$, $E_{\rm pwn}$ in eq 4.2 describe the shape of the spectrum. These plots are taken from the reference [207] as an example to show DM and Pulsar as possible sources for explanation of positron excess.

where $\nabla\,(dN/dE)$ is the gradient of the electron/positron spectrum. However, to detect statistically significant signals, a large of events in the detector is necessary. Compared to this nearby source scenario, in the case of DM where annihilation or decay throughout the Milky Way smoothen the anisotropy, with a possible small excess from the direction of galactic center [204]. It is shown in this work [206] that if the DM annihilations produced in a nearby clump (subhalos) that can explain positron excess is excluded as a source of anisotropy measurement from the non-observation of anomalous $\gamma$-rays in Fermi-LAT. Apart from electron/positron measurement, observance of anti-protons, anti-deuterons and diffuse $\gamma$-ray measurements are also necessary for distinction between these two possible cases and setting up theoretical limits.

## 4.3 3-body Decay of Dark Matter and Fermionic Dark Matter Model

Motivation for the choice of DM decay as an extra source for positron excess in this study over the annihilation scenario is already described in the previous section. Among many DM decay scenarios, 3 body leptonic decay is considered as a possible source of CR positron excess. The 3-body DM decay generally have a softer spectrum compared to 2-body decay, which resembles the recent CR measurements [208, 209]. Choice of leptonic decay products also ensure bypassing the anti-proton constraints and leptonic decay products produce less prompt $\gamma$-rays compared to hadrons or gauge bosons. For a TeV scale DM that decays to leptons (DM $\rightarrow l^- l^+ \nu$), namely a charged standard model lepton+anti-lepton pair and a neutrino, the contribution from the DM decay is given by

$$\phi_{\rm DM} = \frac{1}{\tau_e}\phi_e + \frac{1}{\tau_\mu}\phi_\mu + \frac{1}{\tau_\tau}\phi_\tau \tag{4.4}$$

with $\phi_e$, $\phi_\mu$, $\phi_\tau$ being the $e^+$ (identical to $e^-$) decay spectra for $ee\nu$, $\mu\mu\nu$, $\tau\tau\nu$ channel respectively, propagated with GALPROP.

We choose a fermionic DM model proposed in this work [210], where in the new model, Standard Model (SM) is extended by 3 fermionic singlets and 2 Higgs doublets. According to this proposed non-supersymmetric model under the new gauge group $SU(2)_L \times U(1)_Y \times U(1)_{B-L}$, quantum numbers for the 3 fermionic singlets $(N_L, \psi_R, S_R)$ including the neutral DM candidate $(N_L)$ is $(1, 0, -1)$. $N_L$ is a singlet under $SU(2)_L$ and the hypercharge is 0, and also the lightest among the 3 fermions, making it a possible DM candidate. The Lagrangian terms that describe the decay of the DM to SM lepton anti-lepton pair and neutrino are described as $h_{\alpha\beta}\eta^\dagger \overline{N} l + f\chi^\dagger ll$. The quantum numbers for the 2 Higgs doublets under the new gauge group are $(1, -2, 0)$ and $(1, -2, -2)$ for $\eta$ and $\chi$ respectively. So the interaction of $\eta$, $\chi$ breaks the lepton number by 2 units above TeV scale (2.5–4 TeV) and this cause the DM to decay. The heavy scalars $(\eta^-, \chi^-)$ are assumed to be created from the decay of a hidden inflaton field $\phi_0(1, 0, 0)$ just above Electro-Weak scale. The particles of the model is shown in a representative diagram 4.3. The

main interactions are described in the following Lagrangian :

$$\begin{aligned} L_{eff} \supseteq & \frac{1}{2}(M_N)_{\alpha\beta}\overline{N^c_{\alpha L}}N_{\beta L} + \frac{1}{2}(M_\psi)_{\alpha\beta}\overline{(\psi_{\alpha R})^c}\psi_{\beta R} \\ & + \frac{1}{2}(M_S)_{\alpha\beta}\overline{(S_{\alpha R})^c}S_{\beta R} + (g_S)_{\alpha\beta}(\overline{S_{\alpha R}}Hl_{\beta L}) \\ & + (g_\psi)_{\alpha\beta}(\overline{\psi_{\alpha R}}Hl_{\beta L}) + \mu\eta H_1 H_2 + m^2\eta^\dagger\chi \\ & + f_{\alpha\beta}\chi^\dagger l_{\alpha L}l_{\beta L} + h_{\alpha\beta}\eta^\dagger\overline{N_{\alpha L}}l_{\beta R} + h.c \end{aligned} \tag{4.5}$$

The Lagrangian describing the $B-L$ violation is described by the interaction of two added Higgs doublets $M^2\eta^\dagger\chi$ having different $B-L$ quantum numbers and imposing the condition $m << M_\eta$, $M_\chi$, makes the DM unstable on a cosmological scale and the slow DM decay explains the positron excess. However the lifetime of the DM is more than the age of the universe and it is shown in the same work, the slow decay of such a DM ($N_L \to ee\nu$, $\mu\mu\nu$, $\tau\tau\nu$) is capable of explaining the PAMELA, AMS-02 and Fermi-LAT measurements of CR positrons [210]. In the decay of the lightest fermion $N$ to SM leptons the outgoing neutrino is of different flavor than the lepton anti-lepton pair. So a decay to tau lepton anti-lepton pair will be accompanied by a muon or electron neutrino ($N \to \tau^+\tau^-\nu_e(\nu_\mu)$). This is important in the theory as the decay of this DM breaks the lepton number for each flavor ($L_e(L_\mu)$) by a unit and the total lepton number by two units ($L = L_e + L_\mu + L_\tau$). The lifetime of the DM is given by

$$\begin{aligned} \tau = & 8.0\times10^{25}\text{s}\left(\frac{10^{-2}}{h}\right)^2\left(\frac{10^{-8.5}}{f}\right)^2\left(\frac{50\text{GeV}}{m}\right)^4 \\ & \times\left(\frac{m_\phi}{10^6\text{GeV}}\right)^8\left(\frac{3\text{TeV}}{M_N}\right)^5 \end{aligned} \tag{4.6}$$

This model has two important implications for the study of positron excess from DM decay and $\gamma$-ray production associated with DM decay. The branching ratios of the outgoing leptons are proportional to the inverse of the decay time $\left(\frac{1}{\tau_e}, \frac{1}{\tau_\mu}, \frac{1}{\tau_\tau}\right)$ of the DM for the individual decay channels ($ee\nu$, $\mu\mu\nu$, $\tau\tau\nu$) which depends on the coupling constants $(h, f)$ at both vertices of the decay process. These coupling constants $(h, f)$ are completely independent of the lepton mass hierarchy [210], making $\frac{1}{\tau_e}$, $\frac{1}{\tau_\mu}$, $\frac{1}{\tau_\tau}$ completely free parameters in our study. Also, the decay of the DM is mediated by heavy scalar $\eta$, $\chi(\sim 10^3$ TeV), so the lifetime can be assumed to be negligible, making 4-point scalar interaction a good approximation for the DM decay process. We use this assumption to calculate the energy

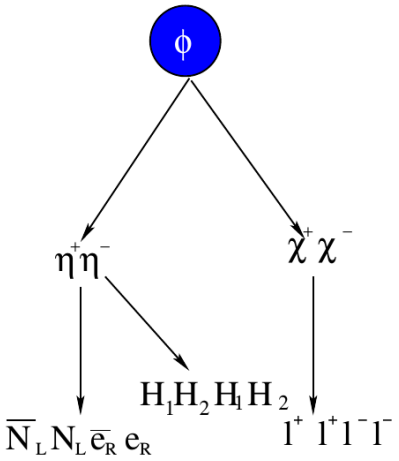


Figure 4.3: Particle contents of the new model [210], where a hidden scalar field $\phi$ decays to produce the Higgs doublets $\eta$, $\chi$. Interaction of $\eta$, $\chi$ breaks down the $B-L$ symmetry to induce a prolonged lifetime for the fermionic DM $N_L$. $H_1$, $H_2$ are SM Higgs and $l$ s are SM leptons.

distribution of the charged leptons ($e^+e^-$, $\mu^+\mu^-$, $\tau^+\tau^-$) which is given by eq. 4.7.

$$\frac{1}{\Gamma}\frac{d\Gamma}{dx} = 2x^2(3-2x) \tag{4.7}$$

where $x = E/E_{\rm max}$ and $E_{\rm max} = 0.5\,{\rm M_{DM}}$ and $\Gamma$, $\rm M_{DM}$ are the decay rate and mass of the DM respectively. The detailed calculation is shown in Appendix A. From this initial energy distribution, the $e^+$ and $e^-$ spectrum $\frac{dN}{dE}$ produced per decay is calculated using the event generator PYTHIA (Version 8.2) [115]. The spectra for $e^+$ and $e^-$ are identical and the $e^+$ spectrum is propagated in GALPROP [33, 211].

## 4.4 Parametrization of Observed Cosmic Ray Electron and Positron Flux

It is necessary to parametrize the locally observed spectra to reflect the variability due to many free parameters of injection and propagation, which can be effectively studied with numerical CR propagation calculation only for exemplary cases. We

use a parametrization based on the assumption that distant supernova remnants (SNR) give a power law primary electron spectrum, to which a secondary component from nuclei interactions with the ISM is added. This is described by two power law indices $\gamma_p$, $\gamma_s$ and two coefficients $C_p$, $C_s$ which describe the relative weights of the spectra for primary electron and secondary flux. The radiative energy loss processes for the primary electrons including synchrotron radiation, inverse Compton radiation is represented by the exponential cut-off at energy $E_d$. Since the secondary electrons and positrons are product of primary particles' interaction in ISM, this cut-off energy term is absent for the secondaries. With these parameters the total flux (primary+secondary) can be written as

$$\phi_T(E) = 2\phi_{\text{extra}} + C_p E^{\gamma_p} \left( 2\frac{C_s}{C_p} E^{\gamma_s - \gamma_p} + e^{\left(\frac{-E}{E_d}\right)} \right) , \tag{4.8}$$

where $\phi_{\text{extra}}$ is the flux from the extra sources emitting electron-positron pairs. For the pulsar scenario the parametrization is influenced by eq. 4.2 and it can be written as

$$\phi_{pn} = C_{pn} E^{\gamma_{pn}} e^{-\left(\frac{E}{E_{pn}}\right)} . \tag{4.9}$$

Here the weight of diffuse spectra is given by $C_{pn}$, power law index $\gamma_{pn}$ (common for electron and positron) and a cut-off energy $E_{pn}$. The positron flux from eq. (4.8) can be written as

$$\phi_{e^+} = \phi_{\text{extra}} + C_s E^{\gamma_s} . \tag{4.10}$$

This parametrization is fitted to the current measurements of the electron and positron flux to determine values for the free parameters. By comparison with the results of numerical calculation using GALPROP, the correspondence to propagation conditions compatible with nuclei spectra measurements is confirmed, as mentioned before. Also the valid range of the cut-off energy $E_d$, which has only influence in the TeV region and cannot be determined from current experimental data, is defined in the same way.

| | Parameter | Definition | Comment |
|---|---|---|---|
| Bkg. | $C_p$ | Absolute normalization of primary $e^-$ flux | Free parameter |
| | $\frac{C_s}{C_p}$ | Ratio of absolute normalization of secondary to primary flux | Free parameter, always $< 1$ |
| | $\gamma_p$ | Primary $e^-$ index | Free parameter |
| | $E_d$ | Background cut-off energy | In AMS-02 fit 1,2,5,10 TeV fixed values are studied |
| | | | Free parameter in CALET simulated data fit |
| | $\gamma_p - \gamma_s$ | Difference between primary and secondary electron indices | $\gamma_p - \gamma_s \approx \delta = 0.4$, fixed from the propagation model in Appendix B |
| DM | $\frac{1}{\tau_e}, \frac{1}{\tau_\mu}, \frac{1}{\tau_\tau}$ | Inverse of the decay time of the lepton channels $(ee\nu, \mu\mu\nu, \tau\tau\nu)$ | Free parameters |
| Pulsar | $\frac{C_{pn}}{C_p}$ | Ratio of absolute normalization of pulsar to primary flux | Free parameter, always $< 1$ |
| | $\gamma_p - \gamma_{pn}$ | Difference between pulsar and primary electron indices | Free parameter |
| | $E_{pn}$ | Cut-off energy for pulsar parametrization | $E_{pn} = 1$TeV, fixed parameter in AMS-02 fit |
| | | | Free parameter in CALET simulated data fit |

Table 4.1: Parameters used in the parametrization (eq. 4.8, eq. 5.5 and eq. 4.4) of the local $(e^+ + e^-)$ and $e^+$ spectra including background (Bkg.) and extra sources (DM and Pulsar) are listed here.

## 4.5 Positron Excess with 3-Body Dark Matter Decay and Single Pulsar

The parametrization with DM as extra source is used to compare with the AMS-02 $e^+ + e^-$ and $e^+$ flux measurements and the free parameter values (see table 4.1) are determined from the fitting. To avoid the low-energy effects in the CR spectrum coming from charge dependent solar modulation potential, diffusive reacceleration, a possible break in the low energy region ($\sim 9\pm3$ GeV) of the CR spectrum [212], data points above 15 GeV are considered. The upper bound of the fit range is 1 TeV due to unavailability of high-resolution data points from AMS-02 measurements. Above 15 GeV, a charge independent solar modulation is applied to the parametrization with a fixed value of 500 MeV [213], for both electrons and positrons, assuming force-field approximation (eq. 1.23). The background cut-off energy ($E_d$) influences only the TeV region of the spectrum and it cannot be determined from the available experimental data. To study the effect of $E_d$ on the shape of the spectrum various fixed values (1 TeV, 2 TeV, 5 TeV, 10 TeV) are tested. Vela SNR, the most influential nearby source with distance around 1 kpc and age less than $10^5$ years [58] can contribute in the TeV region of the electron spectrum and this is calculated using GALPROP with the same propagation parameters used for nuclei, electrons and DM propagation calculation (see section B). Different values of $E_d$ can reflect the influence of spiral arm thickness of milky-way on the $e^+ + e^-$ spectrum and also the variability of the contribution from Vela due to gradual or delayed electron release. An example of fit to AMS-02 measurements with 2 TeV DM is shown in figure 4.4. As the branching ratios are free parameters, the fit converges to 0.77% $\tau\tau\nu$ channel and 23% $ee\nu$ channel with a lifetime of $7.23 \times 10^{25}$ s. For this case the background cut-off energy $E_d$ is fixed to 2 TeV. In table 4.7b, the effect of background cut-off energy on the branching ratios of outgoing particles with different DM mass is shown. Now this DM spectrum which is characterized by a drop around half of the DM mass, is significantly different from a single pulsar spectrum, as shown in figure 4.5. For the pulsar as extra source to explain the positron flux and $e^+ + e^-$ flux, pulsar cut-off energy ($E_{pn}$) is kept fixed at 1 TeV and $E_d$ at 2 TeV. Fixing the pulsar cut-off energy here does not affect our study with CALET expected data, since CALET expected data is calculated with DM as extra source.

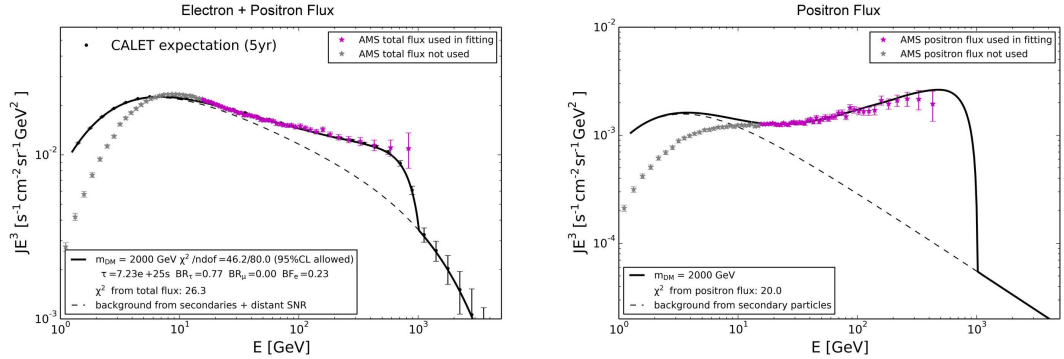


Figure 4.4: 2 TeV fermionic DM decay spectra (black line) on top of the background (dotted line) are fitted to the AMS-02 ($e^+ + e^-$) flux (left) and positron flux (right) shown with magenta error bars, resulting in a branching fraction of 0.77 for $\tau\tau\nu$ channel and 0.23 for $ee\nu$ channel (solid line). $E_d$ is 2 TeV.

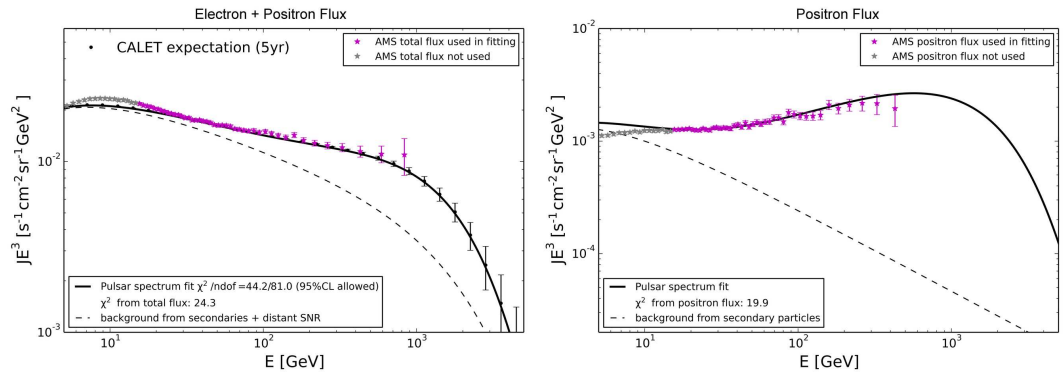


Figure 4.5: The parametrization of the background (dotted line) and a single pulsar as extra source (solid line) is fitted to the AMS-02 ($e^+ + e^-$) flux (left) and positron flux (right) (magenta error bars), assuming $E_{pn} = 1$ TeV and $E_d = 2$ TeV.

## 4.6 Diffuse $\gamma$-ray Constraint on Dark Matter Decay Model

### 4.6.1 Primary and Secondary $\gamma$-ray Production from Dark Matter Decay

DM particles that can annihilate or decay to produce charged leptons will inevitably induce significant amount of $\gamma$-rays from Final State Radiation (FSR) or secondary $\gamma$-rays from Bremsstrahlung and IC scattering during the propagation of charged decay or annihilation products. Fermi-Lat group reported their measurement of diffuse isotropic $\gamma$-ray background at higher latitudes ($|b| > 20^{\circ}$) [193] with energy of the measurement extending up to 820 GeV. Therefore, the IGRB is naturally used as a powerful tool to constrain the DM explanation of the positron excess. The expected DM induced $\gamma$-ray flux from a direction $\theta$ averaged over an opening angle $\delta\theta$ of the detector is given by

$$\frac{d\phi_\gamma}{dE} = \frac{1}{8\pi}\int_{\delta\theta}\frac{d\Omega}{\delta\theta}\underbrace{\int_{\text{l.o.s}} dl\,\rho}_{\text{Astrophys.}} \times \underbrace{\left(\frac{1}{M_{\text{DM}}}\sum_f \frac{\Gamma_f dN_f}{dE}\right)}_{\text{Particle Phys.}}, \tag{4.11}$$

where the integration is performed along the line of sight. Other terms are defined in eq. 2.4. The term in the parenthesis contains all the particle physics input and $\int d\Omega \int \rho dl$ is the astrophysical factor known as 'J-factor'. In figure 4.6 an example of $\gamma$-ray flux associated with 1 TeV DM with considerably large lifetime $3 \times 10^{27}$ s for various channels are shown.

Decay of the fermionic DM to the charged leptons ($e^{\pm}$, $\mu^{\pm}$, $\tau^{\pm}$) would produce a diffuse $\gamma$-ray flux in the galactic DM-halo. So it is necessary to test the $\gamma$-ray flux from the DM decay model (capable of explaining positron excess) with the Fermi-LAT [193] diffuse $\gamma$-ray measurement taken at higher latitudes ($|b| > 20^{\circ}$) in the sky. This isotropic diffuse $\gamma$-ray background (IGRB) is obtained after subtracting the resolved sources, diffuse galactic $\gamma$-ray emission, contribution from the Sun and the CR background, from the total all sky $\gamma$-ray emission. Since the measurement considers region beyond the galactic center, it reduces the background from galactic astrophysical sources. Thus, comparison of $\gamma$-ray flux accompanied

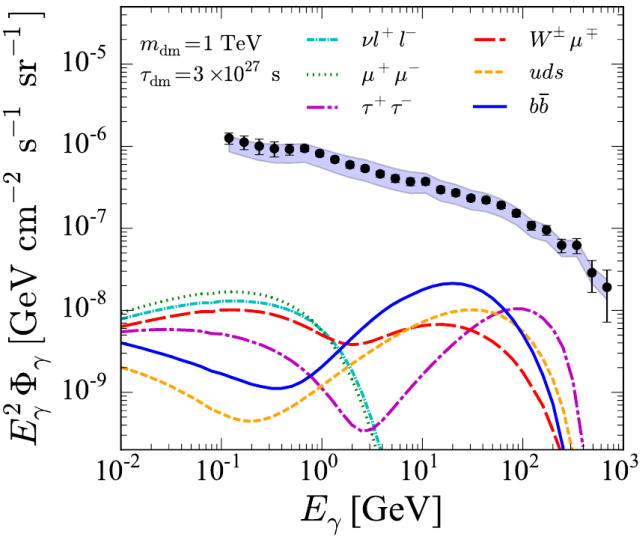


Figure 4.6: $\gamma$-ray flux from the decay of 1 TeV DM with lifetime $\tau = 3 \times 10^{27}$ s is compared with Fermi-Lat measurement (black circles) including the systematic error band. The decay channels are $\nu ll$ (cyan), $\mu^\pm$ (blue dotted line), $\tau^\pm$ (magenta), $W^\pm \mu^\pm$ (red), $uds$ (yellow), $b\bar{b}$ (blue line). Image reference: [214]

by DM decay with the IGRB measurement gives the strongest constraint on DM models. This IGRB measurement in the several 100 GeV region at the higher latitudes of the sky is only provided by Fermi-Lat currently. Detectors like CALET, capable of absorbing the full $\gamma$-ray shower within the thick calorimeter in the TeV energy, will provide precise measurements in near future and the results can be reaffirmed by comparing measurements from Fermi-LAT, CALET [53] and also DAMPE [48, 215].

The $\gamma$-ray fluxes from the FSR and decay of the primary decay products of the DM have been calculated with PYTHIA [115] assuming NFW profile. For calculation of secondary $\gamma$-rays, interaction of the charged dray products with the interstellar radiation field (ISRF) is considered. Using the default ISRF [148] provided by GALPROP the secondary $\gamma$-ray flux at latitudes $|b| > 20^\circ$ is calculate for different DM models. The secondary $\gamma$-rays are expected to have lower energy than the primary component, which is verified in later chapter.

### 4.6.2 Dark Matter Decay Models with Low $\gamma$-ray Flux

For the 2 TeV DM model originally proposed in here [210] to explain the PAMELA measurements decays mostly to $\tau\tau\nu$ channel (73%). Since the $\gamma$-ray flux from the DM decay model depends strongly upon the DM mass and decay products, the possibility of finding low $\gamma$-ray DM models are investigated.

As presence of $\tau$ leptons in the decay product of the DM produces more $\gamma$-rays compared to $e$ and $\mu$ leptons [194], the $\tau\tau\nu$ component from the decay products is reduced. Due to completely free coupling constants, as described in section 4.3, the branching ratio of the decay products are free parameters. Adapting all other free parameters in each step and starting with the parameters obtained from the initial fit, the $\tau\tau\nu$ component is reduced in steps until either the $\chi^2$ of positron flux or $(e^+ + e^-)$ flux exceeds 95% CL, or the scale factor for $\tau\tau\nu$ channel reaches zero. The branching ratios obtained from the initial fit (where all decay channels are used) and the fit with the reduced tau contribution are given in table 4.2 for three different values of DM mass and $E_d$. It is shown that a good fit with completely removed $\tau\tau\nu$ channel is possible for 1.5 TeV DM with $E_d \geq 2$ TeV. For 1 TeV DM model $\tau\tau\nu$ channel can be reduced to zero only for $E_d = 10$ TeV. For 1 TeV DM model even including $\tau\tau\nu$ channel it's not possible to find a good fit for $E_d \leq 2$ TeV. DM Models with low DM mass and decay restricted to $\mu\mu\nu$ and $ee\nu$ channel) can be a unique possibility to explain the positron excess by DM while not producing excess $\gamma$-rays in conflict with current measurements [1]. For 1 TeV DM model with no decay to $\tau\tau\nu$ channel, the fit converges at branching ratios of 0.60 for $\mu\mu\nu$ channel and 0.40 for $ee\nu$ channel, for $E_d = 10$ TeV (figure 4.7b). The 1.5 TeV DM model with decay restricted to $\mu\mu\nu$ and $ee\nu$ channel, branching ratios obtained from the best fit are 0.73 for $\mu\mu\nu$ channel and 0.27 for $ee\nu$ channel, for $E_d = 2$ TeV, shown in figure 4.7a. This 1.5 TeV DM model matches well with the new AMS-02 positron flux [216], making this another case to be studied. It is important to note that uncertainties in the choice of the propagation parameters that were used to calculate the positron flux should be reflected in the lifetime of the DM and thus on the calculated $\gamma$-ray flux (eq. 4.11). Later using 1.5 years of CALET flight

[1] Later in chapter 5, using CALET flight data, 800 GeV DM mass was found to be allowed at 95% CL and the $\gamma$-ray fluxes associated with DM decay are shown in page 122.

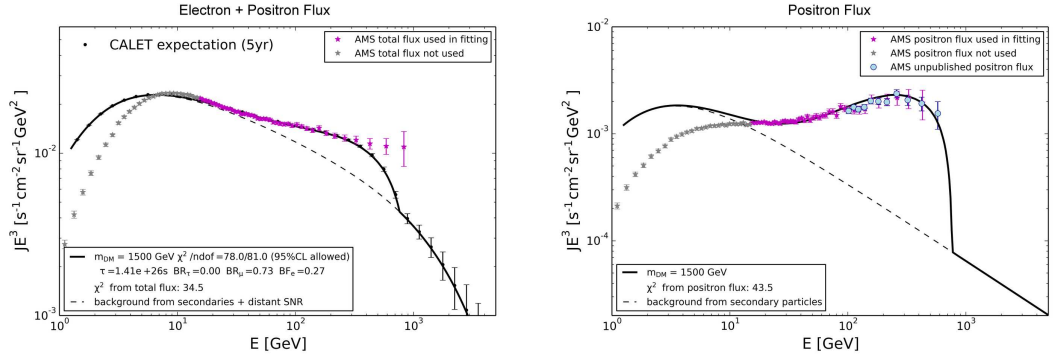


(a)

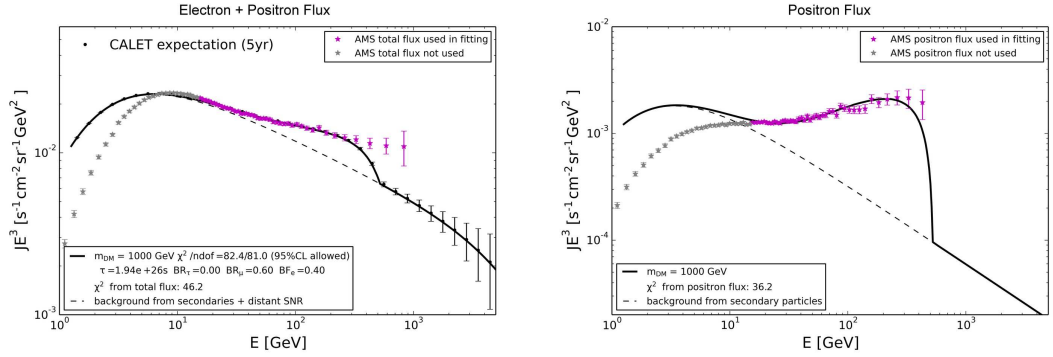


(b)

Figure 4.7: (a) 1.5 TeV DM (without $\tau\tau\nu$ channel) decay spectra on top of the background (dotted line) are fitted to the $(e^+ + e^-)$ and positron flux from AMS-02 with $E_d$ set to 2 TeV. This decaying DM matches well the new 5-year AMS-02 positron flux data (shown with cyan dots) which was not used in the fit. (b) As figure 4.7a but for a 1 TeV DM with $E_d = 10$ TeV.

data it is shown that 800 GeV DM decaying only to $\mu\mu\nu$, $ee\nu$ is well compatible with Fermi-Lat $\gamma$-ray measurements. Also the shape of the DM halo may influence the charged CRs ($e^+$, $e^-$) and $\gamma$-ray flux. It's also shown using the "Dark-Disc" model [217] the $\gamma$-ray constraints can be relieved significantly. In this model the DM halo is divided in two parts where the active part close to the galactic disc is responsible for positron excess and the passive part consists of most of the DM halo which does not contribute significantly in the measured CR spectrum. To construct and study the effect of this kind of DM halo is not performed in this thesis.

## 4.7 Discerning Dark Matter Decay Spectra from Single Pulsar Spectra using CALET

To estimate CALET's capability to distinguish a DM signal from a single pulsar source, we perform these following steps :

1. To calculate CALET expected data assuming 5 years of data taking, the best fit scenarios with DM as extra source (see section 4.5) was used.
2. 10000 event samples were generated which takes into account the statistical fluctuations in the event rates, representing different outcomes of the $(e^+ + e^-)$ flux measurement in each of the DM decay scenarios.
3. The parametrization with single pulsar as extra source was then fitted to the each of the 10000 simulated $(e^+ + e^-)$ CALET data samples for the DM and the positron flux measured by AMS-02, and a $\chi^2$ distribution is obtained.
4. The DM model is then re-fitted to these same data points and a $\chi^2$ distribution for the DM model is obtained.
5. These two $\chi^2$ distributions are compared with each other to determine CALET's capability to discern between the fermionic DM decay and the pulsar model.

For calculating CALET expected data, a detector aperture of 1200 $\mathrm{cm}^2$ sr [218], and 5 years of data-taking with 90% reconstruction efficiency is assumed. In figure 4.8, an example of the single pulsar parametrization fit ($\chi^2/\mathrm{ndf} = 212/78$) to one of the 10000 simulated samples of 2 TeV DM is shown. The $\chi^2$ distribution obtained from this two different models (DM and single pulsar) is shown in the left panel of figure 4.10. Similarly, the process described above for 2 TeV DM case, was repeated for 1.5 TeV and 1 TeV DM models where the decay is restricted only to $\mu\mu\nu$ and $ee\nu$ channels. Example fits of the parametrization with single pulsar as extra source to a DM case sample for 1.5 TeV and 1 TeV DM are shown in figure 4.9a and figure 4.9b respectively. The corresponding $\chi^2$ distributions (obtained from fitting to 10000

generated samples) of the DM and single pulsar models are shown in figure 4.11a and figure 4.11b assuming 1.5 TeV DM and 1 TeV model respectively.

Since the DM and the single pulsar source model are non-nested, i.e. they are independent of each other, so a likelihood-ratio test statistic cannot be determined. However using Akaike's Information Criterion (AIC) [219], it is possible to assess the quality of DM and single pulsar model relative to each other and select one model over another to represent the measurements. The AIC value of a particular model is given by

$$\mathrm{AIC} = -2L_k + 2k \ , \tag{4.12}$$

where $k$ is the number of free parameters in the model and $L_k$ denotes the maximum value of the log-likelihood function. Given a set of models, the model with lowest AIC value is preferred for representing data provided that the likelihood functions for the competing models follow normal distribution. The $\chi^2$ distribution of both pulsar and DM models follow a normal distribution as can be seen from the plots (ex. left panel of figure 4.10). As pulsar cut-off energy ($E_{pn}$) is take as a free parameter in this fit of single pulsar parametrization to simulated CALET data and AMS-02 measurements, from the parameter list (table 4.1), the pulsar model has three free parameters ($\frac{C_{pn}}{C_p}$, $\gamma_p - \gamma_{pn}$, $E_{pn}$). The DM model has 3 free parameters also and these are the scale factors for the 3 decay modes. The CR background spectra has 4 free parameters (see table 4.1) and these are common for both DM and pulsar model. Now referring eq. 4.12, both models have the same number of free parameters ($k$) and the $\chi^2$ distribution for each model follows a normal distribution, so comparison of $\chi^2$ is equivalent to a comparison of the AIC value. Except for very few samples, the $\chi^2$ difference ($\chi^2_{\mathrm{pulsar}} - \chi^2_{\mathrm{DM}}$) between single pulsar source fit and the DM re-fit is always positive (as shown in the right panel of figure 4.10), which indicates that the simulated DM model is favored over the pulsar model to represent the measurements. at 95% CL as the pulsar model is excluded for most of the samples, a clear discernibility can be claimed from those cases where the DM model is allowed. The re-fit of the DM model fits well ($\chi^2 < 95\%\,\mathrm{CL}$) the measurements for all but a negligible fraction of samples as shown in table 4.3. Therefore, the exclusion of the pulsar case is sufficient to claim the discernibility.

For the 2 TeV DM model including decay to $\tau\tau\nu$, the average $\chi^2$ of the

pulsar fit decreases with increasing $E_d$. However, still a majority of samples could be excluded even at $E_d = 10$ TeV, with exact numbers given in table 4.3. The 1.5 TeV and 1 TeV DM mass cases where no decay to $\tau\tau\nu$ takes place, can be well separated from the pulsar case, independent of $E_d$.

Among the studied DM models, 1 TeV decaying DM model (decay only to $\mu\mu\nu$ and $ee\nu$) features the largest difference between the two $\chi^2$ distributions of pulsar and DM model as shown in figure 4.11b. It shows that this model of DM decay is best distinguishable from a single pulsar by the CALET $(e^+ + e^-)$ flux measurement. The branching fraction obtained from the fit of this 1 TeV DM model to the experimental results (see figure 4.7b) is 40% for the $ee\nu$ channel. High branching fraction in $ee\nu$ channel results in a sharp drop in the $(e^+ + e^-)$ flux and positron flux at half the mass of the DM (see figure 4.9b) which is a well detectable signature compared to smooth pulsar spectrum. Also low DM mass (1 TeV) and high percentage of electrons in the decay channel results in the lowest predicted $\gamma$-ray flux among the studied DM models, showing a complementarity between the sensitivity of CALET and $\gamma$-ray measurements.

| $M_{DM}$ \ $E_d$ (TeV) | 1 | 2 | 5 | 10 |
|---|---|---|---|---|
| 2 TeV | 0.27/0/0.73<br>0.23/0.53/0.24 | 0.23/0/0.77<br>0/0.98/0.02 | 0.20/0/0.80<br>0.09/0.83/0.08 | 0.20/0/0.80<br>0.07/0.86/0.07 |
| 1.5 TeV | 0.30/0/0.70<br>0.34/0.59/0.07 | 0.30/0/0.70<br>0.27/0.73/0 | 0.26/0/0.74<br>0.22/0.78/0 | 0.23/0/0.77<br>0.21/0.79/0 |
| 1 TeV | Excluded | Excluded | 0.27/0/0.73<br>0.32/0.15/0.53 | 0.26/0/0.74<br>0.40/0.60/0 |

Table 4.2: Branching ratios (in the order: $ee\nu/\mu\mu\nu/\tau\tau\nu$) from the fit to AMS-02 ($e^+ + e^-$) and positron flux for all the studied values of $M_{DM}$ and $E_d$. Upper line of each cell: branching ratios of the best fit including all the leptonic components, lower line: branching ratios of the best fit with $\tau\tau\nu$ component reduced in the decay products. Colored boxes correspond to the examples shown in figure 4.4, figure 4.7a and figure 4.7b respectively.

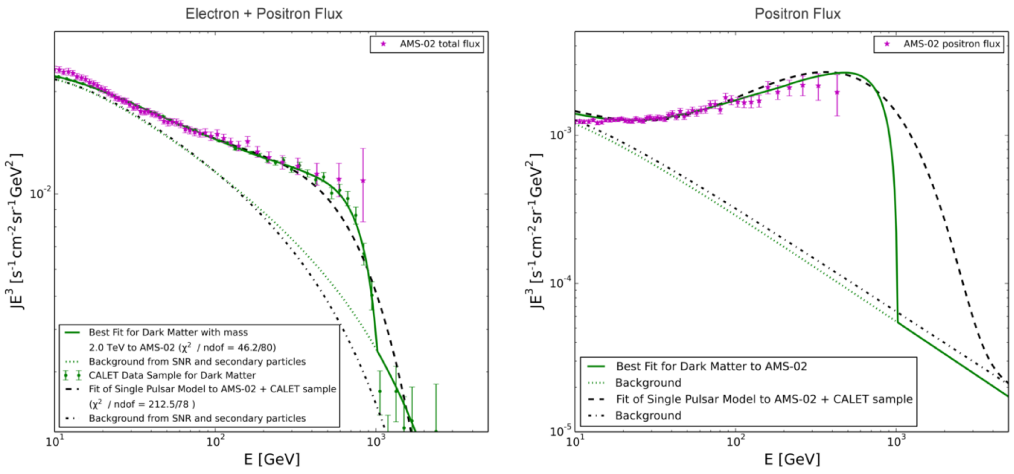


Figure 4.8: Fit of the single pulsar source to one of the simulated 10000 statistical samples of 5-year CALET data for ($e^+ + e^-$) flux (left panel) for the 2 TeV DM (green line) and positron flux (right panel) from AMS-02 data is shown here with the black dashed lines ($\chi^2$/ndf for the shown case is 212.5/78), assuming $E_d = 2$ TeV. Background CR spectra are shown as dotted lines (green and black) for the two different extra source scenarios (DM and pulsar respectively).

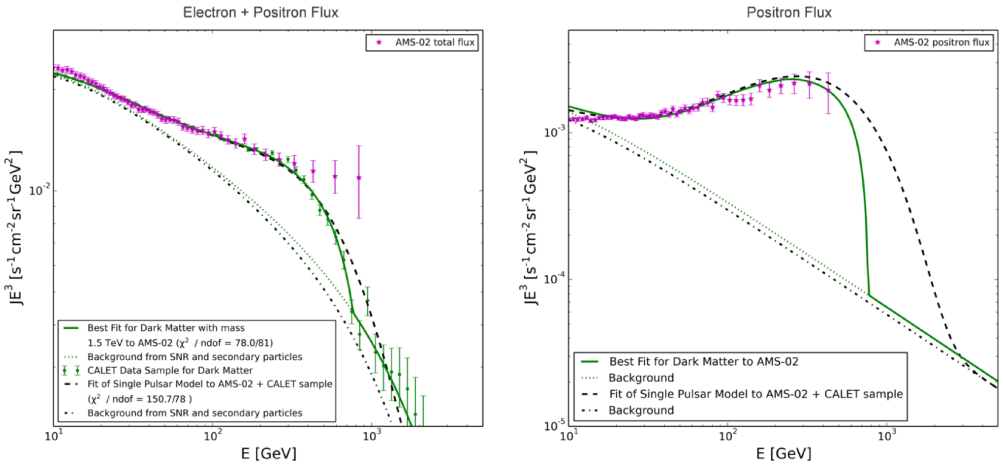


(a)

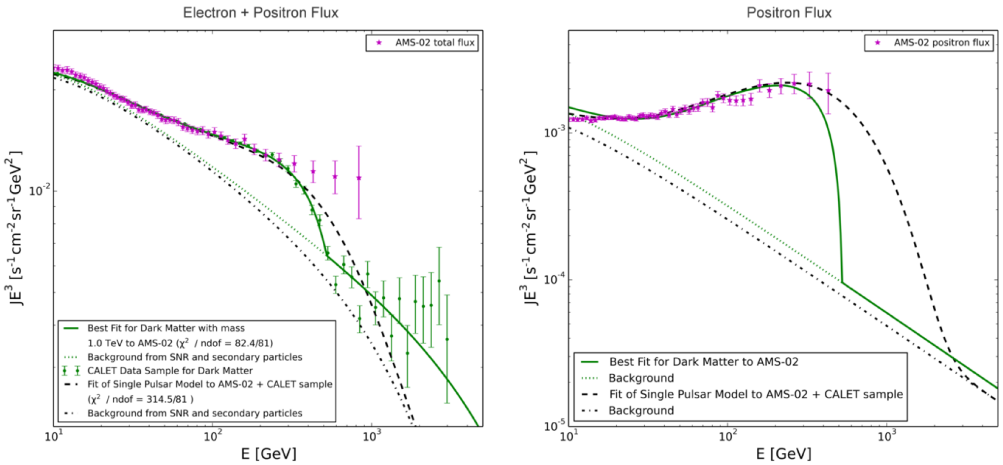


(b)

Figure 4.9: (a)As figure 4.8 but for 1.5 TeV DM without $\tau\tau\nu$ channel, assuming $E_d = 2$ TeV. (b) As figure 4.9a for 1 TeV DM without $\tau\tau\nu$ channel, assuming $E_d = 10$ TeV.

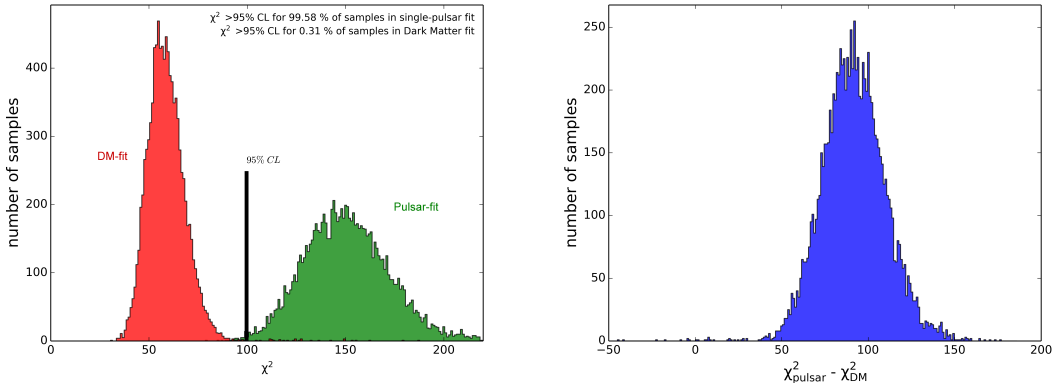


Figure 4.10: $\chi^2$ distribution for the fit of the single pulsar source to the simulated CALET data for 10000 DM samples (2 TeV DM) + AMS-02 positron flux data (green) and re-fit of DM samples using the same data points (red). On the right panel the difference between the $\chi^2$ for pulsar and DM ($\chi^2_{\text{pulsar}} - \chi^2_{\text{DM}}$) is shown (blue).

| $M_{DM}$ \ $E_d$ (TeV) | 1 | 2 | 5 | 10 |
|---|---|---|---|---|
| 2 TeV | 211.15/61.16<br>10000/13 | 150.61/58.90<br>9958/31 | 123.87/58.31<br>8932/6 | 116.19/58.29<br>7771/1 |
| 1.5 TeV | - | 142.37/75.54<br>9943/138 | 132.98/76.06<br>9632/97 | 131.46/76.59<br>10000/49 |
| 1 TeV | - | - | - | 269.85/72.87<br>10000/49 |

Table 4.3: Upper line of each cell: average $\chi^2$ obtained from the fits of the single pulsar source to the 10000 samples of simulated CALET data + positron flux from AMS-02 and the re-fit of the DM model to the same data points as a function of $M_{DM}$ and $E_d$, in the order Pulsar fit/DM fit. Lower line : number of excluded samples ($\chi^2 > 95\%$CL) for each case. Average Number Degree of Freedom (NDF) is 80. Colored boxes are the examples shown in figure 4.10, figure 4.11a, figure 4.11b respectively.

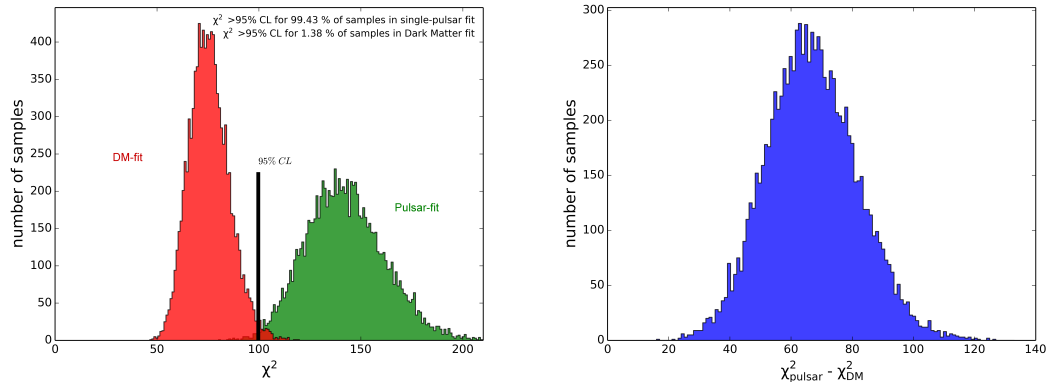


(a)

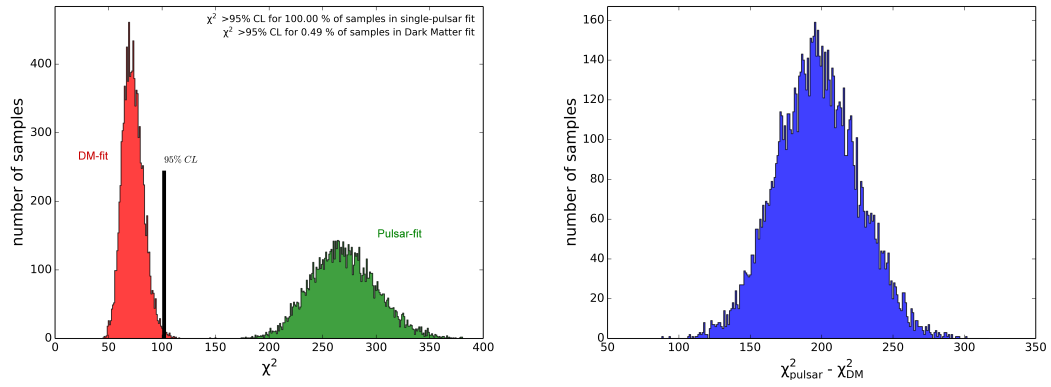


(b)

Figure 4.11: (a) As figure 4.10, but for low $\gamma$-ray model with 1.5 TeV DM decay without $\tau\tau\nu$ channel with $E_d$ set to 2 TeV. (b) As figure 4.11a, but for the low $\gamma$-ray model of the 1 TeV DM decay without $\tau\tau\nu$ channel and $E_d = 10$ TeV. Among the studied DM scenarios, 1 TeV DM decay model shows highest discernibility (higher value of $(\chi^2_{\rm pulsar} - \chi^2_{\rm DM})$ from a single pulsar case with 5 years CALET measurement. Single pulsar model in this case is completely excluded at 95% CL as shown in the figure.

# Chapter 5

# Interpretation of the $e^- + e^+$ Spectrum Measured by CALET on the ISS

## 5.1 Current Status of $e^- + e^+$ Measurement

Recent developments in Cosmic Ray measurements result in precise measurements of CR spectra and significant improvements from past experiments. For the $e^+ + e^-$ spectrum, space missions like ATIC (balloon experiment), PAMELA, Fermi-LAT, AMS-02 (space based) and ground-based experiments like H.E.S.S. Cherenkov Telescope, both provided precise measurements. The balloon experiment ATIC reported an excess in the measurement from 300 GeV to 800 GeV range [65] compared to the background expected from the homogeneous CR source distribution, which was very similar to the feature detected by PPB-BETS [220]. This excess was however not confirmed by Fermi and a steepening in the spectrum was observed by H.E.S.S. over 900 GeV. As mentioned before, due to rapid energy loss of CR electrons through synchrotron radiation and inverse Compton Scattering, observing 1 TeV electrons could act as a probe for nearby CR sources.

Precise measurements of $e^+ + e^-$ by Alpha Magnetic Spectrometer (AMS-02) was published recently and a total of $10.6 \times 10^6$ events in the energy range

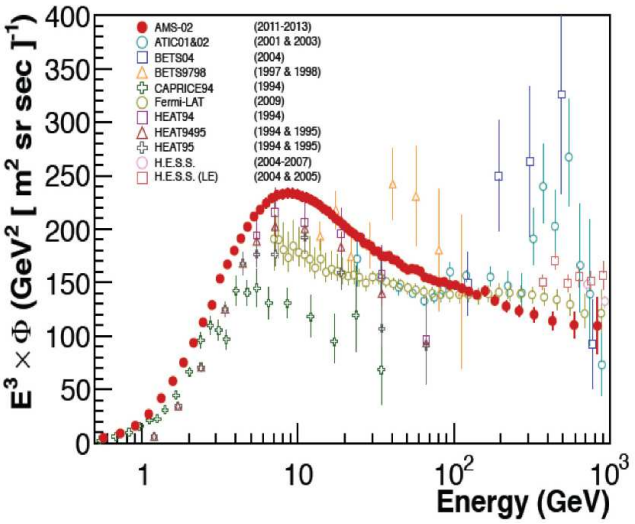


Figure 5.1: A comparison of $e^+ + e^-$ flux measured by various space-based and ground-based CR detectors is shown here. Figure ref. [221]

0.5 GeV to 1 TeV from May 2011 to November 2013 was analyzed. A single power law with spectral index $\gamma = -3.170 \pm 0.008 \pm 0.008$ can explain the measurements from 30 GeV to 1 TeV indicating that the spectra is featureless and smooth [162]. However, the electron flux and positron flux measured by AMS-02 [64] shows spectral hardening for both positron (spectral index changing from $-2.97 \pm 0.03$ to $-2.75 \pm 0.05$) and electron (spectral index changing from $-3.28 \pm 0.03$ to $-3.15 \pm 0.04$) spectrum. The results from various CR measurements including the AMS-02 measurements are shown in figure 5.1 [221]. In figure 5.2 featureless and smooth behavior of $e^+ + e^-$ flux measured by AMS-02 is shown where in the upper panel variation of spectral index with energy is shown and in lower panel the single power law is fitted to measurement.

## 5.2 CALET $e^- + e^+$ Flux Measurement and Result

CALET instrument was launched on August 19, 2015 from Tanegashima by H-II Transfer Vehicle (HTV) and was docked to the International Space Station on the

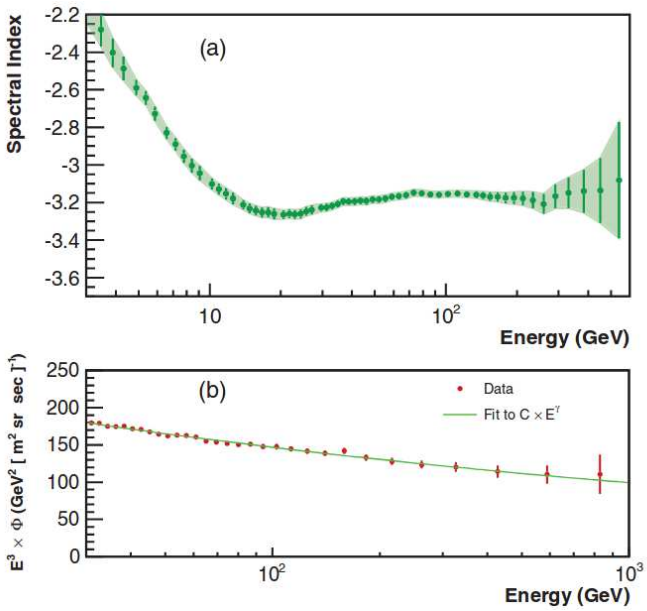


Figure 5.2: The featureless nature of AMS-02 $e^+ + e^-$ spectrum is shown here. In the upper panel spectral index of $e^+ + e^-$ flux as a function of energy is plotted and in lower panel a single power-law is fitted to AMS-02 measurement from 30 GeV to 1 TeV [162].

Japanese Experiment Module-Exposed Facility (JEM-EF). The data collection process began on October 2015. The main science goal of CALET is to perform precise measurement of the CR $e^+ + e^-$ flux measurement starting from 1 GeV to 20 TeV and shed light on nearby sources [57] and CR escape mechanism from SNRs [222]. CALET detector description and science goals are described in section 1.6.

CALET data collected from October 2015 to June 2017 over a period of 627 days are published recently in here [45] and the energy spectrum is shown in figure 5.3. Through careful calibration of each TASC readout channel, a fine energy resolution ($\sim 2\%$) is obtained for both electrons and $\gamma$-rays, especially over 100 GeV [51]. The detector performance was checked using Monte-Carlo simulations and the validity of simulations are confirmed using CERN-SPS beam test data [223, 224]. As hadronic showers are widely spread compared to electrons and $\gamma$-rays, this advantage was used to develop a track recognition algorithm. Also $3\,X_0$ of thick IMC ensures that electromagnetic shower develops properly inside the detector. Including $27\,X_0$ of TASC, the total thickness of the calorimeter is $30\,X_0$ and particle identification information from the calorimeter achieved an electron

detection efficiency above 80% and a proton rejection power of $\sim 10^5$. The $e^- + e^+$ spectrum shown in figure 5.3 for an energy range starting from 10 GeV to 3 TeV as measured by CALET and only the events which are fully contained inside the calorimeter are considered. Acceptance of the detector is $570\,\mathrm{cm}^2\,\mathrm{sr}$, which is 55% of the full acceptance of the detector ($\sim 1040\,\mathrm{cm}^2\,\mathrm{sr}$). The systematic error which includes the uncertainties in energy scale, geometrical acceptance, long-term stability, electron identification etc. are shown as the grey band. It was also reported here [45] that the spectrum above 30 GeV could be fitted to a single power-law with spectral index $-3.152 \pm 0.016$. It is important to note here that the CALET measurement is fairly consistent with AMS-02 $e^- + e^+$ flux measurement where the measurement can be represented by single power-law from 30 GeV to 1 TeV with spectral index $\approx -3.170$ [162].

As already discussed in section 4.1, that one of the important features of recent charged CR measurement is the observation of positron excess which requires extra sources (like pulsar or DM decay and annihilation) producing electron-positron pairs to account for the excess. In the light of CALET measurement we investigate the type of the extra source that can explain the data. To do this we perform a combined analysis of $e^- + e^+$ and $e^+$ data and test decaying DM and pulsar models separately. Starting from a single power law, which was introduced in eq. 4.8, we test several background parametrization to correctly represent the combined measurement under 95% CL. This is indeed necessary for an unbiased study of the possible extra source contributions the the measured data. As the spectral index change as observed by AMS-02 in electron and positron spectrum separately, we assumed a smoothly broken power-law for electron spectrum parametrization to describe the combined CALET $e^- + e^+$ flux and AMS-02 $e^+$ flux over a wide energy range (10 GeV to 3 TeV). This parametrization is fitted to $e^- + e^+$ and $e^+$ data and we found that depending on the choice of parameters in the parametrization, both DM and pulsar model can explain the combined measurements. Setting up a confidence level (CL) of 95% allowed range of DM mass and pulsar cut-off energies are derived. These analysis method and results are described in detail in the next sections. It is necessary to note that during our analysis of CALET data and preparation of the thesis, DAMPE (DArk Matter Particle Explorer) also published their measurement [48] of $e^- + e^+$ flux, so we could not perform a comparative analysis

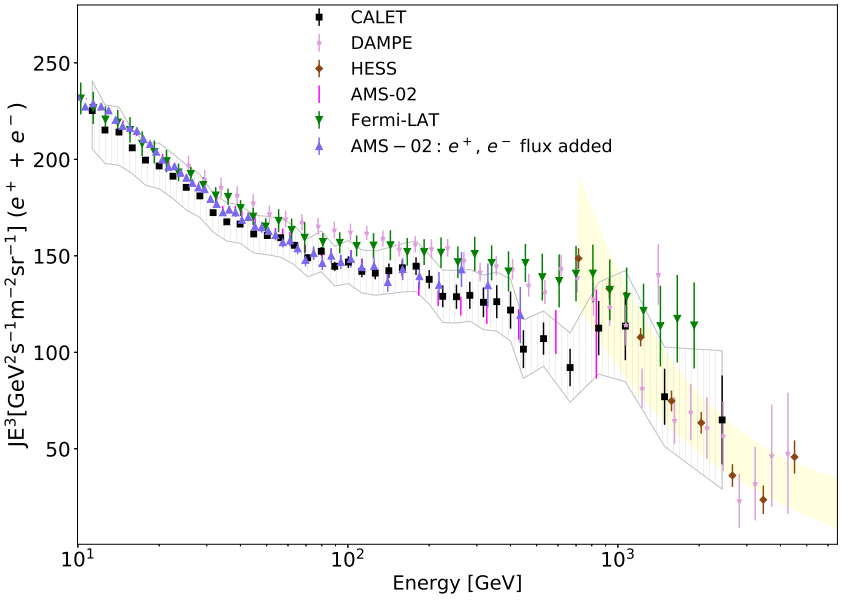


Figure 5.3: $e^+ + e^-$ Flux measured by CALET [45] is shown with red error-bars and compared with other space-based and ground-based measurements. The white and yellow band represents the uncertainty in systematics (energy scale uncertainty is not included) of CALET and HESS measurements respectively.

of DAMPE data. Since we used a combined analysis of CALET $e^- + e^+$ data and AMS-02 $e^+$ data, the inconsistency between DAMPE and AMS-02 measurements makes it difficult to perform a consistent analysis.

## 5.3 Parametrization of the Observed $e^+$ and $e^-$ Spectrum

### 5.3.1 Single Power-law Parametrization

Before the fitting procedures to data and analysis related to it are described in detail, it is necessary to highlight that the systematic errors of CALET measurement are not taken into account. This is due to clearly determine the contribution

from DM and pulsar to the electron/positron measurements to set the allowed range of DM mass and pulsar cut-off energies, which are not possible with systematics included. Also, a significant amount of systematics is coming from the uncertainties in the flux normalization, which does not affect the spectral feature study considerably. Before the combined analysis of CALET and AMS-02 data was performed, CALET measurement only was checked with a single power law with exponential cut-off ($\phi = CE^{-\gamma}\, e^{-\frac{E}{E_d}}$) for three different values of solar modulation potential (0.4 GV, 0.5 GV, 0.6 GV) and it was confirmed that the measured flux from 10 GeV to 3 TeV cannot be represented by this simple parametrization. With this parametrization the best fit to CALET measurement can be found for a solar modulation potential of 400 MeV and $E_d = 10$ TeV, resulting a very poor $\chi^2$/n.d.f. which is shown in figure 5.4. Here it is important to note that we consider data points from 10 GeV to 3 TeV for the combined analysis of CALET $e^- + e^+$ flux and AMS-02 $e^+$ flux as the energy bounds are coming from the CALET measurement, which is [10 GeV, 3 TeV]. The total number of data points are 83 where there are 39 data points from 10 GeV to 3 TeV for CALET measurement, and 44 data points for AMS-02 $e^+$ flux from 10 GeV to $\sim$ 700 GeV.

To study the combined measurement of CALET $e^- + e^+$ flux and AMS-02 $e^+$ flux, the minimal model proposed by AMS-02 [8, 165] to explain the rise in positron fraction is investigated. In this model the electron and positron spectrum are considered as combination of sum of diffuse power-law spectrum ($CE^{-\gamma}$) and a single common source ($C_s\, E^{-\gamma_s}\, e^{-\frac{E}{E_d}}$). With this assumption the total $e^- + e^+$ spectrum can be written as described in eq. 4.8. Using this parametrization, after testing a wide range of cut-off energies for the diffuse spectrum and solar modulation potential, no case with $\chi^2$ below 95% CL was found. The best-fit plot is shown in figure 5.5, where the background cut-off energy is fixed at 5 TeV and solar modulation potential at 300 MeV, resulting in a total $\chi^2$/n.d.f. of $\sim$ 312/73.

### 5.3.2 Smoothly Broken Power-law Parametrization

As the single power-law model used in section 4.4, failed to represent the combined measurement of CALET and AMS-02 data at 95% CL, a smoothly broken power-law is introduced to correctly reflect the variability caused by unknown parameters

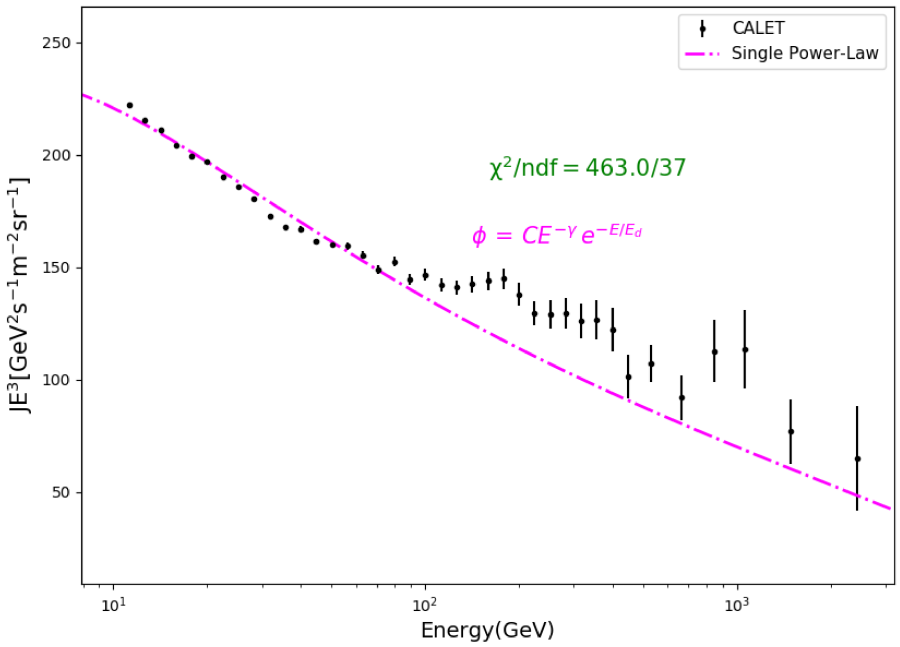


Figure 5.4: Single power law fit to CALET data.

of injection and propagation. This is necessary for a true representation of possible extra source contributions, such as electron-positron pairs from DM (annihilation or decay) or pulsar in the observed spectrum. To correctly represent the CALET measurement over the wide energy range (10 GeV-3 TeV), a smoothly broken power-law spectrum is introduced as shown in eq. 5.1.

$$\phi_{e^-} = C_{e^-} E^{\gamma_{e^-} - \Delta\gamma_{e^-}} \left(1 + \left(\frac{E}{E_g}\right)^{\frac{\Delta\gamma_{e^-}}{s}}\right)^{s} \left(\frac{C_s}{C_{e^-}} E^{-\gamma_{e^-}+\gamma_s} + e^{-E/E_d}\right) + \phi_{\text{extra}} \ , \tag{5.1}$$

where $C_{e^-}$, $\frac{C_s}{C_{e^-}}$ are the absolute normalization of the primary $e^-$ flux and the ratio of absolute normalization of secondary to primary flux. $\Delta\gamma_{e^-}$ is the difference in the spectral index before and after the break, and $E_g$ is the location of the spectral break for primary electrons. The transition of the spectral index change is either over a wide or narrow energy range is described by the dimensionless parameter $s$, known as smoothness, with higher values of $s$ representing a wider energy range and thus a relatively smoother break in the spectrum. An example of the dependence of energy-break term $\left(1 + \left(\frac{E}{E_g}\right)^{\frac{\delta\gamma_e}{s}}\right)^{s}$ on different values of $s$ are shown in figure 5.6.

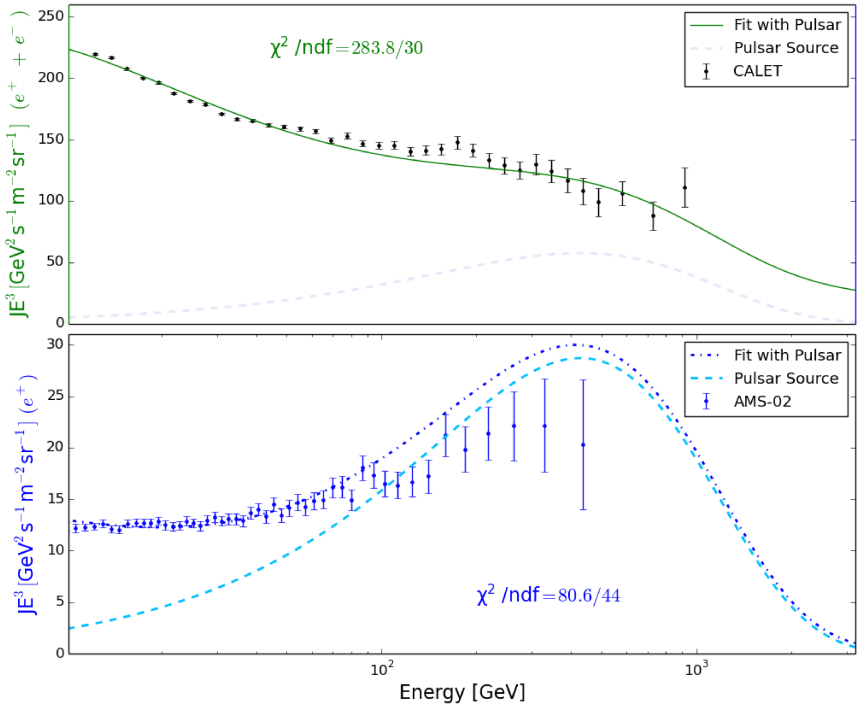


Figure 5.5: Single power law with cut off and pulsar source as extra source producing electron-positron pairs is taken as a test model to explain the $e^+ + e^-$ flux (CALET) and $e^+$ flux (AMS-02) measurements.

For $s \to 0$, i.e. in case of a hard-break the the electron parametrization changes as

$$\begin{aligned}
\phi_{e^-} &= C_{e^-} E^{\gamma_{e^-} - \Delta\gamma_{e^-}} \left( \frac{C_s}{C_{e^-}} E^{-\gamma_{e^-} + \gamma_s} + e^{-E/E_d} \right) + \phi_{\text{extra}} \,; \text{for } E < E_g; \\
\phi_{e^-} &= \left( \frac{E}{E_g} \right)^{\gamma_{e^-}} E_g^{-\gamma_{e^-} - \delta\gamma_{e^-}} \left( \frac{C_s}{C_{e^-}} E^{-\gamma_{e^-} + \gamma_s} + e^{-E/E_d} \right) + \phi_{\text{extra}} \,; \text{for } E > E_g \,.
\end{aligned} \tag{5.2}$$

For $s \to 1$, the parametrization represents addition of an electron-only power-law component. So, this broken power-law parametrization at the two limiting values of $s(0, 1)$, represents a hard break coming from injection and propagation, as well as contribution from nearby SNRs. As before in eq 4.8, radiative energy losses such as synchrotron or inverse Compton scattering for primary electrons are modeled as an exponential cut-off in energy with $E_d$ denoting the value of cut-off energy. $E_d$ also represents the contribution from nearby sources and effect of spiral-arm thickness on CR propagation. To study the effect of this background cut-off energy several values are tested between 1 TeV to 10 TeV and the results for 2 TeV and 10 TeV are shown here. For the difference in the spectral indices of primary and secondary ($\gamma_{e^-} - \gamma_s = -\delta$), which is fixed to 0.4, as described in table 4.1.

The positron flux is given by

$$\phi_{e^+} = C_{e^-} E^{\gamma_{e^-}} \left( \frac{C_s}{C_{e^-}} E^{-\gamma_{e^-} + \gamma_s} \right) + \phi_{\text{extra}} \quad , \tag{5.3}$$

where $\phi_{\text{extra}}$ is the flux of electron-positron pairs from either DM decay or pulsar source.

## 5.4 Explaining CALET Measurement with Dark Matter Decay or Single Pulsar

### 5.4.1 Explaining CALET Measurement with Dark Matter Decay

Considering recent astrophysical and CR measurements, as described previously in details (see section 4.2), 3-body leptonic decay of DM is preferable over other DM

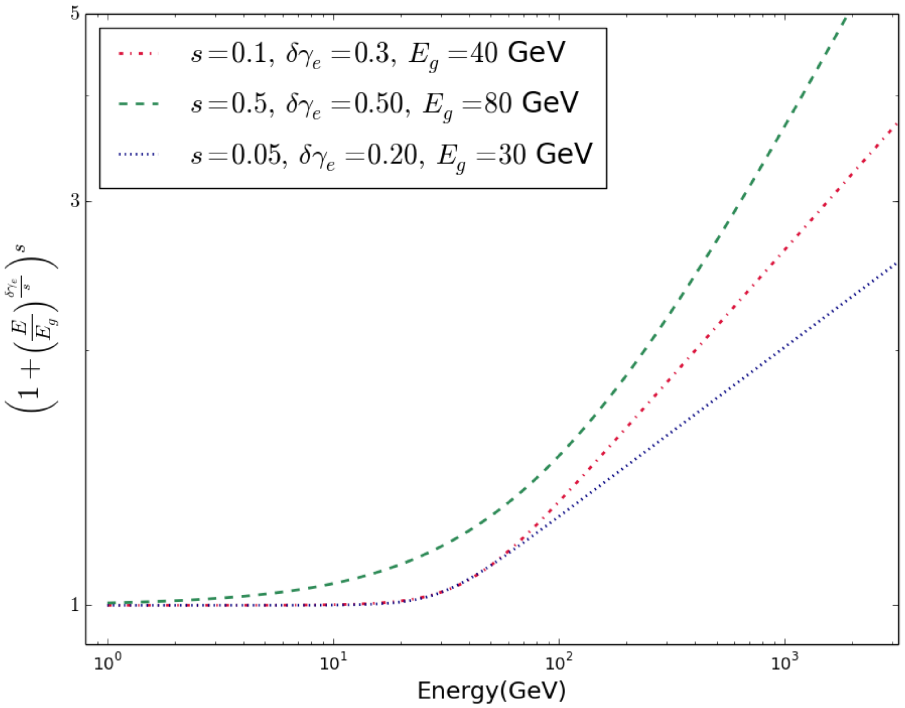


Figure 5.6: Dependence of energy-break term on different values of smoothness ($s$) are shown here. Higher value of smoothness ($s = 0.5$) shows a relatively smoother variation (green line) with energy, compared to the lower value of $s = 0.05$ (blue line).

decay or annihilation scenario to explain the positron excess. DM decaying to 3 leptons ($DM \rightarrow l^+l^-\nu$) is taken as a test model to explain the combined CALET measurement of $e^+ + e^-$ flux and AMS-02 $e^+$ flux. For a fixed value of DM mass it was shown in section 4.6, that decay excluding the $\tau\tau\nu$ channel can reduce $\gamma$-ray flux considerably. So from now while comparing recent measurements with DM decay as extra source, $\tau\tau\nu$ channel is not considered. For the 3-body DM decay scenario, following the procedure as described in section 4.3, the CR $e^+$ ($e^-$) flux is calculated using GALPROP.

Now considering this DM decay as the extra source in the equations for the parametrization of electron and positron flux (eq. 5.1, eq. 5.3), a combined fit to the CALET $e^+ + e^-$ spectrum and the AMS-02 $e^+$ spectrum is performed, to determine the best fit parameters. AMS-02 measurements below 10 GeV are neglected in this fitting, as solar modulation strongly influences the charged CR spectrum at this low energy range. Also, CALET and AMS-02 data sets were taken during different periods of the solar cycle and if the effect of solar modulation on electron and positron are modeled differently below 10 GeV [213] then several new free parameters need to be introduced in the parametrization. Solar modulation potential above 10 GeV is charge independent and assuming force field approximation(eq. 1.23) with a common modulation potential ($\phi$) for $e^-$ and $e^+$, several fixed values are studied (0.4 GV, 0.5 GV, 0.6 GV). The $\chi^2$ value depends on the smoothness term ($s$), for which several fixed values from 0 to 1 were used. The effect of background cut-off energy ($E_d$) were also tested and the results are shown for $E_d = 10$ TeV and $E_d = 2$ TeV.

To determine the allowed range of DM mass based on the combined $\chi^2$ of the fit to CALET $e^+ + e^-$ and AMS-02 $e^+$ spectrum several fixed values in the range 600 GeV–4 TeV were tested to the 95% CL threshold. In figure 5.7, the goodness of fit as a function of the DM mass are shown for $E_d = 10$ TeV and $E_d = 2$ TeV respectively. The shaded region shows the range of $\chi^2$ values obtained with different $s$ for each DM mass, for a fixed value of the solar modulation potential ($\phi$). However, the $\chi^2$ curves are hardly influenced by the choice of solar modulation potential $\phi$. It is also shown in these figures that for both the studied cases with two different values of $E_d$, the allowed range of DM mass at 95% CL is nearly the same. For a DM mass of 1.1 TeV the best $\chi^2$ value of 75.8 with 73 degrees of

freedom is obtained (figure 5.8) with fixed values of $s = 1.0$ and $\phi = 0.5$ GV. Other fit parameters obtained from this fitting are given in Table 5.1). From now onward this model is denoted as DM Model A.

It is important here to note that there's a sudden decrease in branching ratio of electrons around the DM mass ranging from 720 GeV to 800 GeV which was plotted in the lower panel of figure 5.7. High branching fraction in the electron channel ($ee\nu$) channel results in a sharp drop around half the mass of DM and the $e^+ + e^-$ spectrum as measured by CALET features a drop around 400 GeV. The decay of DM with mass $\sim$ 800 GeV and a high branching fraction for the electron channel indeed reduces the $\chi^2$ compared to lower masses (see figure 5.9). This makes the 800 GeV DM an interesting case to study. From the fitting with increasing DM mass, $\mu\mu\nu$ channel contribution increases and results in a relatively smoother spectrum which also models the spectrum well as depicted by the further decreasing $\chi^2$ values up to 1.1 TeV. The best fit case with a mass of 1.1 TeV is shown in figure 5.8, with branching ratios of 46% for the $ee\nu$ channel and 54% for the $\mu\mu\nu$ channel, with the lifetime of the DM being $3.03 \times 10^{26}$ s.

For 800 GeV DM, branching ratio obtained from the lest $\chi^2$ case are 89% $ee\nu$ and 11% $\mu\mu\nu$ with $E_d = 10$ TeV and this case is denoted by DM Model B. Similarly, with $E_d = 2$ TeV, for 800 GeV DM, the branching ratio obtained is 100% $ee\nu$. This case is denoted by DM Model C and the fit plot is shown in figure 5.10.

As mentioned before the systematic errors can be compensated by the normalization and power-law index parameters of the parametrization, the fitting procedure was repeated including the systematics of CALET measurement. Including the systematic errors, the obtained fit parameters for the DM models are listed in Table 5.1, showing that there is no significant shift from those without systematic errors.

| **Model** DM | $C_{e^-}$ $\left(\frac{\text{GeV}}{\text{s m}^2 \text{ sr}}\right)$ | $\frac{C_s}{C_{e^-}}$ | $\gamma_{e^-}$ | $\Delta\gamma_{e^-}$ | $E_g$ GeV | $s$ | $\tau$ $_{\times 10^{26}\text{ s}}$ | $BR_{el}$ | $BR_{\mu}$ | $\chi^2$ |
|---|---|---|---|---|---|---|---|---|---|---|
| Model A | 859 | 0.034 | 2.90 | 0.681 | 87.6 | 1.0 | 3.03 | 0.46 | 0.54 | 74.49 |
| $M = 1.1$ TeV | | | | | | | | | | |
| $E_d = 10$ TeV | 863 | 0.036 | 2.91 | 0.679 | 87.6 | 1.0 | 3.04 | 0.47 | 0.53 | 29.83 |
| Model B | 846 | 0.031 | 2.84 | 0.713 | 115.3 | 1.0 | 5.85 | 0.89 | 0.11 | 80.43 |
| $M = 0.8$ TeV | | | | | | | | | | |
| $E_d = 10$ TeV | 856 | 0.031 | 2.84 | 0.72 | 115.3 | 1.0 | 6.13 | 0.94 | 0.06 | 35.21 |
| Model C | 835 | 0.027 | 2.78 | 0.725 | 107.1 | 0.75 | 7.40 | 1.0 | 0.0 | 82.50 |
| $M = 0.8$ TeV | | | | | | | | | | |
| $E_d = 2$ TeV | 838 | 0.027 | 2.79 | 0.723 | 106.9 | 0.75 | 7.25 | 1.0 | 0.0 | 37.02 |

Table 5.1: Obtained Fit parameters from the best fit of various DM decay models as extra source to the $e^+ + e^-$ (CALET) and $e^+$ (AMS-02) spectra along with the fixed parameters are listed here. Values obtained without (with) including systematic error of CALET data are shown in each cell in the upper (lower) line.

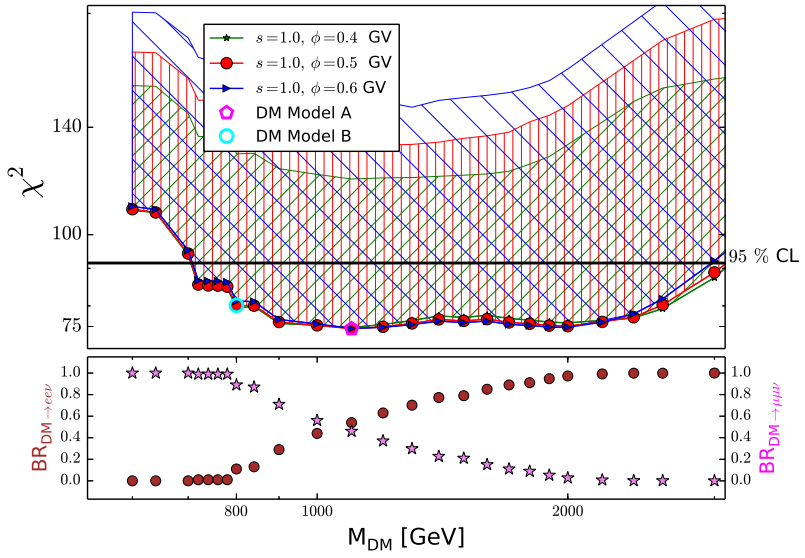


(a)

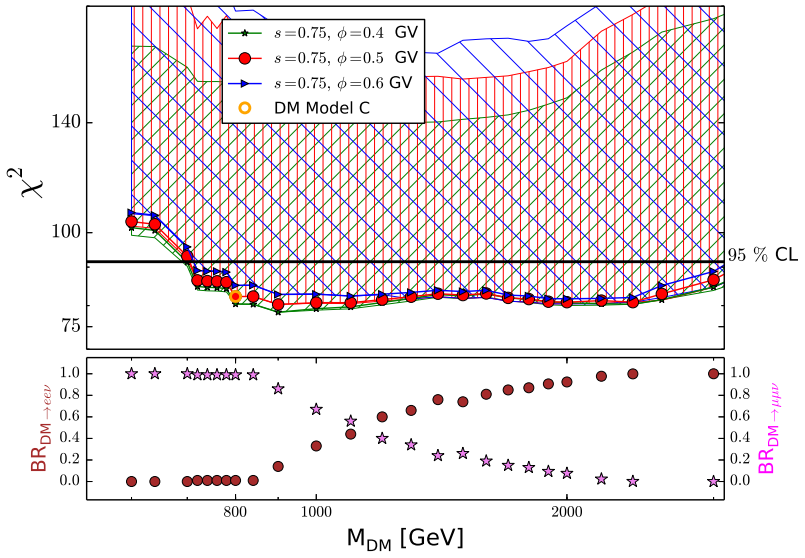


(b)

Figure 5.7: Figure (a): Upper panel shows the dependence of minimum $\chi^2$ obtained from the combined fit to the $e^+ + e^-$ flux (CALET) and $e^+$ flux (AMS-02) for fixed values of $s = 0.5$, $\phi = 0.5$ GV (green line) with $E_d = 10$ TeV, on the DM mass. Red line and blue line represent solar modulation potential $\phi = 0.4$ GV and $\phi = 0.6$ GV respectively. Shaded regions depict the minimum $\chi^2$ obtained using different values of smoothness ($s$) for a ($\phi$) = 0.5 GV (green), $\phi = 0.4$ GV (red) and $\phi = 0.6$ GV (blue). Lower panel shows the variation of branching ratios for $DM \to ee\nu$ channel (brown circles) and $DM \to \mu\mu\nu$ (pink stars) with DM mass for $s = 0.5$, $\phi = 0.5$ GV. Figure (b): Same as figure (a) but now the background cut-off energy $E_d$ is set to 2 TeV.

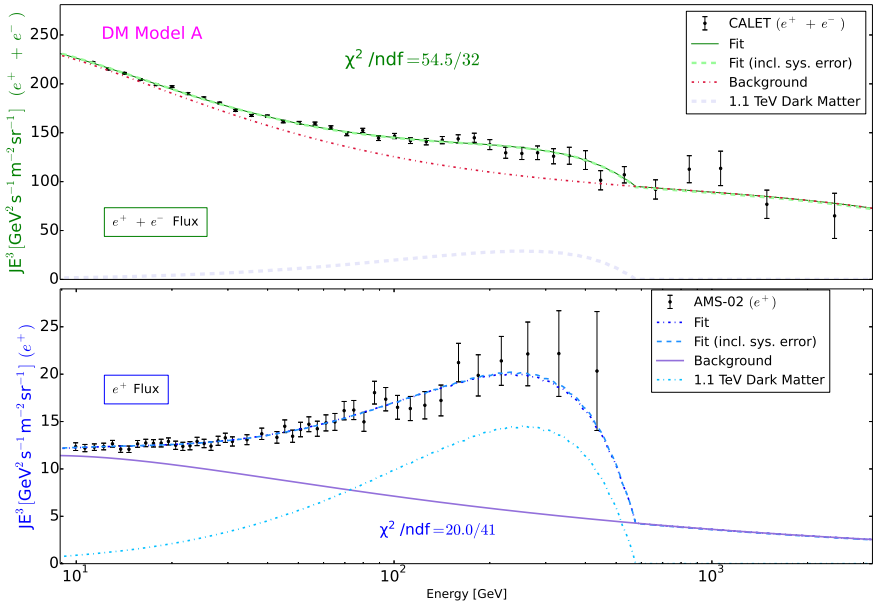


Figure 5.8: Broken power law (eq. 5.1) with decaying DM as extra source providing electron-positron pairs is taken as a test model (green line) to describe $e^+ + e^-$ spectrum measured by CALET in the upper panel and $e^+$ flux measured by AMS-02 (black error bars) in the lower panel. The red-dotted line represents the background $e^+ + e^-$ spectrum. Grey dashed lines in upper panel and blue dotted lines in lower panel show the contribution from the DM to the $e^+ + e^-$ and $e^+$ spectrum respectively. Best fit obtained including systematic error are presented with green and blue dashed lines respectively in the upper and lower panels. For a DM of mass 1.1 TeV the branching ratio and lifetime obtained from the best fit are 65% $\mu\mu\nu$, 35% $ee\nu$ and $2.44 \times 10^{26}$ s respectively. Break energy, smoothness and solar modulation potential are kept fixed at 95 GeV, 0.5 and 0.5 GV respectively.

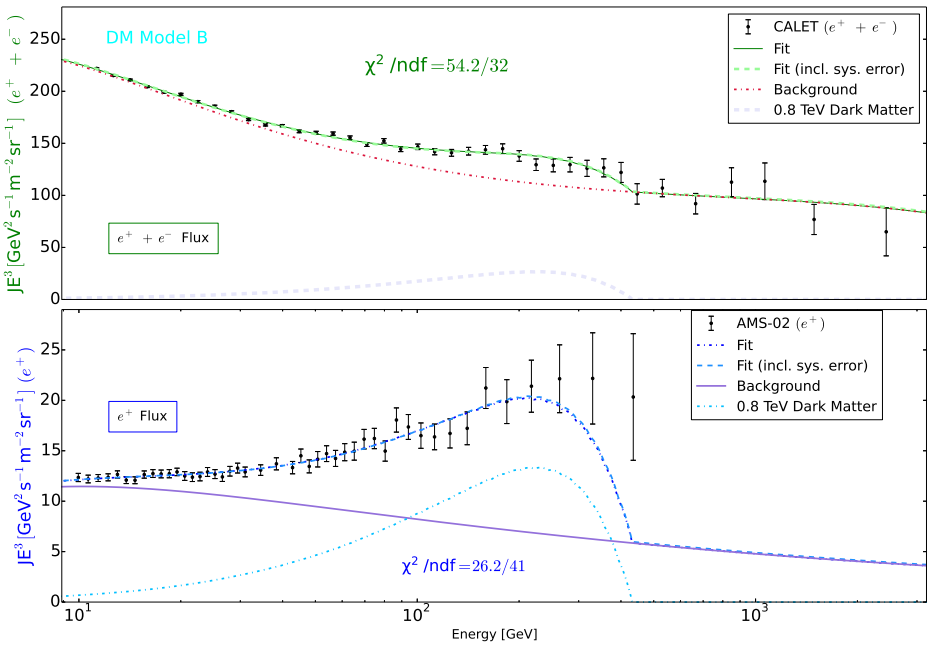


Figure 5.9: Same as figure 5.8, but now the best fit plots are shown for DM Model B. From the best fit to combined $e^+ + e^-$ flux and $e^+$ flux, the branching ratio converges to 11% to $\mu\mu\nu$ and 89% to $ee\nu$ channel with a lifetime of $5.85 \times 10^{26}$ s. Smoothness and solar modulation potential are kept fixed at 1.0 and 0.5 GV respectively.

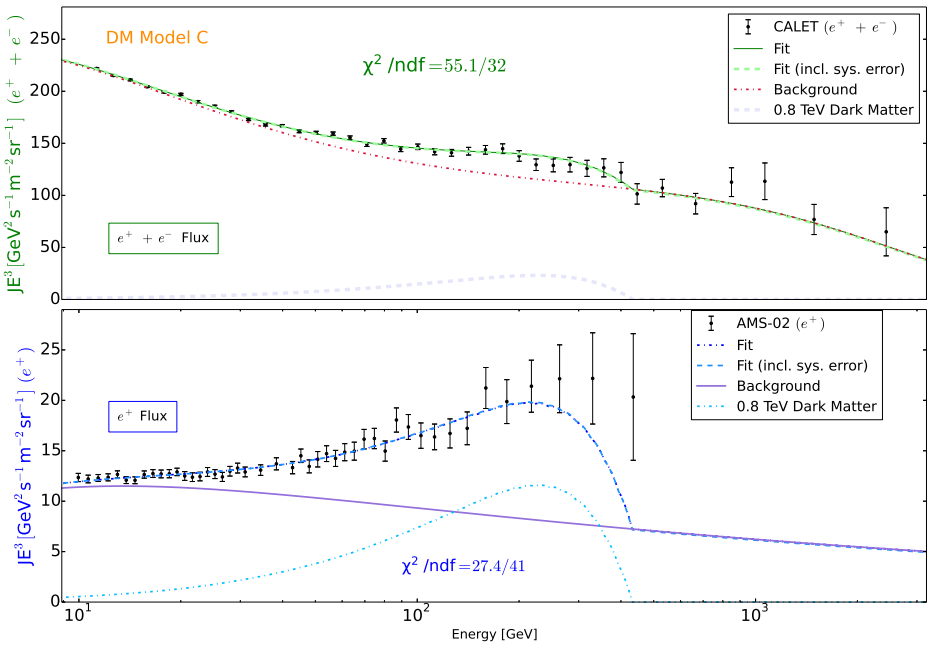


Figure 5.10: Same as figure 5.9, but now the best fit plots are shown for DM Model C. From the best fit to combined $e^+ + e^-$ flux and $e^+$ flux, the branching ratio converges to 100% to $ee\nu$ channel with a lifetime of $7.40 \times 10^{26}$ s. Smoothness and solar modulation potential are kept fixed at 0.75 and 0.5 GV respectively.

### 5.4.2 Diffuse $\gamma$-ray Constraint and Allowed Dark Matter Model

Decay of DM particles in the galactic halo would contribute to the diffuse $\gamma$-ray flux via Final State Radiation (FSR) and secondary $\gamma$-rays via Inverse Compton and Bremsstrahlung processes, as the charged decay products interact with the ISM. $\gamma$-ray flux from the 3-body decay of a DM calculated including primary and secondary production processes and it is described before in detail (section 4.6). For the DM Model A, the $\gamma$-ray flux is plotted in figure 5.11. $\gamma$-ray flux from all the studied DM models are compatible with Fermi-LAT measurement. For DM Model C, where the branching ratio for $ee\nu$ channel is 100%, the $\gamma$-ray flux is the least. In the previous $\gamma$-ray flux from DM decay plot (fig. **??**), the lowest $\gamma$-ray flux was obtained for 1 TeV DM case. Here as the allowed range of DM masses are studied using the precise measurement of CALET and AMS-02, and the the $\gamma$-ray flux from 800 GeV DM with a background cut-off energy of $E_d = 2$ TeV can be reduced further compared to the previous best scenario obtained using comparing with AMS-02 total flux and positron flux measurements. Also the extra-galactic $\gamma$-ray flux from the DM decay can contribute to the IGRB flux and the contribution is checked considering only primary flux, since the secondary flux from the inverse compton scattering off the CMB photons due to electron-positron pair is negligible. The primary extra-galactic $\gamma$-ray flux is calculated as given in this Ref. [195],

$$E_\gamma^2 \phi_\gamma^{\rm DM} = 1.4 \times 10^{-7} {\rm GeV\,cm^{-2}\,s^{-1}\,sr^{-1}} \left(\frac{1{\rm TeV}}{m_{\rm DM}}\right) \left(\frac{10^{27}{\rm s}}{\tau_{DM}}\right) \left(\frac{E_\gamma}{100\,{\rm GeV}}\right) \times \int_{E_\gamma}^{\infty} \frac{e^{-\tau_{\rm od}} \frac{dN}{dE'_\gamma}}{\sqrt{\Omega_\Lambda + \Omega_m (E'_\gamma/E_\gamma)^3}} dE'_\gamma \ , \tag{5.4}$$

where to study the most conservative case, a completely transparent universe ($\tau_{\rm od} = 0$) is assumed. The dark energy and matter density are taken from the PLANCK measurement [82], 0.685 and 0.315 respectively. The $\gamma$-ray flux consisting of primary and secondary galactic and primary extra-galactic flux are shown in figure 5.11. The $\gamma$-ray flux is also compared with the Fermi-Lat result in two more ways. The minimum of total measured flux observed at high latitude $\left(|b| > 60^\circ\right)$ observed by Fermi-Lat up to 100 GeV [193] is higher than the $\gamma$-ray flux from DM decay

products as shown in the lower left panel of figure 5.11. Also $\gamma$-ray flux from the DM decay in the anti-galactic center direction is compared with the Fermi-Lat IGRB results for galactic foreground model B. This IGRB results is obtained with galactic foreground emission subtracted from the flux. The result is shown in the lower right panel of figure 5.11 and the primary galactic flux and extra-galactic flux towards anti-galactic center are found to be of the same order of magnitude below 100 GeV, consistent with the results shown in this Ref. [194].

### 5.4.3 Explaining CALET Measurement with Single Pulsar

Following eq. 4.2 and the description therein, an exponentially cut-off power-law spectrum is used to represent a single pulsar scenario. The pulsar extra source flux is determined by the normalization factor $C_{\rm pwn}$, the power-law index $\gamma_{\rm pwn}$ and the cut-off energy $E_{\rm pwn}$ [199], and can be written as

$$\phi_{\rm pwn} = C_{\rm pwn} E^{\gamma_{\rm pwn}} e^{-\left(\frac{E}{E_{\rm pwn}}\right)} \ . \tag{5.5}$$

Similar to the study of the decaying DM model, using the smoothly broken power-law for electron spectrum parametrization, several values of smoothness ($s$) and solar modulation potential ($\phi$) were tested to explain the combined measurement of CALET and AMS-02. It was found that like the decaying DM model, this single pulsar model can also explain the combined $e^+ + e^-$ flux (CALET) and $e^+$ flux (AMS-02)as the $\chi^2$ stays below 95% CL, even if the break in the primary electron spectrum is hard (eq. 5.2). This is in contrast from the DM decay scenario where even using $s = 0.05$, no values of DM mass can be found in the range (600 GeV to 4 TeV) to explain the measurements at 95 % CL for the tested fixed values of solar modulation potential, and this highlights the necessity of the smoothness term in the primary electron spectrum parametrization. The allowed values of the pulsar-cut off energies ($E_{\rm pwn}$) compared to the 95 % CL threshold from the combined fit to the CALET $e^+ + e^-$ flux and the AMS-02 $e^+$ flux are shown in figure 5.12 for $E_d = 10$ TeV and $E_d = 2$ TeV. The shaded region shows the minimum $\chi^2$ for the different value of smoothness ranging from 0 to 1, for three different values of $\phi$. Depending on the $E_d$ and solar modulation potential, pulsar cut-off energies starting from 200 to 300 GeV to the highest energy value studied (10 TeV) are found to be allowed at 95 % CL.

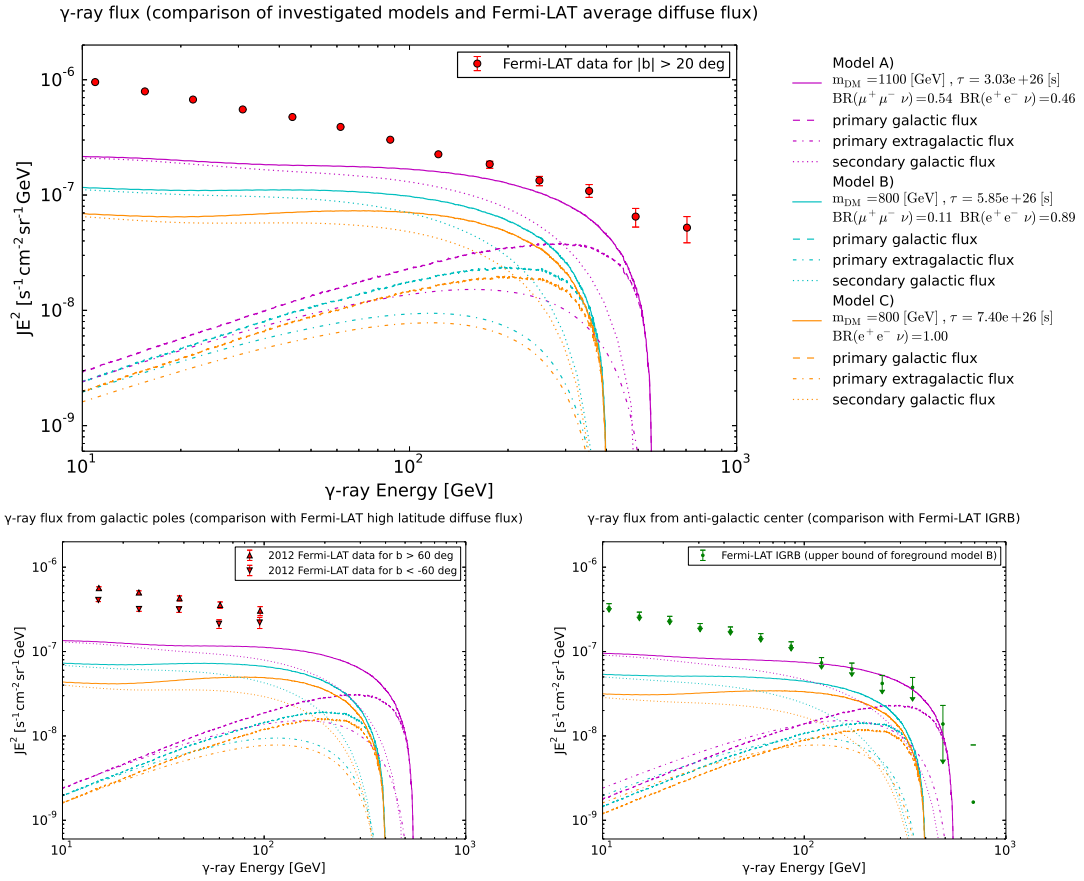


Figure 5.11: Primary and secondary $\gamma$-ray flux accompanied by DM decay to $ee\nu$ and $\mu\mu\nu$ channel for the studied models, DM Model A, DM Model B, DM Model C are shown with magenta, cyan and orange lines. The dashed lines show the primary components, dotted lines show the secondary components and the dash-dot lines represent the extra-galactic components for each DM mass. In the upper panel these results are compared with Fermi-Lat measurement away from galactic plane $|b| > 20^{\circ}$. In the lower panel on the left we compare the $\gamma$-ray flux from the DM decay with the Fermi-Lat measurement at higher latitudes $|b| > 60^{\circ}$. On the right panel $\gamma$-ray flux from the anti-galactic center is shown and compared with the Fermi-Lat IGRB measurement (for foreground model B).

As shown in figure 5.13, the best fit pulsar model is obtained for $E_{\rm pwn} = 600$ GeV with $s = 0.05, \phi = 0.5$ GV, and for a fixed value of background cut-off energy 10 TeV. Setting $E_d$ to 2 TeV, the best fit pulsar model is obtained for $E_{\rm pwn} = 2$ TeV with $s = 0.1, \phi = 0.5$ GV and this is shown in figure 5.13. Remaining characteristic fit parameter values obtained from the fit are given in Table 5.2. The exponentially cut-off pulsar spectrum is considerably different from the DM decay spectrum (figure 5.8) which shows a harder drop (hardness depend on branching fraction to $ee\nu$ channel) in the flux at an energy $\approx \frac{1}{2}\mathrm{M_{DM}}$. Based on the nature of the spectral shape of a generic pulsar spectrum and DM decay spectrum, the possibility of discerning the signatures of the pulsar spectrum from the DM decay is discussed in the next section. Instead of CALET flight data, 5 years of CALET measurement was simulated and used to study the discerning capability of CALET.

To verify that this simple power-law with exponential cut-off can represent the single young pulsar spectrum, GALPROP is used to calculate the CR $e^-(e^+)$ flux from Monogem pulsar where the distance 0.28 kpc and age $1.1 \times 10^5$ yrs are taken from ATNF catalog [201]. The same propagation parameter as shown in table 3.2, are used in consistent with the DM propagation. In GALPROP calculation, just like the calculation of electron-only flux from Vela SNR, the time progression is taken as $1.1 \times 10^4$ steps of 10 years. It is assumed that the total energy was released instantaneously at the beginning of the Monogem's life (first 10 years) and it's used in the generation of high energy CRs. The source energy spectrum is assumed as an exponentially cut-off spectrum. Several values of injection spectrum power-law index and source cut-off energy are tested and GALPROP results are scaled to match with the single pulsar parametrization (eq. 5.5). In figure 5.14, we show few results from GALPROP calculation and comparison with the single pulsar parametrization. The best match case was found with source spectral index 2.20 and source cut-off 2 TeV with total released energy as $3.24 \times 10^{47}$ erg. These values are consistent with the common theoretical models of CR acceleration from pulsars [167–169, 202, 207, 225]. In the lower panel of figure 5.14, the fractional difference of the best match case between GALPROP calculation and single pulsar parametrization are shown, which is within 10% from 10 GeV to 1 TeV and also compared to CALET experimental errors (only statistical) the difference is significantly smaller. Thus it is justified to use this single pulsar parametrization (eq. 5.5)

as a representation of a nearby single young pulsar.

Not only comparing with the numerical calculation, single pulsar parametrization is also compared with the analytic propagation calculation given in this ref. [202]. To do this, the power-law cut-off spectrum from the best fit to CALET + AMS-02 for 10 TeV cut-off is compared with the Monogem pulsar spectrum, given by the equation below (eq. 5.6).

$$\begin{aligned}\phi(r, t_{\rm diff}, E) = \frac{c}{4\pi} f = \frac{c}{4\pi} \frac{Q_0 E^{-\alpha}}{\pi^{\frac{3}{2}} r_{\rm diff}^3} \left(1 - \frac{E}{E_{\rm max}}\right)^{\alpha-2} \\ \times \exp\left[-\frac{E/E_{\rm cut}}{(1 - E/E_{\rm cut})} - \frac{d^2}{r_{\rm diff}^2}\right] ,\end{aligned} \tag{5.6}$$

where the diffusion distance, $r_{\rm diff}$, is given by

$$r_{\rm diff}(t_{\rm diff}, E) = 2\sqrt{\frac{D(E) t_{\rm diff}}{1-\delta} \frac{E_{\rm max}}{E} \left[1 - \left(1 - \frac{E}{E_{\rm max}}\right)^{1-\delta}\right]} , \tag{5.7}$$

and $E_{\rm max}$ is given by $\frac{1}{b_0 t}$, where $b_0$ is the rate of energy loss due to IC scattering and synchrotron radiation, given by $1.4 \times 10^{-16}\,{\rm GeV\,s^{-1}}$. The propagation parameters are taken in consistent with the DM propagation, and the age, distance of Monogem pulsars are taken from ATNF catalog as described before. To study the effect of confinement times in pulsar which is $<< 10^5$ years [168], different release times $t_0 - (1.1 \times 10^5 - \tau_c)$ are studied, with $t_0$ being now. The pulsar power-law index, injection spectrum cut-off and the flux scale are adapted to match the power-law with an exponential cut-off parametrization. As shown in figure 5.15, the propagated spectra for different release times match this spectrum well, considering the CALET error bar. Also, the obtained values of power-law index, cut-off energy and total released energy are compatible with the theoretical model of CR acceleration from pulsar. So, by verifying this power-law with exponential cut-off spectrum 5.5 with numerical and analytical calculation, it can be concluded that this simple parametrization can represent a single, young, nearby pulsar.

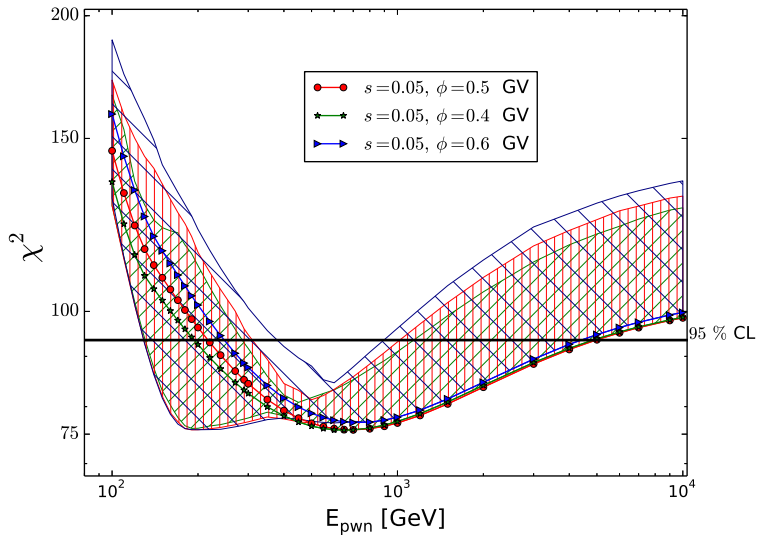


(a)

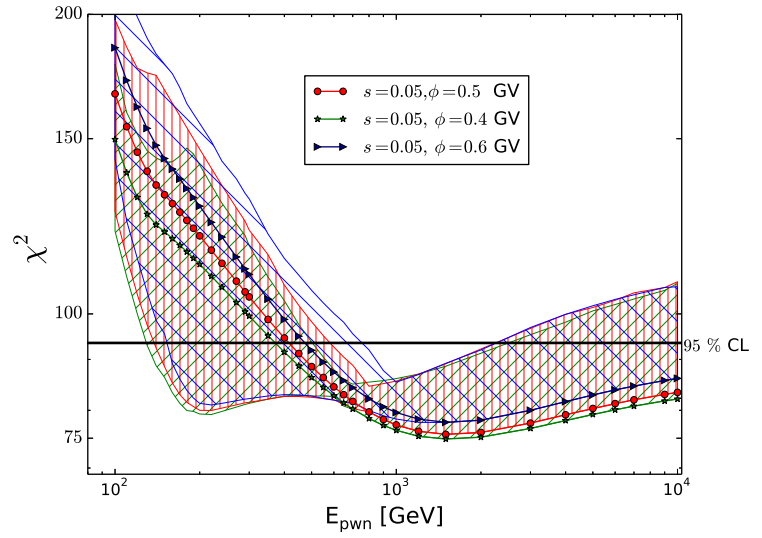


(b)

Figure 5.12: Figure (a) shows the dependence of minimium $\chi^2$ obtained from the fit to CALET and AMS-02 data on pulsar cut-off energy ($E_{pwn}$) for fixed value of $s = 0.05$ with $E_d$ set to 10 TeV. Green, red and blue line represent the minimum $\chi^2$ values obtained for $\phi = 0.4\,\text{GV}, 0.5\,\text{GV}, 0.6\,\text{GV}$ respectively. The shaded regions with the same colors show the minimum $\chi^2$ values obtained using different $s$ values for the studied values of $\phi$. Figure (b) is same as above but now the results are shown for $E_d = 2$ TeV and the minimum $\chi^2$ is obtained for $s = 0.05$.

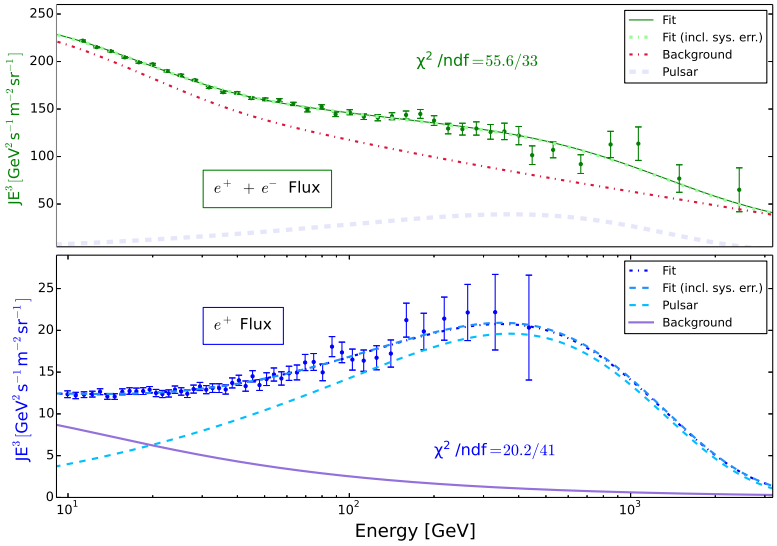


(a)

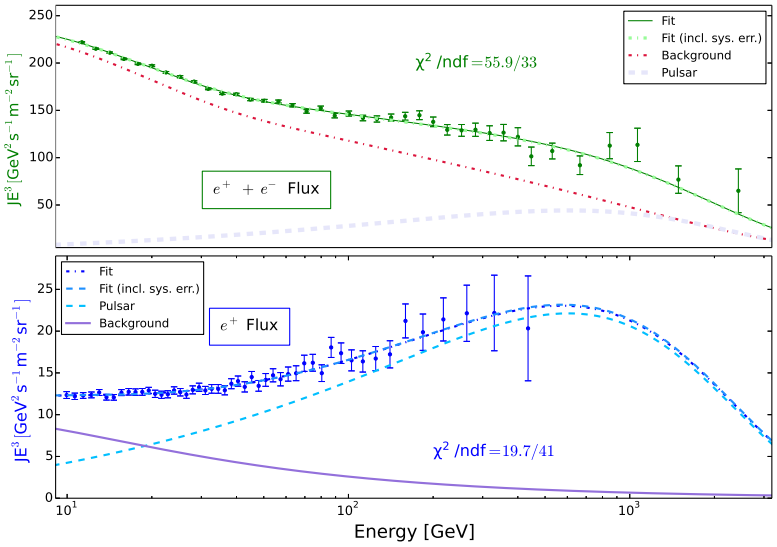


(b)

Figure 5.13: Figure (a): Broken power-law and single pulsar with exponential cut-off is taken as a test case (green line) to explain the combined CALET ($e^+ + e^-$) (upper panel) and AMS-02 ($e^+$) measurements (lower panel). Background $e^+ + e^-$ spectrum with $E_d = 10$ TeV are shown with red dotted lines. Pulsar contributions in the upper and lower panel are shown with grey and cyan dashed lines. Fit including systematic errors are shown with the dash-dotted lines. (b): Same as figure (a) but now $E_d = 2$ TeV. Fit parameters are given in table 5.2.

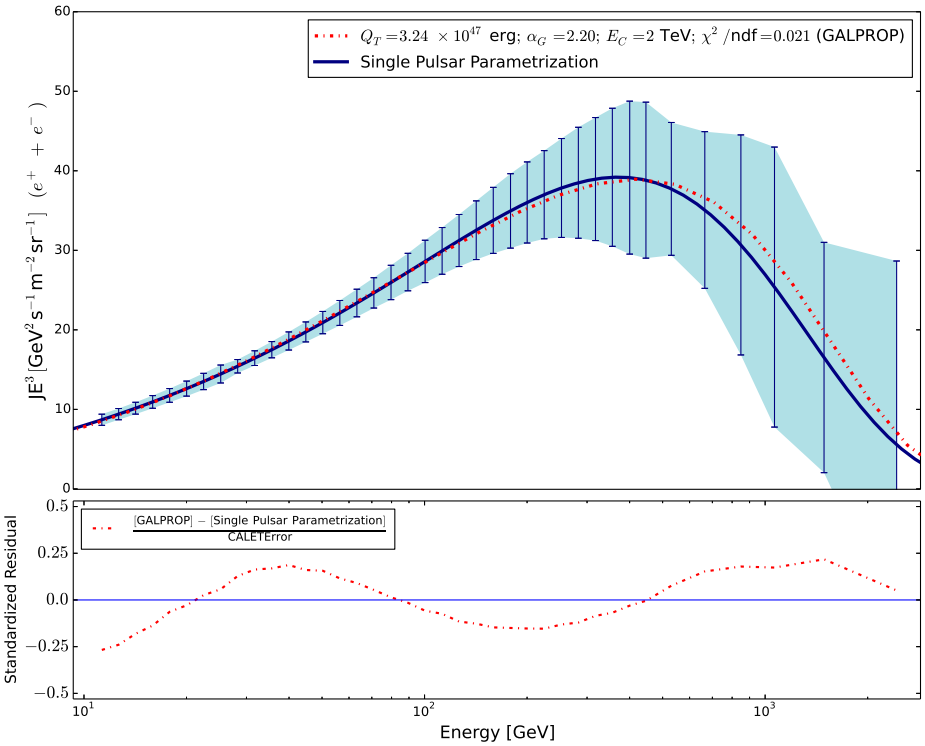


Figure 5.14: Single pulsar parametrization with values obtained for best fit to CALET + AMS-02 for $E_d$ = 10 TeV (shown in blue line), is compared with the numerical propagation calculation using GALPROP for Monogem pulsar (shown in red dotted lines). The errorbars and the shaded region represent CALET error. In the lower panel we show the fractional difference for the best match case with power-law index 2.20 and source cut-off 2 TeV from the single pulsar parametrization. The difference is within 20% for the energy range 10 GeV to 3 TeV.

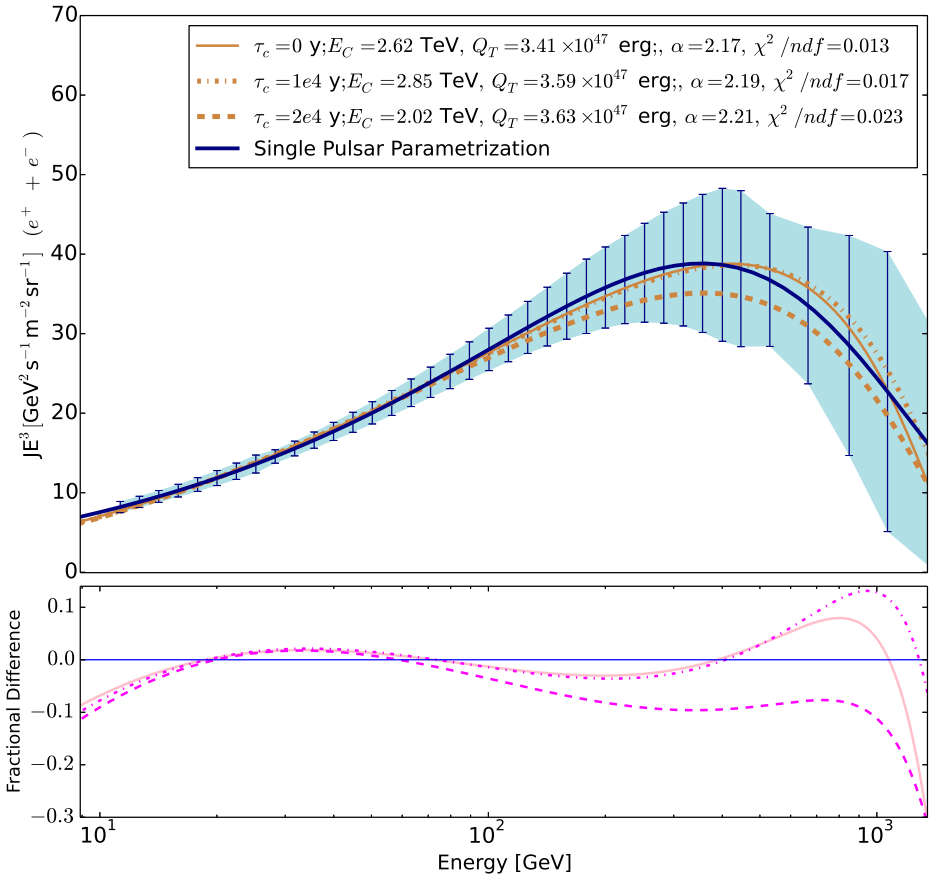


Figure 5.15: The single pulsar parametrization (eq. 5.5) with values obtained for best fit to CALET + AMS-02 for $E_d$ = 10 TeV (shown in blue line), is compared with the analytical calculation assuming Monogem pulsar for different confinement times (shown in brown lines). The errorbars and the shaded region represent CALET error. In the lower panel we show the fractional difference within 15% for the energy range 10 GeV to 3 TeV.

| **Model** Pulsar | $C_{e^-}$ $\left(\frac{\text{GeV}}{\text{s m}^2 \text{ sr}}\right)$ | $\frac{C_s}{C_{e^-}}$ | $\gamma_{e^-}$ | $\Delta\gamma_{e^-}$ | $E_g$ GeV | $s$ | $E_{pwn}$ TeV | $\frac{C_{pwn}}{C_{e^-}}$ | $\gamma_{pwn}$ | $\chi^2$ |
|---|---|---|---|---|---|---|---|---|---|---|
| $E_d = 10$ TeV | 716 | 0.065 | 3.22 | 0.201 | 40.9 | 0.05 | 0.7 | 0.0021 | 2.45 | 75.88 |
| | 719 | 0.065 | 3.23 | 0.203 | 40.7 | 0.05 | 0.7 | 0.0021 | 2.47 | 30.45 |
| $E_d = 2$ TeV | 705 | 0.059 | 3.20 | 0.224 | 40.3 | 0.05 | 1.5 | 0.0027 | 2.53 | 75.62 |
| | 707 | 0.057 | 3.20 | 0.223 | 40.3 | 0.05 | 1.5 | 0.0026 | 2.55 | 30.86 |

Table 5.2: Obtained Fit parameters from the best fit of different single pulsar models as extra source to the $e^+ + e^-$ (CALET) and $e^+$ (AMS-02) spectra along with the fixed parameters are listed here. Upper line (lower line) of each cell shows the values obtained without (with) including systematic error of CALET data.

## 5.5 Discerning Dark Matter and Pulsar Model with 5-year CALET Measurement

### 5.5.1 Simulated CALET Data assuming Dark Matter Decay as Extra Source

Using 627 days of flight data from CALET, it was shown that both DM decay and single pulsar model are capable of explaining the measurement. Assuming 5-years of measurement with CALET, now we study the discerning capability of pulsar spectrum and DM decay spectrum using the procedure as described in detail in section 4.7. CALET data were simulated assuming the flux prediction from the fit of the parametrization with DM as extra source and 5000 event samples were generated, assuming the detector aperture to be 1040 $\text{cm}^2\,\text{sr}$ [45]. The pulsar source parametrization is then fitted to these CALET $e^+ + e^-$ samples and the AMS-02 $e^+$ flux measurement, obtaining a $\chi^2$ distribution. Compared to the previous fit to CALET flight data, several fixed values of solar modulation potential ($\phi$) in the

range [0.35 GV, 0.65 GV], with step size 0.5 GV are tested. For the background cut-off energy parameter ($E_d$), 1 TeV, 2 TeV, 3 TeV, 5 TeV, 7 TeV, 10 TeV values are tested. These wide range of choices ensure the flexibility in the spectrum that deals with the uncertainties which can come from the choice of source distribution and propagation parameter.

In figure 5.16, we show an example of the single pulsar model fit to one of the 5000 CALET data samples, from the model with DM Model A as extra source. The same was done with taking DM Model B and DM Model C as extra sources as a part of the low $\gamma$-ray scenario study, and such examples of pulsar parametrization fit to simulated CALET + AMS-02 data are shown in figure 5.17 and figure 5.18 respectively.

To obtain a $\chi^2$ distribution for the DM models, the DM parametrization is re-fitted to the simulated data. In this fitting, the $\tau\tau\nu$ channel, which was previously excluded due to over-production of $\gamma$-rays, is now included, making 3 branching ratios as 3 free parameters. The branching fraction distribution for all three channels are shown in figure 5.19 for each DM model and as expected, the contribution from $\tau\tau\nu$ channel in all the cases are nearly zero. The $\chi^2$ distributions for DM Model A, DM Model B and DM Model C are shown in figure 5.20, figure 5.21, figure 5.22 respectively. For non-nested models like the decaying DM and pulsar model, Akaike's Information Criterion [219] is used to find the quality of the models to explain the measurement (see section 4.7 for details). From $\chi^2$ distribution plots for each studied cases, it is seen that each model (DM decay and pulsar) follows a normal distribution. Also, $\left(\chi^2_{\rm pulsar} - \chi^2_{\rm DM}\right)$, for each cases is positive for $\sim 90\%$ of the samples. So from the definition of AIC, we conclude qualitatively that the DM model which was used to simulate the CALET 5 years data, is favored to represent the CALET $e^+ + e^-$ simulated flux and AMS-02 $e^+$ flux, over the single pulsar model.

At 95 % CL threshold all the studied DM models are below this limit, except for few samples, and if the pulsar samples are excluded at the boundary, then one can conclude that DM model will be eventually distinguished from pulsar model with CALET measurement. The number of pulsar and DM samples from the fit to simulated CALET data + AMS-02 measurement that are over 95% CL

are listed in table 5.3. Since there's a possibility of $\chi^2$ tail to be shorter for the pulsar scenario due to fixed values of $E_d$, $s$, $\phi$, a Gaussian curve is fitted to the $\chi^2$ distributions to obtain a more conservative percentage on the number of excluded samples, which are also listed in table 5.3. As from the histogram one can conclude that DM samples have good fit quality in each case. Even excluding $\tau\tau\nu$ channel, the $\chi^2$ distribution is found to be equally good. This suggests that even with one less degree of freedom compared to pulsar model, the DM model can well represent the CALET simulated data. Compared to the results in discussed in section 4.7, here it was found that less than half of the pulsar samples would be excluded at $\chi^2 > 95\%$ CL. The number of excluded samples in each studied cases are listed in table 5.3. A maximum separation with a probability of $\sim 45\%$ is obtained for DM Model B and less for DM Model C and DM Model A. Reasons for low separation probability compared to the results obtained in the previous chapter, could be attributed to the facts that previous models were obtained by comparing with AMS-02 measurements, where data points are not available beyond 1 TeV, resulting in a larger contribution from $ee\nu$ channel. And no data points beyond 1 TeV also implies that background spectrum is steeper. As CALET data points are available beyond 1 TeV and we don't observe significant amount of flux suppression above 1 TeV energy, which could lead to a spectrum that resembles much with power-law and exponential cut-off spectrum (single pulsar model). Also, in the previous chapter, a single power-law with exponential cut-off + DM or single pulsar model could explain the AMS-02 total flux measurements. But using CALET flight data, and considering only statistical error, we found that single power-law with exponential cut-off and DM or pulsar cannot explain the CALET + AMS-02 measurements at 95% CL. A smoothly broken power-law allows for a higher flexibility in the spectrum which could give rise to similar spectral shape for the compared models.

Even though the maximum separation capability pulsar model from DM, is less than 50%, from the $\chi^2$ difference plot we see the average is $\sim 20$, for all the studied cases, suggesting a better separation method could yield interesting result. Specially for non-nested models where simple likelihood ratio test is not possible, an example of separating DM models from astrophysical sources by extending the parameter space of each models, are discussed in ref [226]. Also focusing near the region of cut-off (here DM mass), and particularly considering energy bins around

| **Model** DM | Pulsar Case Excluded Sample | | | DM Case Wrongly Excluded Sample | | | $\chi^2_{\rm pwn} - \chi^2_{\rm DM} > 0$ | |
|---|---|---|---|---|---|---|---|---|
| | Sample Number | Fraction | Fraction (Gaussian Fit) | Sample Number | Fraction | Fraction (Gaussian Fit) | Sample Number | Average value |
| Model A | 621 | 12.42% | 12.03% | 0 | 0% | $1 \times 10^{-3}$% | 4188 | 17.82 |
| Model B | 2237 | 44.74% | 44.21% | 0 | 0% | $1 \times 10^{-2}$% | 4791 | 29.35 |
| Model C | 1077 | 21.54% | 20.78% | 0 | 0% | $2 \times 10^{-2}$% | 4459 | 19.53 |

Table 5.3: Based on 5000 CALET data samples simulated for each DM model, the number of samples that are excluded at 95% CL from the fit of pulsar case and DM case to the simulated CALET $e^+ + e^-$ data + AMS-02 $e^+$ data are listed, as well as the fraction of excluded samples according to the fit of a normal distribution to each histogram.

better separation could be possible. The 'drop' $e^+ + e^-$ in flux measured by CALET is non-negligible, which can be explained 800 GeV DM, though as the data points are extended beyond 1 TeV with good statistics, the drop is the spectrum is not strong enough to create a discernible signature from the relatively smoother pulsar spectrum. Compared with the previous AMS-02 measurement this is a significant difference due to available high statistics data from CALET beyond 1 TeV, and to study the fine structures of CALET spectrum, other astrophysical scenarios (ex. multi-pulsar case) should be considered in relation with DM spectrum.

### 5.5.2 Simulated CALET Data assuming Single Pulsar as Extra Source

For a complete analysis, CALET capability of discerning DM decay model from single pulsar model the process described in the previous section was repeated, but now for simulated CALET data the flux prediction from the fit of the parametrization with pulsar as extra source is used. Here the best fit pulsar model for the

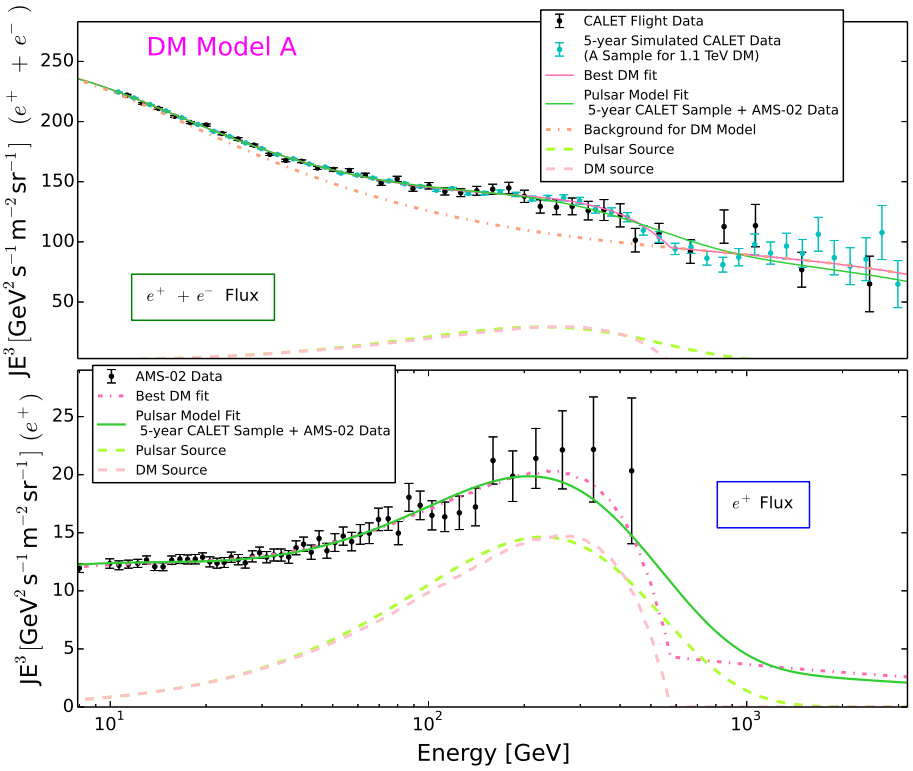


Figure 5.16: Fit of the single pulsar source (green line) to one of the 5000 statistical samples (cyan dots) of five year CALET measurement for $e^+ + e^-$ flux (upper panel) assuming DM Model A as extra source and $e^+$ flux measured by AMS-02 (lower panel) data is shown here. Dotted lines in the upper panel represents the background spectrum for the DM source. Pulsar source and DM decay contribution in the $e^+ + e^-$ flux and $e^+$ flux are shown with green and pink dashed lines respectively. Black error-bars represent CALET and AMS-02 flight data.

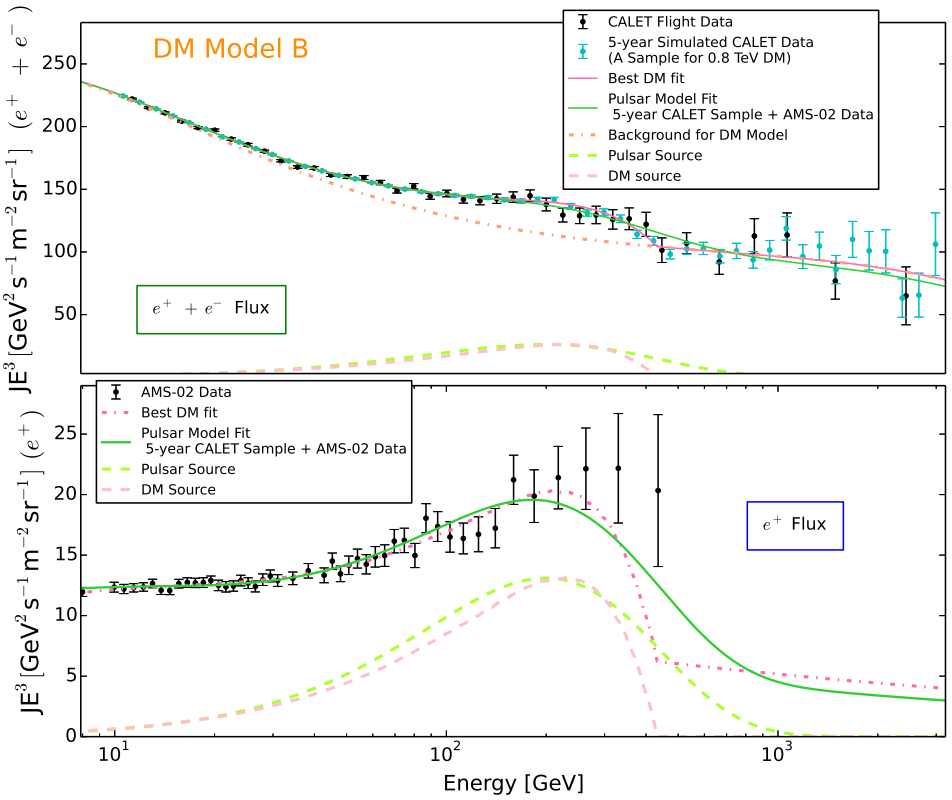


Figure 5.17: Same as figure 5.16 but we assume DM Model B as extra source for generating five year CALET data samples.

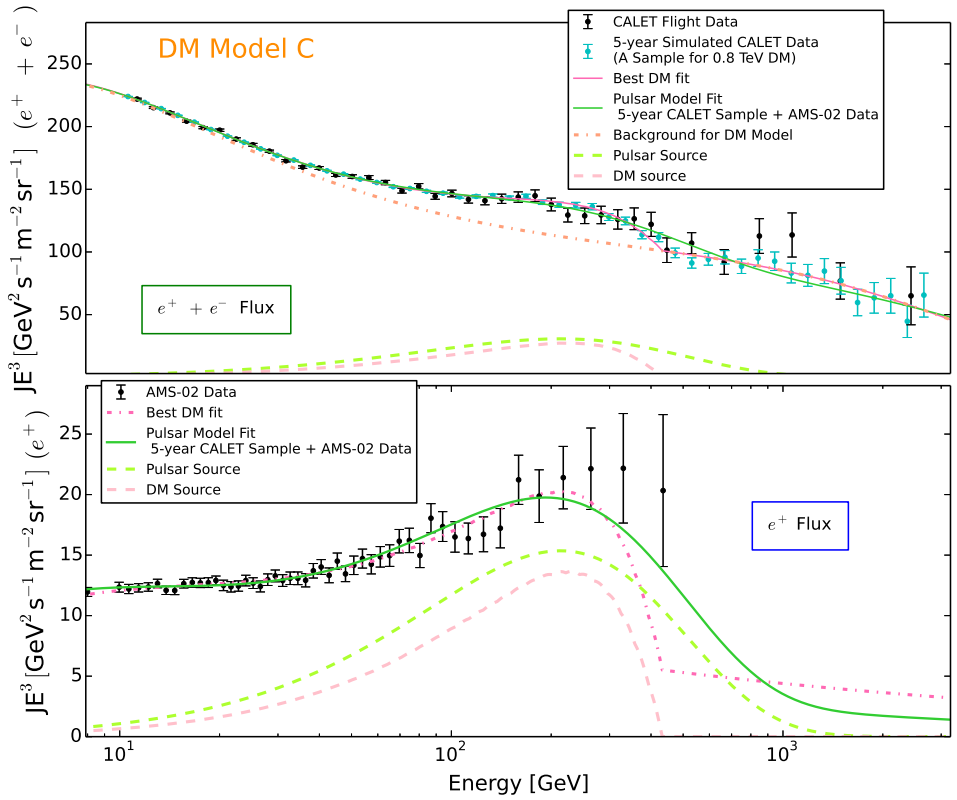


Figure 5.18: Same as figure 5.16 but we assume DM Model C as extra source for generating five year CALET data samples.

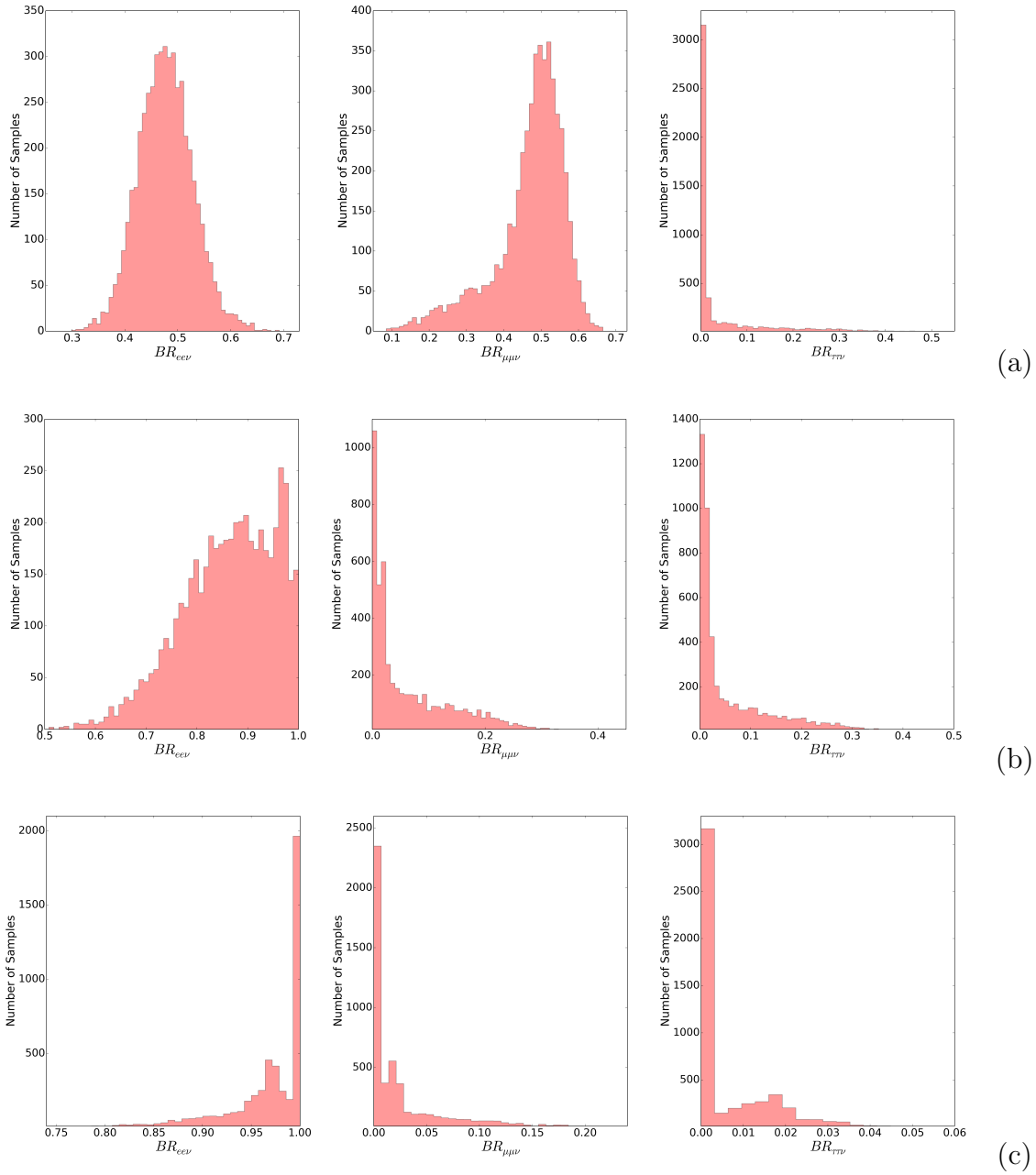


Figure 5.19: Distribution of branching ratios obtained from the re-fit of DM model A (figure a), DM model B (figure b), DM model C (figure c) to the 5000 CALET statistical samples of five year CALET measurement for $e^+ + e^-$ flux + AMS-02 $e^+$ flux are shown here. $BR_{\tau\tau\nu}$ is close to zero for a large number of samples for all the studied cases.

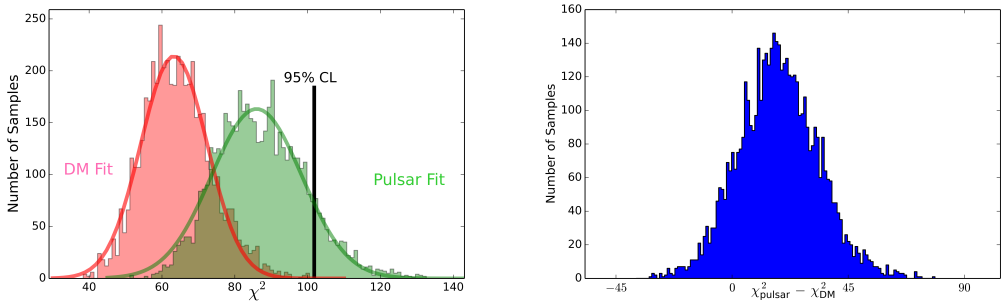


Figure 5.20: $\chi^2$ distribution for the fit of the single pulsar source to the simulated CALET data for 5000 DM Model A samples + AMS-02 positron flux data (green) and re-fit of DM samples using the same data points (pink).

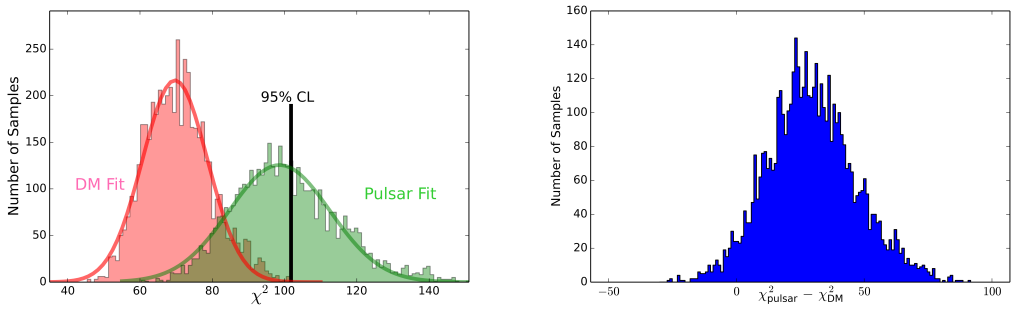


Figure 5.21: Same as figure 5.20 but the CALET data samples were generated assuming decay of DM Model B.

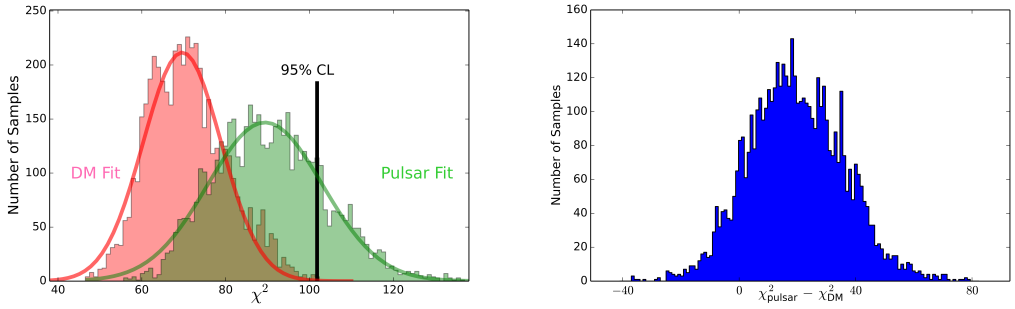


Figure 5.22: Same as figure 5.21 but now the for the DM Model C.

background cut-off energy ($E_d$) of 10 TeV is taken as the extra source. 5000 event samples were generated and the 800 GeV decaying DM model was fitted to the simulated CALET $e^+ + e^-$ data and AMS-02 $e^+$ flux. The fit considering a decaying DM of mass 800 GeV to one such simulated CALET sample with pulsar as extra source is shown in figure 5.23. Here only 800 GeV DM mass was considered as the CALET spectrum has a 'drop' like structure around 400 GeV, but in an ideal scenario the DM mass should be taken as a free parameter to obtained the best-fit results. Due to time constrain only a special case with 800 GeV DM is studied. The branching ratio for all three channels are plotted in figure 5.24 for 5000 samples and the contribution from $\tau\tau\nu$ channel is nearly zero. The pulsar model which was used to simulate CALET 5-years measurement is then refitted to the simulated samples and another $\chi^2$ distribution is obtained and these distributions are shown in figure 5.25. Following AIC, as the $\chi^2$ distribution for both DM and pulsar model follow a normal distribution and the $\chi^2$ difference $\left(\chi^2_{\rm DM} - \chi^2_{\rm pulsar}\right)$ between pulsar model fit and DM model re-fit is positive for all the generated samples, it can be concluded that the pulsar model is more suitable to represent the simulated CALET $e^+ + e^-$ flux + AMS-02 $e^+$ flux. So to conclude this analysis, it is shown that using the pulsar model as as extra source to simulate CALET data assuming 5 years of data taking, a fixed particular DM mass can be separated with CALET data, however this result should not be generalized for all the DM masses.

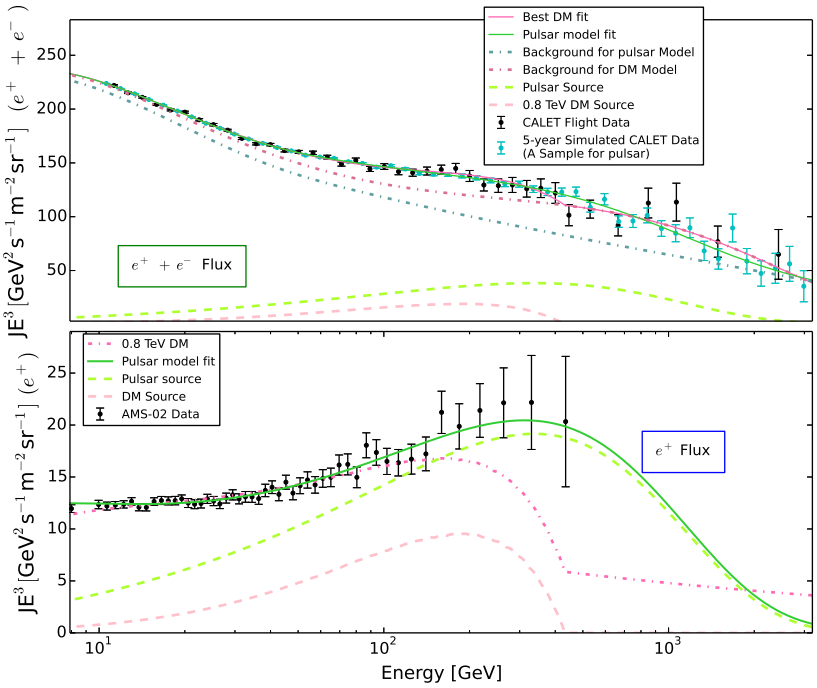


Figure 5.23: Fit of 800 GeV DM to one of the 5000 statistical samples (cyan dots) of five year CALET measurement for $e^+ + e^-$ flux (upper panel) assuming single pulsar ($E_{\rm pwn} = 0.7$ TeV, $E_d = 10$ TeV) as extra source and $e^+$ flux measured by AMS-02 (lower panel) data is shown here. The pulsar model re-fit to the same simulated data is also shown. Dotted lines in the upper panel represents the background spectrum for the pulsar and DM source. Pulsar source and DM decay contribution in the $e^+ + e^-$ flux and $e^+$ flux are shown with green and pink dashed lines respectively. Black error-bars represent CALET and AMS-02 flight data.

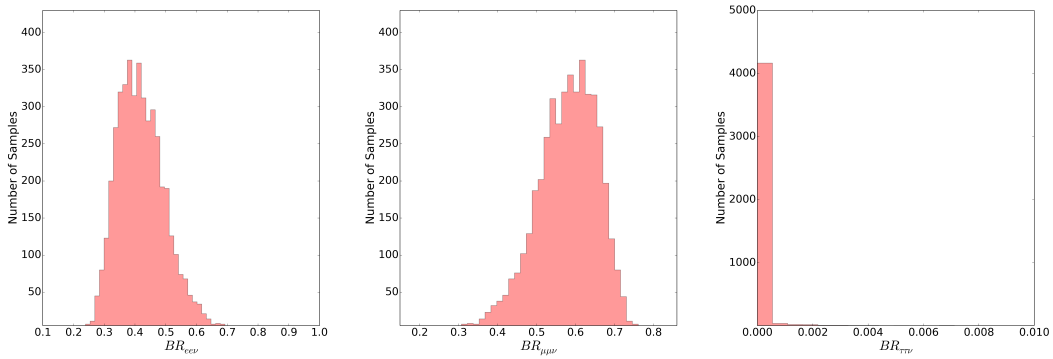


Figure 5.24: Distribution of branching ratios obtained from the fit of 0.8 TeV DM to the 5000 CALET statistical samples of five year CALET measurement with pulsar as extra source ($E_d = 10\,\mathrm{TeV}$) for $e^+ + e^-$ flux + AMS-02 $e^+$ flux are shown here. $BR_{\tau\tau\nu}$ is close to zero for a large number of samples for the studied DM mass.

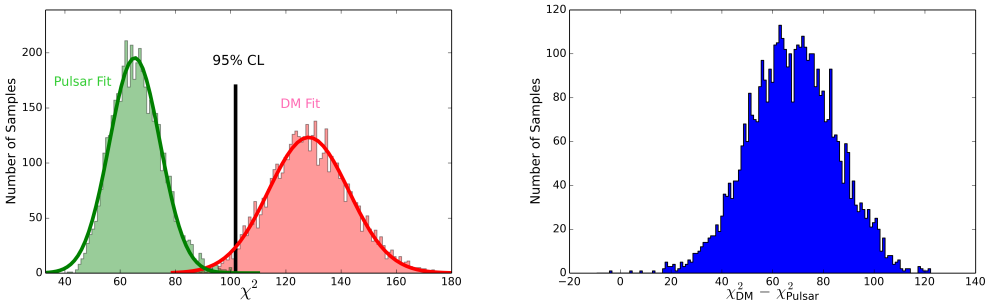


Figure 5.25: $\chi^2$ distribution for the fit of the 0.8 TeV decaying DM to the simulated CALET data for 5000 single pulsar source samples + AMS-02 positron flux data (pink) and re-fit of pulsar samples using the same data points (green). The chosen DM mass is well separated from pulsar model at 95 % CL.

# Chapter 6

# Conclusion and Discussions

With the high precision CR measurements the recent and upcoming years are very exciting in the field of CR physics. Precise measurement of CRs are key for the understanding of CR propagation and properties of ISM in the galaxy. In this context, the prospects of CALET detector on measuring CR $e^+ + e^-$ spectrum is described in detail. The main results presented in this thesis are possibility of discerning a decaying DM signal from a generic single pulsar source with 5 years of simulated CALET data and investigation of spectral features of real time $e^+ + e^-$ spectrum measured with CALET on the ISS for two years.

Recent observation of CR positron excess could be attributed to nearby astrophysical sources such as pulsars or decay and annihilation of DM. CALET's capability to precisely measure the $e^+ + e^-$ spectrum has a crucial role to play in identifying signatures from these exotic CR sources. To calculate the propagation of CRs from the source to Earth, GALPROP numerical package is used and it's described in detail. It is shown that in GALPROP the propagation calculation of electrons depend on the number of energy bins and a method to mitigate this problem is discussed. Effect of the modification on the background CR spectrum as well as DM annihilation spectrum is shown. Also the spiral arm structure of Milky Way galaxy and its effect on the propagation of charged CRs are discussed. GALPROP source distribution is modified in a simple way so that it reflects the spiral arm nature of Milky Way and the variation of the spectral shape with spiral

arm thickness are calculated with GALPROP and results are plotted. As the decay products of DM are propagated in GALPROP, the propagation parameters are determined by comparing with the nuclei measurement results with the spiral arm modification in GALPROP. CR electron and positron flux from a decaying DM to three SM leptons are calculated and it's shown that it can explain the current CR positron excess. In this regard, a Fermionic DM model is discussed and it's shown that this model can explain the positron excess and compatible with the Fermi-LAT $\gamma$-ray measurement. The DM candidate with the lowest $\gamma$-ray flux has the most prominent detectable signature in the CR $e^+ + e^-$ spectrum. The decay of these specific cases are characterized by a hard drop around half of the DM mass, which can be well discerned by CALET from a relatively smooth pulsar spectrum.

Also 2 years of real time CALET measurement of CR $e^+ + e^-$ spectrum is investigated and the results are presented in detail in this thesis. It's shown that $e^+ + e^-$ spectrum measured by CALET cannot be represented by a single power-law spectrum with pulsar or 3 body DM decay as extra source, for the whole energy range. A smoothly broken power-law for primary electron flux with DM decay or single pulsar as extra source providing electron-positron pairs can well explain the combined CALET ($e^+ + e^-$) and AMS-02 ($e^+$) measurements. From the combined analysis of CALET and AMS-02 measurements, allowed range of DM masses and pulsar cut-off energies are calculated, and effect other related parameters in the parametrization are discussed in detail. Based on the allowed range of DM mass, it was shown that for an 800 GeV DM decaying to $\mu\mu\nu$ and $ee\nu$ which can explain CALET $e^+ + e^-$ flux and AMS-02 $e^+$ flux, is compatible with Fermi-Lat $\gamma$-ray measurements. Also assuming 5-year data taking, possibility of discerning such DM from generic single pulsar source is discussed. In the light of CALET and other precise CR experiments, distinct spectral features the high energy domain can reveal many details about CR sources and acceleration mechanism and which will help us in answering some of the long standing questions. Directly measuring electron spectrum with CALET up to 20 TeV along with observation of other nuclei will guide us in the future to unravel cosmic mysteries.

# Appendices

# Appendix A

# Energy Distribution of the DM Decay Products

Fermionic DM candidate decays to SM leptons ($N_L \rightarrow ll\nu$) by breaking the $B-L$ symmetry by 2 units and the Lagrangian that describes the process can be written as $h\,\eta^{\dagger}\overline{N}\,l + f\,\chi^{\dagger}\,l\nu$. A schematic Feynman diagram for the process is shown in figure A.1 and the mediating particles in the decay are the heavy scalars $\chi, \eta$. Mass range of these scalars are $\mathcal{O}(10^3)$ TeV much higher than the DM mass ($\mathcal{O}$(TeV)) and SM leptons. Lifetime of the mediating scalars can be assumed to be negligible and this process can be approximated as a 4 point Fermi interaction, similar to muon decay process. Assuming this the energy distributions of the decay products are calculated.

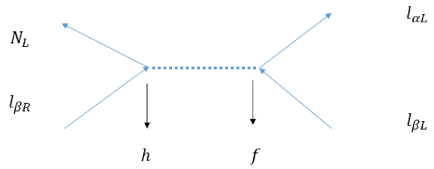


Figure A.1: A schematic Feynman diagram of the fermionic DM ($N_L$) decay process to SM leptons ($l$). $h$, $f$ are the coupling constants for the vertices where the decay is mediated by heavy charged scalars $\eta$ and $\chi$.

The invariant amplitude for muon decaying to electron, muon neutrino and anti-electron neutrino ($\mu\,(p) \to e\,(p') + \nu_\mu\,(k) + \bar{\nu_e}\,(k')$) can be written as

$$M = \frac{G}{\sqrt{2}}[\overline{u(k)}\,\gamma^\mu(1-\gamma^5)\,u(p)]\,[\overline{u(p')}\,\gamma_\mu(1-\gamma^5)\,v(k')]\,, \tag{A.1}$$

where $G$ is the 4-point coupling constant. Using this the decay rate can be calculated as

$$d\Gamma = \frac{1}{2E}|\ M\ |^2 dQ\ , \tag{A.2}$$

where $dQ$ is the invariant phase space written as

$$dQ = \frac{d^3p'}{2E'}\,\frac{d^3k}{2\omega}\,\frac{d^3k'}{2\omega'}\,\frac{(2\pi)^4}{(2\pi)^9}\,\delta^4(p-p'-k-k')\,. \tag{A.3}$$

Using the formula $\int \frac{d^3k}{2\omega} = \int d^4k\theta(\omega)\delta(k^2)$ , after performing $d^3k$ integration, the above equation can be reduced to

$$dQ = \frac{1}{(2\pi)^5}\,\frac{d^3p'}{2E'}\,\frac{d^3k'}{2\omega'}\,\theta(E-E'-\omega')\delta((p-p'-k')^2) \tag{A.4}$$

To calculate invariant amplitude we need several formulas, to start with

$$\sum_{\text{all spins}} [\overline{u(a)}\Gamma_1 u(b)]\,[\overline{u(a)}\Gamma_2 u(b)]^* = Tr[\Gamma_1(\not{p}_b + m_b)\,\overline{\Gamma_2}(\not{p}_a + m_a)] \tag{A.5}$$

So using this technique which is known as Casimir's Trick, eq. A.1 can be reduced as

$$\begin{aligned} |\ M\ |^2 \ &= \ \frac{G^2}{2} Tr[\gamma^\mu\,(1-\gamma^5)\not{k}\,\gamma^\nu(1-\gamma^5)\,(\not{p}+m_\mu)] \\ &\quad \times Tr[\gamma_\mu\,(1-\gamma^5)\,(\not{p}'+m_e)\gamma_\nu\,(1-\gamma^5)\,\not{k}'] \end{aligned} \tag{A.6}$$

where neutrinos are assumed massless. To reduce this equation few more trace theorems are used as

$$Tr(1) = 4 \qquad \text{(A.7)} \qquad Tr(\gamma^\mu\,\gamma^\nu) = 4g^{\mu\nu} \quad \text{(A.8)} \qquad Tr(\not{a}\,\not{b}) = 4(a\cdot b) \quad \text{(A.9)}$$

$$Tr(\gamma^\mu\gamma^\nu\gamma^\lambda\gamma^\sigma) = 4(g^{\mu\nu}g^{\lambda\sigma} - g^{\mu\lambda}g^{\nu\sigma} + g^{\mu\sigma}g^{\nu\lambda}) \tag{A.10}$$

Since $\gamma^5$ matrix is involved, few more trace theorems using $\gamma^5$ matrices are described. $\gamma^5$ is a product of even number of matrices, $\gamma^5 = i\gamma^0\gamma^1\gamma^2\gamma^3$ and trace of the product of odd number of gamma matrices are zero, it follows that $Tr(\gamma^5\gamma^\nu) = 0$. Some other important rules involving $\gamma^5$ matrix that will be used in this calculations are

$$Tr(\gamma^5\gamma^\mu\gamma^\nu\gamma^\lambda\gamma^\sigma) = 4i\epsilon^{\mu\nu\lambda\sigma}\,;\; Tr(\gamma^5) = 0\,. \tag{A.11}$$

Now considering the first trace term from eq. A.6 and using the above mentioned rules, the second trace will reduce in the following manner

$$\begin{aligned} Tr[\gamma^\mu(1-\gamma^5)\not{k}\gamma^\nu(1-\gamma^5)(\not{p}+m_\mu)] &= Tr[\gamma^\mu(1-\gamma^5)\not{k}\gamma^\nu(1-\gamma^5)\not{p} \\ &\quad +\gamma^\mu(1-\gamma^5)\not{k}\gamma^\nu(1-\gamma^5)m_\mu]\,. \end{aligned} \tag{A.12}$$

The second term in the above equation gives zero because it involves odd number of gammas. Expanding the first term gives

$$\begin{aligned} &= Tr[\gamma^\mu\not{k}\gamma^\nu\not{p}] - Tr[\gamma^\mu\gamma^5\not{k}\gamma^\nu\not{p}] - Tr[\gamma^\mu\not{k}\gamma^\nu\gamma^5\not{p}] \\ &\quad +Tr[\gamma^\mu\gamma^5\not{k}\gamma^\nu\gamma^5\not{p}]\,. \end{aligned} \tag{A.13}$$

Reducing these matrices term by term

$$\begin{aligned} Tr[\gamma^\mu\not{k}\gamma^\nu\not{p}] &= Tr[\gamma^\mu k_\lambda\gamma^\lambda\gamma^\nu p_\sigma\gamma^\sigma] \\ &= k_\lambda p_\sigma Tr[\gamma^\mu\gamma^\lambda\gamma^\nu\gamma^\sigma] \\ &= k_\lambda p_\sigma 4(g^{\mu\lambda}g^{\nu\sigma} - g^{\mu\nu}g^{\lambda\sigma} + g^{\mu\sigma}g^{\lambda\nu}) \text{ (using eq. A.10)} \\ &= 4(k^\mu p^\nu - g^{\mu\nu}(p\cdot k) + k^\nu p^\mu)\,. \end{aligned} \tag{A.14}$$

$$\begin{aligned} Tr[\gamma^\mu\gamma^5\not{k}\gamma^\nu\not{p}] &= Tr[\gamma^\mu\not{k}\gamma^\nu\gamma^5\not{p}] \\ &= Tr[\gamma^\mu k_\lambda\gamma^\lambda\gamma^\nu\gamma^5 p_\sigma\gamma^\sigma] \\ &= k_\lambda p_\sigma Tr[\gamma^\mu\gamma^\lambda\gamma^\nu\gamma^5\gamma^\sigma] \\ &= -4ik_\lambda p_\sigma\epsilon^{\mu\nu\lambda\sigma}\text{(using eq. A.11)}\,. \end{aligned} \tag{A.15}$$

Since $(\gamma^5)^2 = 1$ fourth term from eq. A.12 reduces in a similar manner as the first term. So eq. A.12 finally reduces to

$$8(k^\mu p^\nu - g^{\mu\nu}(p\cdot k) + k^\nu p^\mu - i\epsilon^{\mu\nu\lambda\sigma}k_\lambda p_\sigma)\,. \tag{A.16}$$

On a similar way second trace of eq. A.6 will be

$$8(p'_\mu k'_\nu - g_{\mu\nu}(p'\cdot k') + p'_\nu k'_\mu - i\epsilon_{\mu\nu\kappa\tau}p'^\kappa k'^\tau)\,. \tag{A.17}$$

So multiplying eq. A.16 and A.17 we finally get the spin average probability

$$\mid M \mid^2 = 64G^2(k \cdot p')(p \cdot k') \,. \tag{A.18}$$

In muon rest frame $p = (m_\mu, 0)$, so $(p \cdot k') = m_\mu \omega'$ , to determine $(k \cdot p')$, we use $p = p' + k + k'$, so that

$$\begin{aligned} (p' + k)^2 &= p'^2 + k^2 + 2p' \cdot k \\ &= m_e^2 + 2p' \cdot k \\ &= p^2 + k'^2 - 2p \cdot k' \\ &= m_\mu^2 - 2m_\mu \omega' \,. \end{aligned} \tag{A.19}$$

From the above equation one can determine $(p' \cdot k)$. If we neglect the mass of the electron as $m_\mu > 200 m_e$ then $2(k \cdot p')(k' \cdot p) = (m^2 - 2m\omega')m\omega'$. Using this, eq. A.2 can be rewritten as

$$\begin{aligned} d\Gamma &= \frac{1}{2m} 32G^2(m^2 - 2m\omega')m\omega' dQ \\ &= \frac{G^2}{2m\pi^5} \frac{d^3p' d^3k'}{2E'2\omega'} (m^2 - 2m\omega')m\omega' \\ &\quad \times \delta(m^2 - 2mE' - 2m\omega' - 2E'\omega'(1 - \cos\theta)) \,. \end{aligned} \tag{A.20}$$

Assuming spherical polar coordinates $d^3p' d^3k'$ can be reduced as

$$d^3p' d^3k' = 4\pi E'^2 \, dE' \, 2\pi \, \omega'^2 \, d\omega' \, d\cos\theta \tag{A.21}$$

where $\theta$ is the polar angle designating the angle between $e$ and $\bar{\nu}_e$, and integration over azimuthal angle $\phi$ gives $4\pi$. Also using $\delta(.....+2E'\omega'\cos\theta) = \frac{1}{2E'\omega'} \, \delta(.....-\cos\theta)$ and perform the integration over the angle $\theta$ one can obtain the decay width as

$$d\Gamma = \frac{G^2}{2\pi^3} dE' d\omega' m\omega'(m - 2\omega') \,. \tag{A.22}$$

The limits on the energies of neutrino and electron are $\frac{1}{2}m - E \leq \omega' \leq \frac{1}{2}m$, and $0 \leq E \leq \frac{1}{2}m$ respectively. To find out the energy spectrum of the electron we

perform the $\omega'$ integration

$$\begin{aligned}
\frac{d\Gamma}{dE'} &= \frac{mG^2}{2\pi^3}\int_{\frac{1}{2}m-E'}^{\frac{m}{2}} d\omega'\omega'(m-2\omega') \qquad (A.23)\\
&= \frac{mG^2}{2\pi^3}(m\frac{\omega'^2}{2}-2\frac{\omega'^3}{3})_{\frac{m}{2}-E'}^{\frac{m}{2}}\\
&= \frac{mG^2}{2\pi^3}[\frac{m}{2}(\frac{m^2}{4}-\frac{m^2}{4}+mE'-E'^2)\\
&\quad -\frac{2}{3}(\frac{m^2}{8}-\frac{m^2}{8}+3\frac{m^2}{4}E'-3\frac{m}{2}E'^2+E'^3)]\\
&= \frac{G^2}{12\pi^3}m^2E'^2(3-\frac{4E'}{m})\ .
\end{aligned}$$

This quantity represents the transition rate per unit energy of electrons where the energy of the electrons lie between $E$ and $E+dE$. When we observe electrons coming out of a muon decay then the probability that electron energy lie between $E$ and $E+dE$ is $\frac{1}{\Gamma}\frac{d\Gamma}{dE'}\,dE'$, where $\Gamma$, the total decay width of the muon is given by $\Gamma=\frac{G^2m^5}{192\pi^3}$.

We can see from equation above that the fractional decay width depends only on the energy of the outgoing anti-neutrino. So the energy distribution of muon will be same as electron if $dE'$ is replaced with $d\omega$. So the energy distribution of the outgoing left handed leptons is

$$\frac{d\Gamma}{dE_l}=\frac{G^2}{12\pi^3}m^2E_l^2(3-\frac{4E_l}{m})\,, \qquad (A.24)$$

Where $l$ denotes particle species. For simplification, above equation can be further reduced and written in terms of $x$, where $x_i=\frac{E_l}{E_{max}}$ where $i$ denotes electron and muon neutrino and $E_{max}=m_\mu/2$. $dx=\frac{2dE_l}{m}$, so for electron

$$\frac{d\Gamma}{dx_l}=\frac{G^2m^5}{96\pi^3}x_l^2(3-2x_l) \qquad (A.25)$$

So the probability distribution for the left handed leptons will be...

$$\frac{1}{\Gamma}\frac{d\Gamma}{dx_l}=2x_l^2(3-2x_l)\,. \qquad (A.26)$$

For four point interaction we assume isotropic distribution, so the probability distribution is independent of the outgoing particles. But, going back to eq. B.27 one can see that the fractional decay rate is a function of outgoing anti-neutrino energy($\omega'$) (This comes from the invariant amplitude calculation where it's

assumed that muon decays to $\mu_\nu$ and $W$ boson, which then produces electron and anti-neutrino]. So the energy spectrum of the anti neutrino can be written as

$$\begin{aligned}
\frac{d\Gamma}{d\omega'} &= \frac{mG^2}{2\pi^3}\int_{\frac{1}{2}m-\omega'}^{\frac{m}{2}} dE'\omega'(m-2\omega') \\
&= \frac{mG^2}{2\pi^3}(m\omega' E' - 2\omega'^2 E')_{\frac{m}{2}-\omega'}^{\frac{m}{2}} \\
&= \frac{mG^2}{2\pi^3}[m\omega'(\frac{m}{2}-\frac{m}{2}+\omega') \\
&\quad -2\omega'^2(\frac{m}{2}-\frac{m}{2}+\omega'] \\
&= \frac{G^2}{2\pi^3}m^2\omega'^2(1-\frac{2\omega'}{m})
\end{aligned} \tag{A.27}$$

So the energy spectrum of the outgoing electron and muon neutrino is given by eq. A.26, whereas the energy distribution of the outgoing anti-neutrino is given by equation above. We write the above equation as a function of $x$ where $x = \frac{E}{E_{max}}$

$$\frac{d\Gamma}{dx_{\bar{\nu}}} = \frac{G^2m^5}{16\pi^3}x_{\bar{\nu}}^2(1-x_{\bar{\nu}})\,. \tag{A.28}$$

So the probability distribution for outgoing anti-neutrino is

$$\frac{1}{\Gamma}\frac{d\Gamma}{dx_{\bar{\nu}}} = 12x_{\bar{\nu}}^2(1-x_{\bar{\nu}})\,. \tag{A.29}$$

Since neutrinos do not contribute to CR electron-positron spectrum this is not needed for the calculation of CR electron-positron pair from the fermionic DM.

# Appendix B

# Comparison of Parametrization and GALPROP Calculation

To link the fitted values of the parameters of the parametrization described in section 4.4, with a specific model of CR propagation, parametrized flux is compared with the GALPROP propagation calculations and the results are shown in figure B.1. In the lower panel of figure B.1, we show the deviation between GALPROP calculation and parametrization and in the relevant energy range the difference is on the order of 70% at most. As shown in figure B.1a, the GALPROP calculation with $\sigma = 0.6$ kpc, corresponds to a value of 2 TeV for $(E_d)$ in the parametrization. Variation of $(E_d)$ in the parametrization represents different values of the $\sigma$ parameter in the numerical calculation which represents the ring thickness in this new GALPROP source distribution.

Electron-only flux from Vela SNR is calculated in GALPROP assuming propagation parameters as listed in table 3.2, except that the time progression is taken as 1200 steps of 10 years and the spatial grid distance is 0.1 kpc in a cube of 12 kpc calculated on the solar system. This flux added to the GALPROP calculated spectrum from distant SNR with $\sigma = 0.5$ kpc corresponds best to the parametrization with a value of 10 TeV for $E_d$ as is shown in figure B.1b. Emission of CRs from the Vela SNR is assumed to be instantaneous and the total energy emitted as electron above 1 GeV normalized to $10^{48}$ erg [57]. It should also be

noted that a harder injection spectrum [57] and/or a specific energy-dependent release [222] of the electrons from Vela could create a distinct signature in the TeV region, like a sharp cut-off in the low energy-part of the Vela spectrum. If such a signature is found by CALET, the background model for DM search would have to be adapted.

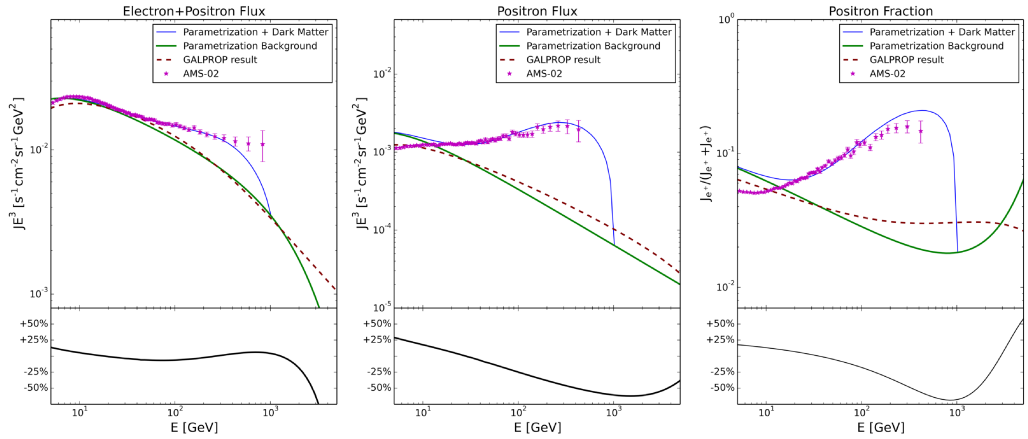


(a)

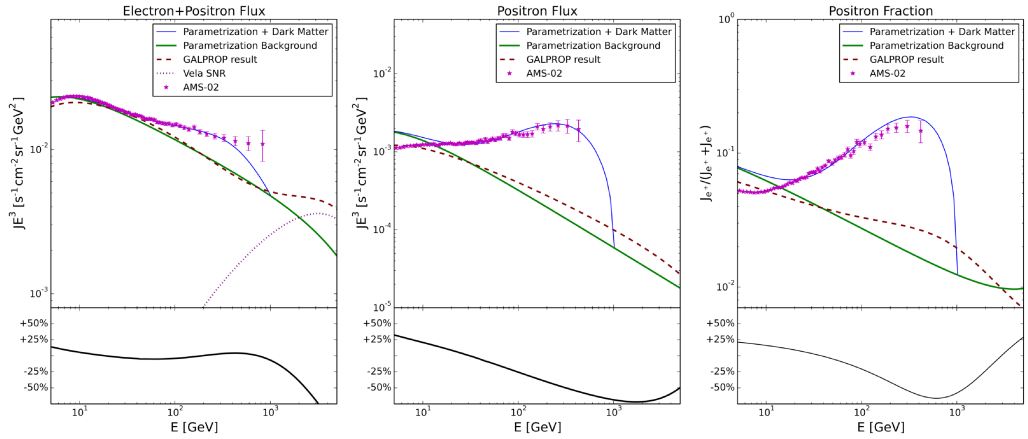


(b)

Figure B.1: (a) CR spectra calculated with GALPROP (red dotted line) with $\sigma = 0.6$ kpc are compared with the parametrization (green line) with DM as extra source and $E_d = 2$ TeV. In the lower panel the fractional difference between the GALPROP results and parametrization are shown. (b) Same as figure B.1a but now with $\sigma = 0.5$ kpc for the GALPROP calculation and $E_d = 10$ TeV in the parametrization to which Vela SNR (magenta dots) is added.

# Appendix C

# An Update Based on CALET Extended Results

During the preparation of finalizing the thesis and studies related to it, CALET published extended measurement of $e^+ + e^-$ spectrum on July 2018, extending the highest energy of measurement from 3 TeV to 4.8 TeV [227]. This updated results is based on 780 days of observance with full geometrical acceptance and increased statistics by a factor of $\sim 2$. The flux measurements were given using the same energy bin as the previous result [45] but one extra added energy bin is added at the highest energy region. The green band in figure C.1, represents the quadratic sum of statistical and systematic error. The $e^+ + e^-$ spectrum below 1 TeV is well consistent with AMS-02 measurement, while it is much softer compared to Fermi-Lat or DAMPE measurement in the energy region 300 GeV-600 GeV, which indicate the presence of unknown systematics in various experiments. The CALET results are compared with DAMPE results which suggested a break in the energy spectrum at $\simeq 0.9$ TeV [48], and it is found that considering a broken power-law with a fixed break energy at 914 GeV gives a good fit $\left(\frac{\chi^2}{\text{ndf}} \approx 17/25\right)$ to CALET measurement. This suggests the flux suppression in the TeV region of the spectrum is compatible with DAMPE measurement and with better statistics the accurate position of break energy and spectral behavior in the TeV region will be more clear. Another important finding was the peak like structure in the DAMPE spectrum at 1.4 TeV energy bin (which consequently led to many DM influenced studies,

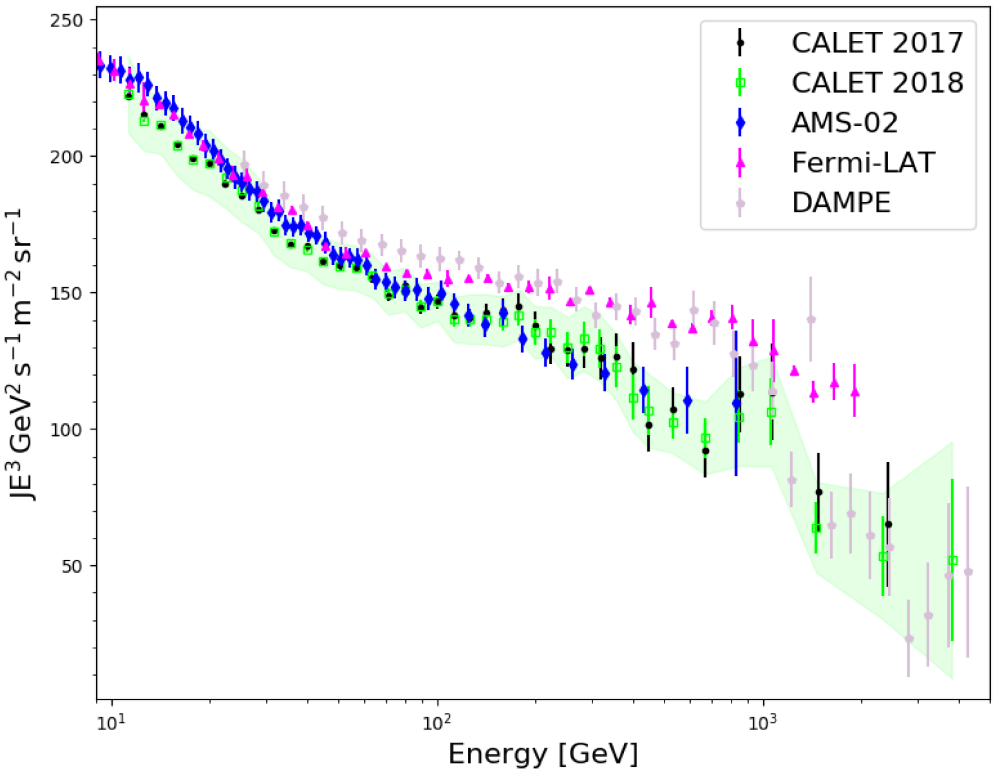


Figure C.1: CR $e^+ + e^-$ flux measured by CALET up to 4.8 TeV is shown here with the quadratic sum of systematics and statistical errors are included in the green band. This measurement is compared with previous CALET result and other direct measurements by space-based detectors.

e.g. [228–231]), was found to be incompatible with CALET measurement at $4\sigma$ significance, including the systematic errors for both experiments.

In consistent with our previous studies, here also either the decaying DM model or the single pulsar model was used as potential extra source to explain the combined measurement of new CALET results + AMS-02 positron flux measurement. Due to an increase in statistical accuracy in the new measurement by a factor of $\sim 2$, we found that considering a smoothly broken power-law + either DM or pulsar model cannot explain the new CALET (only statistical error) + AMS-02 (statistical + systematical) positron flux measurements at 95% CL. So compared with the previous results, using the updated CALET measurements, no parameter

space remains for either the DM or pulsar model. Considering the systematics of CALET measurements assuming a background cut-off energy $E_d = 10$ TeV, with solar modulation potential set to 0.5 GV, the best fit plots for Decaying DM and the single pulsar model are shown in figure C.2, C.3 respectively. We found that for the above mentioned background parameters, for the DM model, the least $\chi^2$ was obtained for an 1.1 TeV DM decaying to 54% $ee\nu$ and 46% $\mu\mu\nu$ channel with lifetime of $3.33 \times 10^{26}$ s. Similarly for the single pulsar model the least $\chi^2$ was obtained for a source cut-off energy of 650 GeV. Including the systematics of CALET makes it difficult to select or reject specific extra source scenarios as for a wide range of parameters, either DM or pulsar models are allowed at 95% CL. So using updated CALET measurements it is not so significant to replicate the analysis we have done before. However in the updated measurements a detailed breakdown of the systematic error is given, including errors due to charge identification, BDT stability, trigger etc. It would be interesting to study these contributing errors as nuisance parameters and their effects on the combined fit. Expanding the direct measurements of CR $e^+ + e^-$ flux for the first time in the TeV regions with CALET and DAMPE would also open doors to search for answers of many long standing questions such as measuring local diffusion coefficients [232]. Due to time constraint such studies are beyond this thesis but will be explored in the near future.

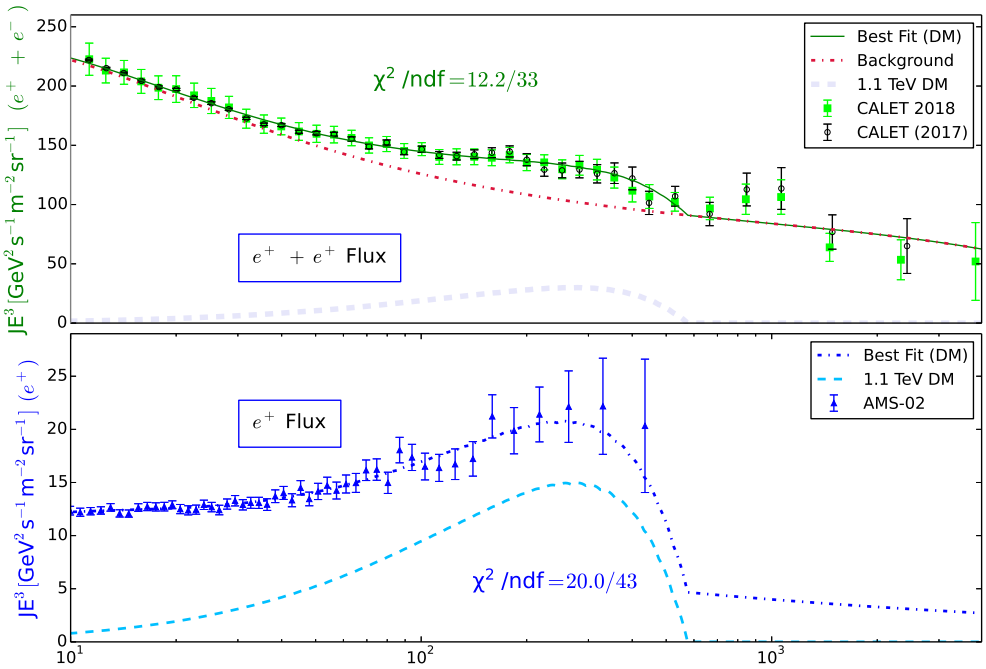


Figure C.2: Broken power-law and 1.1 TeV decaying DM is taken as a test case (green line) to explain the combined new CALET ($e^+ + e^-$) (upper panel) + AMS-02 ($e^+$) measurements (lower panel). New CALET data points are shown using green squares. Background $e^+ + e^-$ spectrum with $E_d = 10$ TeV, $\phi = 0.5$ GV, s=1.0 are shown with red dotted lines. DM contributions in the upper and lower panel are shown with grey and cyan dashed lines.

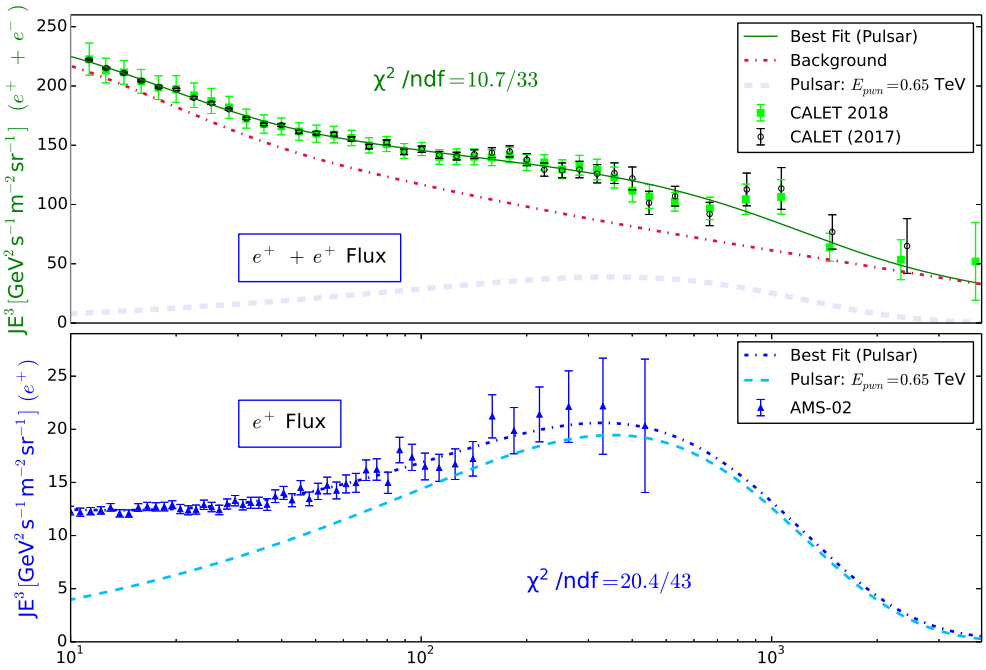


Figure C.3: Broken power-law and single pulsar with exponential cut-off is taken as a test case (green line) to explain the combined new CALET ($e^+ + e^-$) (upper panel) + AMS-02 ($e^+$) measurements (lower panel). New CALET data points are shown using green squares. Background $e^+ + e^-$ spectrum with $\phi = 0.5\,\mathrm{GV}$, s=0.05, $E_d = 10$ TeV are shown with red dotted lines. Pulsar contributions in the upper and lower panel are shown with grey and cyan dashed lines.

# Acknowledgment

First of all I would like to express my deepest gratitude to my supervisor Shoji Torii, without whom this thesis would have never finished within the due time. From first day in the lab and the welcome party to deal with the visa issues at the end, he was there for me always. I would like to use this opportunity to thank my co-supervisors Motz-san and Asaoka-san for showing endless patience and constant support through the past 5 years, specifically to Motz-san for constant evaluation of my work and helping with other daily issues that a foreigner can face while studying in Japan.

I'm very thankful to Dr. K.Kohri for discussing the Fermionic Dark Matter model in detail with us. Also I would like to thank the sub-referees Dr. Keiichi Maeda, Dr. Nobuyuki Hasebe, Dr. Masaki Mori for helpful comments and evaluating my thesis.

I would like to thank Ozawa-san for helping me in getting familiarized with the lab workstations and the restaurants nearby. During the first 3 years in our laboratory I made three amazing friends- Murata-san, Saitou-san and Kimura-san, and it was just so fun to play soccer or hang around in the nearby sports centers after a hard day's work. JICA provided my scholarship to stay and fund my studies in Japan and I cannot thank them enough. Makiko-san, my first JICA cordinator helped me in making first bank account and getting adopted in and around Tokyo. Even though at the beginning it was tough to get accustomed, Motz-san, Makiko-san and Anju helped me in believing that things will get easier. It would be difficult to name all my friends who have helped me always, but Aakash, Tigu, Tanimadi were there through ups and downs. Medical coordinator Shirakaki san helped me a lot when I fractured my ankle and eventually she became one of my best guides

in Japan. Lindsey helped a lot to cope with pressure during the last days of thesis writing. It is so difficult to mention all the kind people I met around our lab, but it would be a mistake to not to thank the obachan in Fujiya shop, where eating dinner felt more like a trip back home.

On a personal note I cannot express the gratitude I have for my parents for supporting and encouraging me always even they are very far away. They were available for me at every single instant when I needed someone to talk to. I adored the PhD process, as in past 5 years it made me realize the virtues of hard work, perseverance and gratitude in life, which will surely help me on a longer run.

# Bibliography


[1] V. S. Ptuskin, S. I. Rogovaya, V. N. Zirakashvili, L. G. Chuvilgin, G. B. Khristiansen, et al., *Diffusion and drift of very high energy cosmic rays in galactic magnetic fields*, *Astron. Astrophys.* **268** (1993) 726.

[2] L. O. Drury, *Origin of Cosmic Rays*, *Astropart. Phys.* **39-40** (2012) 52–60, [arXiv:1203.3681].

[3] L. O. Drury, *An introduction to the theory of diffusive shock acceleration of energetic particles in tenuous plasmas*, *Reports on Progress in Physics* **46** (1983), no. 8 973.

[4] M. S. Longair, *High Energy Astrophysics*. Cambridge University Press, third ed., 2011.

[5] S. Reinhard, *Cosmic Ray Astrophysics*. Springer, second ed., 2003.

[6] **Fermi-LAT** Collaboration, W. B. Atwood et al., *The Large Area Telescope on the Fermi Gamma-ray Space Telescope Mission*, *Astrophys. J.* **697** (2009) 1071–1102, [arXiv:0902.1089].

[7] M. Casolino et al., *Launch of the Space experiment PAMELA*, *Adv. Space Res.* **42** (2008) 455–466, [arXiv:0708.1808].

[8] **AMS** Collaboration, M. Aguilar et al., *First Result from the Alpha Magnetic Spectrometer on the International Space Station: Precision Measurement of the Positron Fraction in Primary Cosmic Rays of 0.5350 GeV*, *Phys. Rev. Lett.* **110** (2013) 141102.

[9] **CALET** Collaboration, S. Tori, *The CALorimetric Electron Telescope (CALET) on the ISS: Preliminary Results from On-orbit Observations since October, 2015*, *PoS* **ICRC2017** (2018) 1092.

[10] H. Ahn et al., *The Cosmic Ray Energetics and Mass (CREAM) instrument*, *Nucl. Instrum. and Methods* **579** (2007) 1034.

[11] M. Ave and others, *Composition of Primary Cosmic-Ray Nuclei at High Energies*, *Astrophys. J* **678** (2008), no. 1 262.

[12] V. Ptuskin, V. Zirakashvili, and E.-S. Seo, *Spectra of Cosmic Ray Protons and Helium Produced in Supernova Remnants*, *Astrophys. J.* **763** (2013) 47, [arXiv:1212.0381].

[13] W. R. Webber, *A new estimate of the local interstellar energy density and ionization rate of galactic cosmic cosmic rays*, *Astrophys. J* **506** (1998), no. 1 329.

[14] K. G. Thomas, *Cosmic Rays and Particle Physics*. Cambridge University Press, first ed., 1990.

[15] **Fermi-LAT** Collaboration, M. Ackermann et al., *Detection of the Characteristic Pion-Decay Signature in Supernova Remnants*, *Science* **339** (2013) 807, [arXiv:1302.3307].

[16] A. R. Bell, *The acceleration of cosmic rays in shock fronts  I*, *Mon. Not. Roy. Astron. Soc.* **182** (1978), no. 2 147.

[17] E. Fermi, *On the origin of the cosmic radiation*, *Phys. Rev.* **75** (Apr, 1949) 1169–1174.

[18] T. Stanev, *High Energy Cosmic Rays*. Springer, second ed., 2009.

[19] P. Lagage and C. Cesarsky, *The maximum energy of cosmic rays accelerated by supernova shocks*, *Astron. Astrophys.* **125** (1983) 249–257.

[20] E. Herbst, *Chemistry in the interstellar medium*, *Annual Review of Physical Chemistry* **46** (1995) 27–54.

[21] P. M. Kalberla and J. Kerp, *The HI Distribution of the Milky Way*, *Ann. Rev. of Astron. and Astrophys.* **47** (2009) 27–61.

[22] Y. Sofue, *A Grand Rotation Curve and Dark Matter Halo in the Milky Way Galaxy*, *Publ. Astron. Soc. Jap.* **64** (2012) 75, [arXiv:1110.4431].

[23] Y. Sofue, M. Fujimoto, and R. Wielebinski, *Global Structure of Magnetic Fields in Spiral Galaxies*, *Ann. Rev. of Astron. and Astrophys.* **24** (1986) 459–497.

[24] X. H. Sun, W. Reich, A. Waelkens, and T. Enslin, *Radio observational constraints on Galactic 3D-emission models*, *Astron. Astrophys.* **477** (2008) 573, [arXiv:0711.1572].

[25] Andrew W. Strong and Igor V. Moskalenko and Olaf Reimer, *Diffuse Continuum Gamma Rays from the Galaxy*, *Astrophys. J.* **537** (2000), no. 2 763.

[26] R. Cowsik, Y. Pal, S. N. Tandon, and R. P. Verma, *Steady state of cosmic-ray nuclei¯their spectral shape and path length at low energies*, *Phys. Rev.* **158** (Jun, 1967) 1238–1242.

[27] J. Engelmann, P. Ferrando, A. Soutoul, P. Goret, and E. Juliusson, *Charge Composition and Energy Spectra of Cosmic-Ray Nuclei for Elements from Be to Ni- Results from HEACO-3*, *Astron. Astrophys.* **233** (July, 1990) 96–111.

[28] M. A. Duvernois, J. A. Simpson, and M. R. Thayer, *Interstellar propagation of cosmic rays: analysis of the ulysses primary and secondary elemental abundances*, *Astron. Astrophys.* **316** (1996) 555–563.

[29] A. Panov, N. Sokolskaya, and V. Zatsepin, *Upturn in the ratio of nuclei of $Z = 16 - 24$ to iron observed in the ATIC experiment and the Local Bubble*, *Nuclear Physics B - Proceedings Supplements* **256** (2014) 233 – 240. Cosmic Ray Origin  Beyond the Standard Models.

[30] M. Garcia-Munoz, J. Simpson, T. Guzik, J. Wefel, and S. Margolis, *Cosmic-ray propagation in the galaxy and in the heliosphere-the path-length distribution at low energy*, *Astrophys. J. Suppl.* **64** (May, 1987) 269–304.

[31] R. A. Leske, *The elemental and isotopic composition of galactic cosmic-ray nuclei from scandium through nickel*, *Astrophys. J.* **405** (1993), no. 2 567–583.

[32] M. Garcia-Munoz, G. M. Mason, and J. A. Simpson, *The Isotopic Composition of Galactic Cosmic-Ray Beryllium and the Cosmic Ray Age*, in *Proceedings, 15th International Cosmic Ray Conference (ICRC 1977): Plovdiv, Bulgaria, August 13-26, 1977*, vol. 1, pp. 307–312, 1978.

[33] A. W. Strong and I. V. Moskalenko, *Propagation of cosmic-ray nucleons in the galaxy*, *Astrophys. J.* **509** (1998) 212–228, [astro-ph/9807150].

[34] A. W. Strong, I. V. Moskalenko, and V. S. Ptuskin, *Cosmic-ray propagation and interactions in the Galaxy*, *Ann. Rev. Nucl. Part. Sci.* **57** (2007) 285–327, [astro-ph/0701517].

[35] P. Goldreich and S. Sridhar, *Toward a Theory of Interstellar Turbulence. II: Strong Alfvenic Turbulence*, *Astrophys. J.* **438** (1995) 763–775.

[36] H. Yan and A. Lazarian, *Cosmic ray scattering and streaming in compressible magnetohydrodynamic turbulence*, *Astrophys. J.* **614** (2004) 757–769, [astro-ph/0408172].

[37] E. S. Seo and V. S. Ptuskin, *Stochastic reacceleration of cosmic rays in the interstellar medium*, *Astrophys. J.* **438** (1994) 705–714.

[38] E. C. Stone, A. C. Cummings, F. B. McDonald, B. C. Heikkila, N. Lal, and W. R. Webber, *Voyager 1 Observes Low-Energy Galactic Cosmic Rays in a Region Depleted of Heliospheric Ions*, *Science* **341** (2012) 150–153.

[39] E. N. Parker, *Dynamics of the Interplanetary Gas and Magnetic Fields*, *Astrophys. J.* **128** (1958) 664–676.

[40] E. Parker, *The passage of energetic charged particles through interplanetary space*, *Planetary and Space Science* **13** (1965), no. 1 9 – 49.

[41] L. J. Gleeson and W. I. Axford, *Solar modulation of galactic cosmic rays*, *Astrophys. J.* **154** (1968) 1011.

[42] C. J. Mertens et al., *Influence of Space Weather on Aircraft Ionizing Radiation Exposure*, in *Aerospace Sciences Meeting and Exhibit*, 2008.

[43] Y. Shimizu et al., *Balloon borne experiment with CALET prototype*, *J. Phys. Soc. Jpn.* **78** (2009) 165–168.

[44] **CALET** Collaboration, S. Torii, *The CALorimetric Electron Telescope (CALET): a High-Energy Astroparticle Physics Observatory on the International Space Stati*, *PoS* **ICRC2015** (2016) 581.

[45] **CALET** Collaboration, O. Adriani et al., *Energy Spectrum of Cosmic-Ray Electron and Positron from 10 GeV to 3 TeV Observed with the Calorimetric Electron Telescope on the International Space Station*, *Phys. Rev. Lett.* **119** (Nov, 2017) 181101.

[46] T. Guzik et al., *The ATIC long duration*, *Adv. Space Res.* **33** (2004) 1763.

[47] J. Chang, *Dark Matter Particle Explorer, The First Chinese Cosmic Ray and Hard $\gamma$-ray Detector in Space*, *Chinese Journal of Space Science* **34** (2014) 550.

[48] **DAMPE** Collaboration, A. G. et al., *Direct detection of a break in the teraelectronvolt cosmic-ray spectrum of electrons and positrons*, *Nature* **553** (2017) 63–66.

[49] **Pierre Auger** Collaboration, *Observation of large-scale anisotropy in the arrival directions of cosmic rays above* $8 \times 10^{18}$ *eV*, *Science* **357** (2017) 1266.

[50] J. R. Horandel, *A Review of experimental results at the knee*, *J. Phys. Conf. Ser.* **47** (2006) 41–50.

[51] Y. Asaoka et al., *Energy calibration of CALET onboard the International Space Station*, *Astropart. Phys.* **91** (2017) 1–10.

[52] **CALET** Collaboration, B. F. Rauch, *Predicted CALET Measurements of Heavy and Ultra-Heavy Cosmic Ray Nuclei*, *PoS* **ICRC2015** (2016) 627.

[53] N. W. Cannady and M. L. Cherry, *Gamma-Ray Observations with CALET: Exposure Map, Response Functions, and Simulated Results*, *PoS* **ICRC2015** (2016) 995.

[54] O. Adriani et al., *CALET Upper Limits on X-ray and Gamma-ray Counterparts of GW 151226*, *Astrophys. J.* **829** (2016), no. 1 L20, [arXiv:1607.00233].

[55] Y. Asaoka, *Development of the Waseda CALET Operations Center (WCOC) for Scientific Operations of CALET*, *PoS* **ICRC2015** (2016) 603.

[56] K. Yamaoka, *CALET Gamma-ray Burst Monitor (CGBM)*, *PoS* **ICRC2013** (2013) 1007.

[57] T. Kobayashi, Y. Komori, K. Yoshida, and J. Nishimura, *The most likely sources of high energy cosmic-ray electrons in supernova remnants*, *Astrophys. J.* **601** (2004) 340–351, [astro-ph/0308470].

[58] B. Aschenbach, *Discovery of a young nearby supernova remnant*, *Nature* **396** (1998) 141–142.

[59] J. P. W. Verbiest, J. M. Weisberg, A. A. Chael, K. J. Lee, and D. R. Lorimer, *On Pulsar Distance Measurements and their Uncertainties*, *Astrophys. J.* **755** (2012) 39, [arXiv:1206.0428].

[60] J. Nishimura et al., *Emulsion chamber observations of primary cosmic-ray electrons in the energy range 30-1000 GeV*, *Astrophys. J.* **238** (1980) 394–409.

[61] Atoyan, A. M. and others, *Electrons and positrons in the galactic cosmic rays*, *Phys. Rev. D* **52** (Sep, 1995) 3265.

[62] C. S. Shen and C. Y. Mao, *Anisotropy of high energy cosmic-ray electrons in the discrete source model*, *Astrophys. J. Lett.* **9** (1971) 169.

[63] **AMS** Collaboration, M. Aguilar et al., *Precision Measurement of the Proton Flux in Primary Cosmic Rays from Rigidity 1 GV to 1.8 TV with the Alpha Magnetic Spectrometer on the International Space Station*, *Phys. Rev. Lett.* **114** (2015) 171103.

[64] **AMS** Collaboration, M. Aguilar et al., *Electron and Positron Fluxes in Primary Cosmic Rays Measured with the Alpha Magnetic Spectrometer on the International Space Station*, *Phys. Rev. Lett.* **113** (2014) 121102.

[65] J. Chang et al., *An excess of cosmic ray electrons at energies of 300-800 GeV*, *Nature* **456** (2008) 362–365.

[66] **PAMELA** Collaboration, O. Adriani et al., *An anomalous positron abundance in cosmic rays with energies 1.5-100 GeV*, *Nature* **458** (2009) 607–609, [arXiv:0810.4995].

[67] M. Kruskal, S. P. Ahlen, and G. Tarl, *Secondary Production as the Origin of the Cosmic-ray Positron Excess*, *Astrophys. J.* **818** (2016), no. 1 70, [arXiv:1410.7239].

[68] K. Yoshida, *The science objectives for CALET*, in *Proceedings, 32nd International Cosmic Ray Conference (ICRC 2011): Beijing, China, August 11-18, 2011*, vol. 6, p. 367, 2011.

[69] **Fermi-LAT** Collaboration, S. Abdollahi et al., *Cosmic-ray electron-positron spectrum from 7 GeV to 2 TeV with the Fermi Large Area Telescope*, *Phys. Rev.* **D95** (2017), no. 8 082007, [arXiv:1704.07195].

[70] **Virgo, LIGO Scientific** Collaboration, B. P. Abbott et al., *GW151226: Observation of Gravitational Waves from a 22-Solar-Mass Binary Black Hole Coalescence*, *Phys. Rev. Lett.* **116** (2016), no. 24 241103, [arXiv:1606.04855].

[71] O. Adriani et al., *The CALorimetric Electron Telescope (CALET) for high-energy astroparticle physics on the International Space Station*, *J. Phys. Conf. Ser.* **632** (2015), no. 1 012023.

[72] F. Zwicky, *On the masses of nebulae and clusters of nebulae*, *Astrophys. J.* **86** (1937) 217.

[73] V. C. Rubin and J. Ford, W. Kent, *Rotation of the andromeda nebula from a spectroscopic survey of emission regions*, *Astrophys. J.* **159** (February, 1970) 379.

[74] E. Corbelli and P. Salucci, *The Extended Rotation Curve and the Dark Matter Halo of M33*, *Mon. Not. Roy. Astron. Soc.* **311** (2000) 441–447, [astro-ph/9909252].

[75] Y. Sofue and V. Rubin, *Rotation curves of spiral galaxies*, *Ann. Rev. Astron. Astrophys.* **39** (2001) 137–174, [astro-ph/0010594].

[76] D. P. Roy, *Basic constituents of the visible and invisible matter: A Microscopic view of the universe*, physics/0007025.

[77] R. Massey et al., *Dark matter maps reveal cosmic scaffolding*, *Nature* **445** (2007) 286, [astro-ph/0701594].

[78] J. A. Tyson, G. P. Kochanski, and I. P. Dell'Antonio, *Detailed mass map of CL0024+1654 from strong lensing*, *Astrophys. J.* **498** (1998) L107, [astro-ph/9801193].

[79] **EROS-2** Collaboration, P. Tisserand et al., *Limits on the Macho Content of the Galactic Halo from the EROS-2 Survey of the Magellanic Clouds*, *Astron. Astrophys.* **469** (2007) 387–404, [astro-ph/0607207].

[80] D. S. Graff and K. Freese, *Analysis of a hubble space telescope search for red dwarfs: limits on baryonic matter in the galactic halo*, *Astrophys. J.* **456** (1996) L49, [astro-ph/9507097].

[81] **WMAP** Collaboration, G. Hinshaw et al., *Nine-Year Wilkinson Microwave Anisotropy Probe (WMAP) Observations: Cosmological Parameter Results*, *Astrophys. J. Suppl.* **208** (2013) 19, [arXiv:1212.5226].

[82] **Planck** Collaboration, P. A. R. Ade et al., *Planck 2015 results. XIII. Cosmological parameters*, *Astron. Astrophys.* **594** (2016) A13, [arXiv:1502.01589].

[83] **SDSS** Collaboration, M. Tegmark et al., *The 3-D power spectrum of galaxies from the SDSS*, *Astrophys. J.* **606** (2004) 702–740, [astro-ph/0310725].

[84] **HST** Collaboration, W. L. Freedman et al., *Final results from the Hubble Space Telescope key project to measure the Hubble constant*, *Astrophys. J.* **553** (2001) 47–72, [astro-ph/0012376].

[85] D. Clowe, M. Bradac, A. H. Gonzalez, M. Markevitch, S. W. Randall, C. Jones, and D. Zaritsky, *A direct empirical proof of the existence of dark matter*, *Astrophys. J.* **648** (2006) L109–L113, [astro-ph/0608407].

[86] V. Springel et al., *Simulating the joint evolution of quasars, galaxies and their large-scale distribution*, *Nature* **435** (2005) 629–636, [astro-ph/0504097].

[87] J. Diemand, M. Kuhlen, P. Madau, M. Zemp, B. Moore, D. Potter, and J. Stadel, *Clumps and streams in the local dark matter distribution*, *Nature* **454** (2008) 735–738, [arXiv:0805.1244].

[88] **Supernova Cosmology Project** Collaboration, R. A. Knop et al., *New constraints on Omega(M), Omega(lambda), and w from an independent set of eleven high-redshift supernovae observed with HST*, *Astrophys. J.* **598** (2003) 102, [astro-ph/0309368].

[89] S. D. M. White, C. S. Frenk, and M. Davis, *Clustering in a Neutrino Dominated Universe*, *Astrophys. J.* **274** (1983) L1–L5.

[90] S. Hannestad, A. Mirizzi, G. G. Raffelt, and Y. Y. Y. Wong, *Neutrino and axion hot dark matter bounds after WMAP-7*, *JCAP* **1008** (2010) 001, [arXiv:1004.0695].

[91] E. Gerhard and N. Spergel, *Dwarf spheroidal galaxies and the mass of neutrino*, *Astrophys. J.* **389** (April, 1992) L9–L11.

[92] W. K. Edward and M. Turner, *Early Universe*. Addison-Wesley, first ed., 1990.

[93] L. Bergstrm, *Nonbaryonic dark matter: Observational evidence and detection methods*, *Rept. Prog. Phys.* **63** (2000) 793, [hep-ph/0002126].

[94] G. Jungman, M. Kamionkowski, and K. Griest, *Supersymmetric dark matter*, *Phys. Rept.* **267** (1996) 195–373, [hep-ph/9506380].

[95] H. Chiu, *Symmetry between particle and antiparticle populations in the universe*, *Phys. Rev. Lett.* **17** (Sep, 1966) 712–714.

[96] F. Halzen and A. Martin, *Quarks and Leptons: An Introductory Course in Modern Particle Physics*. John Wiley and Sons., first ed., 1984.

[97] G. Servant and T. M. P. Tait, *Is the lightest Kaluza-Klein particle a viable dark matter candidate?*, *Nucl. Phys.* **B650** (2003) 391–419, [hep-ph/0206071].

[98] D. Hooper and G. D. Kribs, *Kaluza-Klein dark matter and the positron excess*, *Phys. Rev.* **D70** (2004) 115004, [hep-ph/0406026].

[99] E. W. Kolb et al., *WIMPzillas!*, in *Trends in theoretical physics II. Proceedings, 2nd La Plata Meeting, Argentina, November*, pp. 91–105, 1998. hep-ph/9810361.

[100] J. L. Feng and J. Kumar, *The WIMPless Miracle: Dark-Matter Particles without Weak-Scale Masses or Weak Interactions*, *Phys. Rev. Lett.* **101** (2008) 231301, [arXiv:0803.4196].

[101] D. P. Finkbeiner and N. Weiner, *Exciting Dark Matter and the INTEGRAL/SPI 511 keV signal*, *Phys. Rev.* **D76** (2007) 083519, [astro-ph/0702587].

[102] K. N. Abazajian et al., *Light Sterile Neutrinos: A White Paper*, arXiv:1204.5379.

[103] A. Boyarsky, O. Ruchayskiy, and M. Shaposhnikov, *The Role of sterile neutrinos in cosmology and astrophysics*, *Ann. Rev. Nucl. Part. Sci.* **59** (2009) 191–214, [arXiv:0901.0011].

[104] Weinberg, S., *A New Light Boson?*, *Phys. Rev. Lett.* **40** (Jan, 1978) 223–226.

[105] Preskill, J. and Wise, Mark B. and Wilczek, F., *Cosmology of the invisible axion*, *Phys. Lett. B.* **120** (1983) 127–132.

[106] L. Visinelli and P. Gondolo, *Dark Matter Axions Revisited*, *Phys. Rev.* **D80** (2009) 035024, [arXiv:0903.4377].

[107] M. Battaglia, I. Hinchliffe, and D. Tovey, *Cold dark matter and the lhc*, *Journal of Physics G: Nuclear and Particle Physics* **30** (2004), no. 10 R217.

[108] E. A. Baltz, M. Battaglia, M. E. Peskin, and T. Wizansky, *Determination of dark matter properties at high-energy colliders*, *Phys. Rev.* **D74** (2006) 103521, [hep-ph/0602187].

[109] J. D. Lewin and P. F. Smith, *Review of mathematics, numerical factors, and corrections for dark matter experiments based on elastic nuclear recoil*, *Astropart. Phys.* **6** (1996) 87–112.

[110] K. Freese, M. Lisanti, and C. Savage, *Colloquium: Annual modulation of dark matter*, *Rev. Mod. Phys.* **85** (2013) 1561–1581, [arXiv:1209.3339].

[111] **DAMA** Collaboration, R. Bernabei et al., *First results from DAMA/LIBRA and the combined results with DAMA/NaI*, *Eur. Phys. J.* **C56** (2008) 333–355, [arXiv:0804.2741].

[112] M. Teresa and R. Ludwig, *Dark matter direct-detection experiments*, *J. Phys.* **G43** (2016), no. 1 013001, [arXiv:1509.08767].

[113] P. Salati, F. Donato, and N. Fornengo, *Indirect Dark Matter Detection with Cosmic Antimatter*, arXiv:1003.4124.

[114] A. Ibarra, D. Tran, and C. Weniger, *Indirect Searches for Decaying Dark Matter*, *Int. J. Mod. Phys.* **A28** (2013) 1330040, [arXiv:1307.6434].

[115] T. Sjostrand, S. Mrenna, and P. Z. Skands, *A Brief Introduction to PYTHIA 8.1*, *Comput. Phys. Commun.* **178** (2008) 852–867, [arXiv:0710.3820].

[116] M. Cirelli, G. Corcella, A. Hektor, G. Hutsi, M. Kadastik, P. Panci, M. Raidal, F. Sala, and A. Strumia, *PPPC 4 DM ID: A Poor Particle Physicist Cookbook for Dark Matter Indirect Detection*, *JCAP* **1103** (2011) 051, [arXiv:1012.4515]. [Erratum: JCAP1210,E01(2012)].

[117] L. Bergstrom and J. Kaplan, *Gamma-ray lines from TeV dark matter*, *Astropart. Phys.* **2** (1994) 261–268, [hep-ph/9403239].

[118] P. Ullio and L. Bergstrom, *Neutralino annihilation into a photon and a Z boson*, *Phys. Rev.* **D57** (1998) 1962–1971, [hep-ph/9707333].

[119] C. Rott, *Status of Dark Matter Searches (Rapporteur Talk)*, arXiv:1712.00666. [PoSICRC2017,1119(2017)].

[120] *Searches for annihilating dark matter in the Milky Way halo with IceCube*, . [PoSICRC2017,906(2017)].

[121] **Fermi-LAT** Collaboration, V. Vitale and A. Morselli, *Indirect Search for Dark Matter from the center of the Milky Way with the Fermi-Large Area Telescope*, in *Fermi gamma-ray space telescope. Proceedings, 2nd Fermi Symposium, Washington, USA, November 2-5, 2009*, 2009. arXiv:0912.3828.

[122] **H.E.S.S.** Collaboration, F. Acero, *Localising the VHE gamma-ray source at the Galactic Centre*, *Mon. Not. Roy. Astron. Soc.* **402** (2010) 1877–1882, [arXiv:0911.1912].

[123] F. Stoehr, S. D. M. White, V. Springel, G. Tormen, and N. Yoshida, *Dark matter annihilation in the halo of the Milky Way*, *Mon. Not. Roy. Astron. Soc.* **345** (2003) 1313, [astro-ph/0307026].

[124] A. W. Graham et al., *Empirical models for Dark Matter Halos. I. Nonparametric Construction of Density Profiles and Comparison with Parametric Models*, *Astron. J.* **132** (2006) 2685–2700, [astro-ph/0509417].

[125] J. F. Navarro et al., *The Diversity and Similarity of Cold Dark Matter Halos*, *Mon. Not. Roy. Astron. Soc.* **402** (2010) 21, [arXiv:0810.1522].

[126] K. G. Begeman, A. H. Broeils, and R. H. Sanders, *Extended rotation curve for spiral galaxies-dark haloes and modified dynamics*, *Mon. Not. Roy. Astron. Soc.* **249** (1991) 523–537.

[127] A. Burkert, *The Structure of dark matter halos in dwarf galaxies*, *IAU Symp.* **171** (1996) 175, [astro-ph/9504041]. [Astrophys. J.447,L25(1995)].

[128] J. Diemand, B. Moore, and J. Stadel, *Convergence and scatter of cluster density profiles*, *Mon. Not. Roy. Astron. Soc.* **353** (2004) 624, [astro-ph/0402267].

[129] J. F. Navarro, C. S. Frenk, and S. D. M. White, *A Universal density profile from hierarchical clustering*, *Astrophys. J.* **490** (1997) 493–508, [astro-ph/9611107].

[130] E. L. Lokas and G. A. Mamon, *Properties of spherical galaxies and clusters with an nfw density profile*, *Mon. Not. Roy. Astron. Soc.* **321** (2001) 155, [astro-ph/0002395].

[131] W. Dehnen, D. McLaughlin, and J. Sachania, *The velocity dispersion and mass profile of the milky way*, *Mon. Not. Roy. Astron. Soc.* **369** (2006) 1688–1692, [astro-ph/0603825].

[132] M. Boudaud, M. Cirelli, G. Giesen, and P. Salati, *A fussy revisitation of antiprotons as a tool for Dark Matter searches*, *JCAP* **1505** (2015), no. 05 013, [arXiv:1412.5696].

[133] S. Thoudam and J. R. Horandel, *On the point source approximation of nearby cosmic-ray sources*, *Mon. Not. Roy. Astron. Soc.* **419** (2012) 624, [arXiv:1109.5588].

[134] Y. Genolini, A. Putze, P. Salati, and P. D. Serpico, *Theoretical uncertainties in extracting cosmic-ray diffusion parameters: the boron-to-carbon ratio*, *Astron. Astrophys.* **580** (2015) A9, [arXiv:1504.03134].

[135] T. Delahaye, J. Lavalle, R. Lineros, F. Donato, and N. Fornengo, *Galactic electrons and positrons at the Earth:new estimate of the primary and secondary fluxes*, *Astron. Astrophys.* **524** (2010) A51, [arXiv:1002.1910].

[136] D. Maurin, F. Donato, R. Taillet, and P. Salati, *Cosmic rays below z=30 in a diffusion model: new constraints on propagation parameters*, *Astrophys. J.* **555** (2001) 585–596, [astro-ph/0101231].

[137] M. Boudaud, E. F. Bueno, S. Caroff, Y. Genolini, V. Poulin, V. Poireau, A. Putze, S. Rosier, P. Salati, and M. Vecchi, *The pinching method for Galactic cosmic ray positrons: implications in the light of precision measurements*, *Astron. Astrophys.* **605** (2017) A17, [arXiv:1612.03924].

[138] T. Delahaye, F. Donato, N. Fornengo, J. Lavalle, R. Lineros, P. Salati, and R. Taillet, *Galactic secondary positron flux at the Earth*, *Astron. Astrophys.* **501** (2009) 821–833, [arXiv:0809.5268].

[139] E. A. Baltz and J. Edsjo, *Positron propagation and fluxes from neutralino annihilation in the halo*, *Phys. Rev.* **D59** (1998) 023511, [astro-ph/9808243].

[140] M. Boudaud et al., *A new look at the cosmic ray positron fraction*, *Astron. Astrophys.* **575** (2015) A67, [arXiv:1410.3799].

[141] A. E. Vladimirov, S. W. Digel, G. Johannesson, P. F. Michelson, I. V. Moskalenko, P. L. Nolan, E. Orlando, T. A. Porter, and A. W. Strong, *GALPROP WebRun: an internet-based service for calculating galactic cosmic ray propagation and associated photon emissions*, *Comput. Phys. Commun.* **182** (2011) 1156–1161, [arXiv:1008.3642].

[142] D. Gaggero, L. Maccione, G. Di Bernardo, C. Evoli, and D. Grasso, *Three-Dimensional Model of Cosmic-Ray Lepton Propagation Reproduces Data from the Alpha Magnetic Spectrometer on the International Space Station*, *Phys.Rev.Lett.* **111** (2013), no. 2 021102, [arXiv:1304.6718].

[143] J. Crank and P. Nicolson, *A practical method for numerical evaluation of solutions of partial differential equations of the heat-conduction type*, *Advances in Computational Mathematics* **6** (Dec, 1996) 207.

[144] A. W. Strong, 2011. GALPROP Version 54: Explanatory Supplement.

[145] D. J. Thompson, *Gamma ray astrophysics: the EGRET results*, *Rept. Prog. Phys.* **71** (2008) 116901, [arXiv:0811.0738].

[146] M. A. Gordon and W. B. Burton, *Carbon monoxide in the Galaxy. I - The radial distribution of CO, $H_2$, and nucleons*, *Astrophys. J.* **208** (1976) 346–353.

[147] I. V. Moskalenko and A. W. Strong, *Production and propagation of cosmic ray positrons and electrons*, *Astrophys. J.* **493** (1998) 694–707, [astro-ph/9710124].

[148] T. A. Porter and A. W. Strong, *A New estimate of the Galactic interstellar radiation field between 0.1 microns and 1000 microns*, in *29th International Cosmic Ray Conference (ICRC 2005) Pune, India, August 3-11, 2005*, p. 77, 2005. astro-ph/0507119. [4,77(2005)].

[149] G. Corcella et al., *HERWIG 6: An Event generator for hadron emission reactions with interfering gluons (including supersymmetric processes)*, *JHEP* **01** (2001) 010, [hep-ph/0011363].

[150] G. Belanger et al., *micrOMEGAs 3: A program for calculating dark matter observables*, *Comput. Phys. Commun.* **185** (2014) 960–985, [arXiv:1305.0237].

[151] G. Belanger et al., *Indirect search for dark matter with micrOMEGAs 2.4*, *Comput. Phys. Commun.* **182** (2011) 842–856, [arXiv:1004.1092].

[152] M. W. Werner and others, *The Spitzer Space Telescope Mission*, *Astrophys. J* **154** (2004), no. 1.

[153] Ed Churchwell and others, *The Spitzer/GLIMPSE Surveys: A New View of the Milky Way*, *Publications of the Astronomical Society of the Pacific* **121** (2009), no. 877 213.

[154] J. C. Higdon and R. E. Lingenfelter, *The Galactic Spatial Distribution of OB Associations and their Surrounding Supernova-generated Superbubbles*, *Astrophys. J.* **775** (2013) 110, [arXiv:1302.1223].

[155] Steiman-Cameron, T. and Wolfire, M. and Hollenbach, D., *COBE and the Galactic Interstellar Medium: Geometry of the Spiral Arms from FIR Cooling Lines*, *Astrophys. J.* **722** (2010), no. 2 1460.

[156] M. Werner, R. Kissmann, A. W. Strong, and O. Reimer, *Spiral Arms as Cosmic Ray Source Distributions*, *Astropart. Phys.* **64** (2015) 18–33, [arXiv:1410.5266].

[157] Jacques P. Valle, *The Spiral Arms and Interarm Separation of the Milky Way: An Updated Statistical Study*, *Astron. J.* **130** (2005), no. 2 569.

[158] Y. Xu, M. Reid, X. W. Zheng, and K. M. Menten, *The distance to the perseus spiral arm in the milky way*, *Science* **311** (2006) 54–57.

[159] T. Kaluza, *On the Problem of Unity in Physics*, *Sitzungsber. Preuss. Akad. Wiss. Berlin (Math. Phys.)* **1921** (1921) 966–972.

[160] O. Klein, *Quantentheorie und fünfdimensionale Relativitätstheorie*, *Zeitschrift für Physik* **37** (Dec, 1926) 895–906.

[161] K. Kong and K. T. Matchev, *Precise calculation of the relic density of Kaluza-Klein dark matter in universal extra dimensions*, *JHEP* **01** (2006) 038, [hep-ph/0509119].

[162] **AMS** Collaboration, M. Aguilar et al., *Precision Measurement of the $(e^+ + e)$ Flux in Primary Cosmic Rays from 0.5 GeV to 1 TeV with the Alpha Magnetic Spectrometer on the International Space Station*, *Phys. Rev. Lett.* **113** (2014) 221102.

[163] J. Lavalle and P. Salati, *Dark Matter Indirect Signatures*, *Comptes Rendus Physique* **13** (2012) 740–782, [arXiv:1205.1004].

[164] Adriani, O. and others, *PAMELA Results on the Cosmic-Ray Antiproton Flux from 60 MeV to 180 GeV in Kinetic Energy*, *Phys. Rev. Lett.* **105** (Sep, 2010) 121101.

[165] **AMS** Collaboration, Accardo, L. and others, *High Statistics Measurement of the Positron Fraction in Primary Cosmic Rays of 0.5˘500 GeV with the Alpha Magnetic Spectrometer on the International Space Station*, *Phys. Rev. Lett.* **113** (Sep, 2014) 121101.

[166] **Fermi LAT Collaboration** Collaboration, Ackermann, M. others, *Measurement of Separate Cosmic-Ray Electron and Positron Spectra with the Fermi Large Area Telescope*, *Phys. Rev. Lett.* **108** (Jan, 2012) 011103.

[167] D. Hooper, P. Blasi, and P. D. Serpico, *Pulsars as the Sources of High Energy Cosmic Ray Positrons*, *JCAP* **0901** (2009) 025, [arXiv:0810.1527].

[168] Malyshev, D. and Cholis, I. and Gelfand, J., *Pulsars versus dark matter interpretation of ATIC/PAMELA*, *Phys. Rev. D* **80** (Sep, 2009) 063005.

[169] S. Profumo, *Dissecting cosmic-ray electron-positron data with Occams razor: the role of known pulsars*, *Open Physics* **10** (2012).

[170] M. Cirelli, M. Kadastik, M. Raidal, and A. Strumia, *Model-independent implications of the e+-, anti-proton cosmic ray spectra on properties of Dark Matter*, *Nucl. Phys.* **B813** (2009) 1–21, [arXiv:0809.2409]. [Addendum: Nucl. Phys.B873,530(2013)].

[171] Bergstrom, L. and Bringmann, T. and Edsjo, J., *New positron spectral features from supersymmetric dark matter: A way to explain the PAMELA data?*, *Phys. Rev. D* **78** (Nov, 2008) 103520.

[172] I. Cholis, L. Goodenough, D. Hooper, M. Simet, and N. Weiner, *High Energy Positrons From Annihilating Dark Matter*, *Phys. Rev.* **D80** (2009) 123511, [arXiv:0809.1683].

[173] P.-f. Yin et al., *PAMELA data and leptonically decaying dark matter*, *Phys. Rev. D* **79** (Jan, 2009) 023512.

[174] P. J. Fox and E. Poppitz, *Leptophilic dark matter*, *Phys. Rev. D* **79** (Apr, 2009) 083528.

[175] Blasi, P., *Origin of the Positron Excess in Cosmic Rays*, *Phys. Rev. Lett.* **103** (Jul, 2009) 051104.

[176] G. Di Bernardo, C. Evoli, D. Gaggero, D. Grasso, L. Maccione, and M. N. Mazziotta, *Implications of the Cosmic Ray Electron Spectrum and Anisotropy measured with Fermi-LAT*, *Astropart. Phys.* **34** (2011) 528–538, [arXiv:1010.0174].

[177] Bergstrom, L. and Edsjo, J. and Zaharijas, G., *Dark matter interpretation of recent electron and positron data*, *Phys. Rev. Lett.* **103** (Jul, 2009) 031103.

[178] I. Cholis, G. Dobler, D. Finkbeiner, L. Goodenough, and N. Weiner, *The Case for a 700+ GeV WIMP: Cosmic Ray Spectra from ATIC and PAMELA*, *Phys. Rev.* **D80** (2009) 123518, [arXiv:0811.3641].

[179] J. Lavalle, Q. Yuan, D. Maurin, and X. J. Bi, *Full Calculation of Clumpiness Boost factors for Antimatter Cosmic Rays in the light of Lambda-CDM N-body simulation results. Abandoning hope in clumpiness enhancement?*, *Astron. Astrophys.* **479** (2008) 427–452, [arXiv:0709.3634].

[180] J. Lavalle, E. Nezri, E. Athanassoula, F. Ling, and R. Teyssier, *Antimatter cosmic rays from dark matter annihilation: First results from an N-body experiment*, *Phys. Rev.* **D78** (2008) 103526, [arXiv:0808.0332].

[181] J. Hisano, S. Matsumoto, and M. M. Nojiri, *Explosive dark matter annihilation*, *Phys. Rev. Lett.* **92** (2004) 031303, [hep-ph/0307216].

[182] M. Ibe, H. Murayama, and T. T. Yanagida, *Breit-Wigner Enhancement of Dark Matter Annihilation*, *Phys. Rev.* **D79** (2009) 095009, [arXiv:0812.0072].

[183] M. Cirelli, P. Panci, and P. D. Serpico, *Diffuse gamma ray constraints on annihilating or decaying Dark Matter after Fermi*, *Nucl. Phys.* **B840** (2010) 284–303, [arXiv:0912.0663].

[184] N. F. Bell and T. D. Jacques, *Gamma-ray Constraints on Dark Matter Annihilation into Charged Particles*, *Phys. Rev.* **D79** (2009) 043507, [arXiv:0811.0821].

[185] **AMS** Collaboration, M. Aguilar et al., *Antiproton Flux, Antiproton-to-Proton Flux Ratio, and Properties of Elementary Particle Fluxes in Primary Cosmic Rays Measured with the Alpha Magnetic Spectrometer on the International Space Station*, *Phys. Rev. Lett.* **117** (2016), no. 9 091103.

[186] Kevork N. A. and J. Patrick H., *Constraints on WIMP and Sommerfeld-enhanced dark matter annihilation from HESS observations of the galactic center*, *JCAP* **2012** (2012), no. 01 041.

[187] I. Cholis et al., *Diffuse Galactic Gamma Rays at intermediate and high latitudes. I. Constraints on the ISM properties*, *JCAP* **1205** (2012) 004, [arXiv:1106.5073].

[188] Ibarra, A. and Tran, D., *Gamma-Ray Spectrum from Gravitino Dark Matter Decay*, *Phys. Rev. Lett.* **100** (Feb, 2008) 061301.

[189] G. Bertone, W. Buchmuller, L. Covi, and A. Ibarra, *Gamma-Rays from Decaying Dark Matter*, *JCAP* **0711** (2007) 003, [arXiv:0709.2299].

[190] C.-R. Chen and F. Takahashi, *Cosmic rays from Leptonic Dark Matter*, *JCAP* **0902** (2009) 004, [arXiv:0810.4110].

[191] K. Kohri, A. Mazumdar, N. Sahu, and P. Stephens, *Probing Unified Origin of Dark Matter and Baryon Asymmetry at PAMELA/Fermi*, *Phys. Rev.* **D80** (2009) 061302, [arXiv:0907.0622].

[192] C.-R. Chen, F. Takahashi, and T. T. Yanagida, *Gamma rays and positrons from a decaying hidden gauge boson*, *Phys. Lett.* **B671** (2009) 71–76, [arXiv:0809.0792].

[193] **Fermi-LAT** Collaboration, M. Ackermann et al., *Fermi-LAT Observations of the Diffuse Gamma-Ray Emission: Implications for Cosmic Rays and the Interstellar Medium*, *Astrophys. J.* **750** (2012) 3, [arXiv:1202.4039].

[194] Cirelli, Marco and Moulin, Emmanuel and Panci, Paolo and Serpico, Pasquale D. and Viana, Aion, *Gamma ray constraints on decaying dark matter*, *Phys. Rev. D* **86** (Oct, 2012) 083506.

[195] S. Ando and K. Ishiwata, *Constraints on decaying dark matter from the extragalactic gamma-ray background*, *JCAP* **1505** (2015), no. 05 024, [arXiv:1502.02007].

[196] Ruderman, M. A. and Sutherland, P. G., *Theory of pulsars- Polar caps, sparks, and coherent microwave radiation*, *Astrophys. J.* **196** (1975) 51–72.

[197] J. Arons, *Pair creation above pulsar polar caps - Geometrical structure and energetics of slot gaps*, *Astrophys. J.* **266** (1983) 215–241.

[198] J. Takata and Y. Wang and K. S. Cheng, *Pulsar High Energy Emissions from Outer Gap Accelerator Closed by a Magnetic Pair-creation Process*, *Astrophys. J.* **715** (2010), no. 2 1318.

[199] L. Zhang and K. Cheng, *Cosmic-ray positrons from mature gamma-ray pulsars*, *Astron. Astrophys.* **368** (2001), no. 3.

[200] H. Motz, Y. Asaoka, S. Torii, and S. Bhattacharyya, *CALET's Sensitivity to Dark Matter Annihilation in the Galactic Halo*, *JCAP* **1512** (2015), no. 12 047, [arXiv:1510.03168].

[201] R. N. Manchester, G. B. Hobbs, A. Teoh, and M. Hobbs, *The Australia Telescope National Facility pulsar catalogue*, *Astron. J.* **129** (2005) 1993, [astro-ph/0412641].

[202] J. Feng and H.-H. Zhang, *Pulsar interpretation of lepton spectra measured by AMS-02*, *Eur. Phys. J.* **C76** (2016), no. 5 229, [arXiv:1504.03312].

[203] A. U. Abeysekara et al., *Extended gamma-ray sources around pulsars constrain the origin of the positron flux at Earth*, *Science* **358** (2017), no. 6365 911–914.

[204] I. Cernuda, *Cosmic ray electron anisotropies as a tool to discriminate between exotic and astrophysical sources*, *Astropart. Phys.* **34** (2010) 59–69, [arXiv:0905.1653].

[205] I. Buesching, O. C. de Jager, M. S. Potgieter, and C. Venter, *A Cosmic Ray Positron Anisotropy due to Two Middle-Aged, Nearby Pulsars?*, *Astrophys. J.* **678** (2008) L39–L42, [arXiv:0804.0220].

[206] S. Profumo, *An observable electron-positron anisotropy cannot be generated by dark matter*, *JCAP* **1502** (2015), no. 02 043, [arXiv:1405.4884].

[207] I. Cholis and D. Hooper, *Dark matter and pulsar origins of the rising cosmic ray positron fraction in light of new data from the ams*, *Phys. Rev. D* **88** (Jul, 2013) 023013.

[208] A. Ibarra, D. Tran, and C. Weniger, *Decaying Dark Matter in Light of the PAMELA and Fermi LAT Data*, *JCAP* **1001** (2010) 009, [arXiv:0906.1571].

[209] C. D. Carone, A. Cukierman, and R. Primulando, *On the Cosmic-Ray Spectra of Three-Body Lepton-Flavor-Violating Dark Matter Decays*, *Phys. Lett.* **B704** (2011) 541–546, [arXiv:1108.2084].

[210] K. Kohri and N. Sahu, *Constraining the cogenesis of visible and dark matter with AMS-02 and Xenon-100*, *Phys. Rev.* **D88** (2013) 103001, [arXiv:1306.5629].

[211] http://galprop.stanford.edu/.

[212] A. Neronov, D. V. Semikoz, and A. M. Taylor, *Low-energy break in the spectrum of galactic cosmic rays*, *Phys. Rev. Lett.* **108** (Jan, 2012) 051105.

[213] I. Cholis, D. Hooper, and T. Linden, *A Predictive Analytic Model for the Solar Modulation of Cosmic Rays*, *Phys. Rev.* **D93** (2016), no. 4 043016, [arXiv:1511.01507].

[214] Ando, S. and Ishiwata, K., *Constraints on decaying dark matter from the extragalactic gamma-ray background*, *JCAP* **1505** (2015), no. 05 024, [arXiv:1502.02007].

[215] Chang, J., *Dark Matter Particle Explorer, The First Chinese Cosmic Ray and Hard $\gamma$-ray Detector in Space*, *Chinese Journal of Space Science* **34** (2014) 550.

[216] **AMS** Collaboration, S. Ting, *The First Five Years of the Alpha Magnetic Spectrometer on the International Space Station*, 2016. https://indico.cern.ch/event/592392/.

[217] K. Belotsky, R. Budaev, A. Kirillov, and M. Laletin, *Fermi-lat kills dark matter interpretations of ams-02 data. or not?*, *JCAP* **2017** (2017), no. 01 021, [arXiv:1606.01271].

[218] Y. Akaike, K. Kasahara, and S. Torii, *Expected CALET Telescope Performance from Monte Carlo Simulations*, *PoS* **6** (2011) 371.

[219] Akaike.H, *A new look at the statistical model identification*, *IEEE* **19** (Dec 1974) 716–723.

[220] S. Torii et al., *The Energy Spectrum of Cosmic-Ray Electrons from 10 to 100 GeV Observed with a Highly Granulated Imaging Calorimeter*, *Astrophys. J* **559** (2001) 973–984.

[221] P. S. Marrocchesi, *Charged Cosmic Rays: a Review of Balloon and Space Borne Measurements*, in *25th European Cosmic Ray Symposium (ECRS 2016) Turin, Italy, September 04-09, 2016*, 2017. arXiv:1704.00304.

[222] N. Kawanaka, K. Ioka, Y. Ohira, and K. Kashiyama, *TeV Electron Spectrum for Probing Cosmic-Ray Escape from a Supernova Remnant*, *Astrophys. J.* **729** (2011) 93, [arXiv:1009.1142].

[223] **CALET** Collaboration, Y. Akaike, *Simulations for CALET Energy Calibration Confirmed Using CERN-SPS Beam Tests*, *PoS* **ICRC2015** (2016) 613.

[224] T. Niita, S. Torii, Y. Akaike, Y. Asaoka, K. Kasahara, S. Ozawa, and T. Tamura, *Energy calibration of Calorimetric Electron Telescope (CALET) in space*, *Adv. Space Res.* **55** (2015) 2500–2508.

[225] H. Yuksel, M. D. Kistler, and T. Stanev, *TeV Gamma Rays from Geminga and the Origin of the GeV Positron Excess*, *Phys. Rev. Lett.* **103** (2009) 051101, [arXiv:0810.2784].

[226] S. Algeri, J. Conrad, and D. A. van Dyk, *A method for comparing non-nested models with application to astrophysical searches for new physics*, *Mon. Not. Roy. Astron. Soc.* **458** (2016), no. 1 L84–L88, [arXiv:1509.01010].

[227] O. Adriani et al., *Extended Measurement of the Cosmic-Ray Electron and Positron Spectrum from 11 GeV to 4.8 TeV with the Calorimetric Electron Telescope on the International Space Station*, *Phys. Rev. Lett.* **120** (2018), no. 26 261102, [arXiv:1806.09728].

[228] K. Fang, X.-J. Bi, and P.-F. Yin, *Explanation of the knee-like feature in the DAMPE cosmic $e^- + e^+$ energy spectrum*, *Astrophys. J.* **854** (2018), no. 1 57, [arXiv:1711.10996].

[229] P. Athron, C. Balazs, A. Fowlie, and Y. Zhang, *Model-independent analysis of the DAMPE excess*, *JHEP* **02** (2018) 121, [arXiv:1711.11376].

[230] P.-H. Gu and X.-G. He, *Electrophilic dark matter with dark photon: from DAMPE to direct detection*, *Phys. Lett.* **B778** (2018) 292–295, [arXiv:1711.11000].

[231] J. Cao et al., *Scalar dark matter interpretation of the DAMPE data with U(1) gauge interactions*, *Phys. Rev.* **D97** (2018), no. 9 095011, [arXiv:1711.11452].

[232] D. Hooper and T. Linden, *Measuring the Local Diffusion Coefficient with H.E.S.S. Observations of Very High-Energy Electrons*, *Phys. Rev.* **D98** (2018), no. 8 083009, [arXiv:1711.07482].

# Research Achievements

1. **Refereed Journal Papers**

   - *"An Interpretation of the Cosmic-Ray Electron + Positron Spectrum from 10 GeV to 3 TeV Measured by CALET on the ISS"*,
     **International Journal of Modern Physics D; *IJMPD 1950035 (2019) no. 02***; [arXiv: 1712.06265]
     Saptashwa Bhattacharyya, Holger Motz, Yoichi Asaoka, Shoji Torii.
   - *"Decaying Fermionic Dark Matter Search with CALET"*,
     **Journal of Cosmology and Astroparticle Physics; *JCAP 1708 (2017) no.08, 2012***; [arXiv: 1702.02546]
     Saptashwa Bhattacharyya, Holger Motz, Shoji Torii, Yoichi Asaoka.
   - *"CALET's Sensitivity to Dark Matter Annihilation in the Galactic Halo"*,
     **Journal of Cosmology and Astroparticle Physics; *JCAP 1512 (2015) no.12, 047***; [arXiv: 1510.03168]
     Holger Motz, Yoichi Asaoka, Shoji Torii, Saptashwa Bhattacharyya.

2. **Conference Proceedings**

   - *"Searching for Cosmic-Ray Signals from Decaying Fermionic Dark Matter with CALET"*,
     **Proceeding of Science; *ICRC 2017, 919***;
     Saptashwa Bhattacharyya, Holger Motz, Shoji Torii, Yoichi Asaoka.
   - *"Searching for Anisotropy in Electron + Positron Cosmic-Rays with CALET"*,
     **Proceeding of Science; *ICRC 2017, 265***;
     Holger Motz, Yoichi Asaoka, Shoji Torii, Saptashwa Bhattacharyya.

- *"Self Consistent Simulation of Dark Matter and Background"*,
  **Proceeding of Science; *ICRC 2015, 1182***;
  Saptashwa Bhattacharyya, Holger Motz, Shoji Torii, Yoichi Asaoka.
- *"CALET's Sensitivity to Dark Matter and Astrophysical Sources"*,
  **Proceeding of Science; *ICRC 2015, 1194***;
  Holger Motz, Yoichi Asaoka, Shoji Torii, Saptashwa Bhattacharyya.

3. **Oral and Poster Presentation**

- *"Searching for Decaying Fermionic Dark Matter with CALET"*,
  **Japan Physical Society, *Presentation Id: 18aK21-5, Osaka University, March 2017***;
  Saptashwa Bhattacharyya, Holger Motz, Shoji Torii, Yoichi Asaoka.
- *"Investigating Leptonic 3-Particle Dark Matter Decay as the Source of Positron Excess with CALET"*,
  **Japan Physical Society, *Presentation Id: 21pSP-9, Miyazaki University, September 2016***;
  Holger Motz, Yoichi Asaoka, Shoji Torii, Saptashwa Bhattacharyya.
- *"Discerning Pulsar and Dark Matter Explanations of Positron Excess with CALET"*,
  **Japan Physical Society, *Presentation Id: 19aAT-3, Tohoku Gakuin University, March 2016***;
  Holger Motz, Yoichi Asaoka, Shoji Torii, Saptashwa Bhattacharyya.
- *"Self-Consistent Simulation of Cosmic-Ray Background Including Dark Matter Signatures"*,
  **Japan Physical Society, *Presentation Id: 21pDC-10, Waseda University, March 2015***;
  Saptashwa Bhattacharyya, Holger Motz, Shoji Torii, Yoichi Asaoka.
- *"CALET's Potential to Identify the Origin of the Cosmic-Ray Positron Excess"*,
  **Japan Physical Society, *Presentation Id: 28aTS-2, Tokai University, March 2014***;
  Holger Motz, Saptashwa Bhattacharyya, Shoji Torii, Tae Niita, Yoichi Asaoka, Yosui Akaike.